INL/EXT-09-16140

High Temperature Electrolysis for Hydrogen Production from Nuclear Energy – Technology Summary

J. E. O'Brien
C. M. Stoots
J. S. Herring
M. G. McKellar
E. A. Harvego
M. S. Sohal
K. G. Condie

February 2010

The INL is a U.S. Department of Energy National Laboratory
operated by Battelle Energy Alliance

Idaho National Laboratory

INL/EXT-09-16140

High Temperature Electrolysis for Hydrogen Production from Nuclear Energy – Technology Summary

J. E. O'Brien
C. M. Stoots
J. S. Herring
M. G. McKellar
E. A. Harvego
M. S. Sohal
K. G. Condie

February 2010

Idaho National Laboratory
Idaho Falls, Idaho 83415

http://www.inl.gov

Prepared for the
U.S. Department of Energy
Office of Nuclear Energy
Under DOE Idaho Operations Office
Contract DE-AC07-05ID14517

ABSTRACT

The Department of Energy, Office of Nuclear Energy, has requested that a Hydrogen Technology Down-Selection be performed to identify the hydrogen production technology that has the best potential for timely commercial demonstration and for ultimate deployment with the Next Generation Nuclear Plant (NGNP). An Independent Review Team (IRT) has been assembled to execute the down-selection. This report has been prepared to provide the members of the Independent Review Team with detailed background information on the High Temperature Electrolysis (HTE) process, hardware, and state of the art. The Idaho National Laboratory has been serving as the lead lab for HTE research and development under the Nuclear Hydrogen Initiative. The INL HTE program has included small-scale experiments, detailed computational modeling, system modeling, and technology demonstration. Aspects of all of these activities are included in this report. In terms of technology demonstration, the INL successfully completed a 1000-hour test of the HTE Integrated Laboratory Scale (ILS) technology demonstration experiment during the fall of 2008. The HTE ILS achieved a hydrogen production rate in excess of 5.7 Nm^3/hr, with a power consumption of 18 kW. This hydrogen production rate is far larger than has been demonstrated by any of the thermochemical or hybrid processes to date.

This report was prepared in April-May 2009 specifically for the IRT, which at the end of its evaluation in July 2009, recommended that:

> *DOE-NE should focus on the continued development of HTSE [High Temperature Steam Electrolysis] as the leading candidate for integration with NGNP in 2021. This conclusion is based upon the IRT judgment that HTSE has the highest probability of meeting the down-selection criteria described in the report, including efficient production of hydrogen at NGNP conditions.*

Because of continued interest in a comprehensive technology summary, the report has now been cleared for public release. Although the text of the summary has not been updated to reflect work since May 2009, the bibliography of project publications beginning on page 56 has been updated to show more recent work.

TABLE OF CONTENTS

LIST OF FIGURES

NOMENCLATURE

F	Faraday number, 96487 C/mol
ASR	area-specific resistance, Ohm·cm^2
ΔG_R	gibbs energy of reaction, J/mol
ΔH_f^o	enthalpy of formation, J/mol
H_i	component sensible enthalpy, J/mol
ΔH_R	enthalpy of reaction, J/mol
HHV	higher heating value
i	current density, A/cm^2
I	current, A
j	number of electrons transferred per molecule of hydrogen produced
LHV	lower heating value
$\dot{N}_{H_2}$	molar hydrogen flow rate, mol/s
$\Delta\dot{N}_{H_2}$	molar hydrogen production rate, mol/s
P	pressure, kPa
q''	heat flux, W/cm^2
Q_H	high-temperature heat addition, J/mol
Q_L	low-temperature heat rejection, J/mol
$\dot{Q}_T$	isothermal heat transfer rate, W
$\dot{Q}$	heat transfer rate, W
R_u	universal gas constant, J/mol·K
ΔS_R	entropy of reaction, J/mol·K
T	temperature, K
T_o	standard temperature, K
T_L	temperature of heat rejection, K
T_H	temperature of heat addition, K
T_R	reactant temperature, K
T_P	product temperature, K
V	voltage, V
V^o	standard-state open-cell potential, V
V_N	Nernst potential, V
V_{op}	operating voltage, V
V_{tn}	thermal neutral voltage, V
$\dot{W}$	work, rate basis, W
y	mole fraction
η_H	overall thermal-to-hydrogen efficiency
η_{th}	power cycle thermal efficiency
η_e	electrolysis efficiency

INTRODUCTION

High-temperature nuclear reactors have the potential for substantially increasing the efficiency of hydrogen production from water, with no consumption of fossil fuels, no production of greenhouse gases, and no other forms of air pollution. Efficient water-splitting for hydrogen production can be accomplished via high-temperature electrolysis (HTE) or thermochemical processes, using high-temperature nuclear process heat. In order to achieve high efficiencies, both processes require high-temperature operation. Thus these hydrogen-production technologies are tied to the development of advanced high-temperature nuclear reactors. High-temperature electrolytic water-splitting supported by nuclear process heat and electricity has the potential to produce hydrogen with overall thermal-to-hydrogen efficiencies of 50% or higher, based on high heating value. This efficiency is near that of the thermochemical processes [1 - 3], but without the severe corrosive conditions of the thermochemical processes and without the fossil fuel consumption and greenhouse gas emissions associated with hydrocarbon processes.

A research program is under way at the Idaho National Laboratory (INL) to simultaneously address the technical and scale-up issues associated with the implementation of solid-oxide electrolysis cell technology for efficient hydrogen production from steam. We are coordinating a progression of electrolysis cell and stack testing activities, at increasing scales, along with a continuation of supporting research activities in the areas of materials development, single-cell testing, detailed computational fluid dynamics (CFD) analysis and system modeling.

The INL HTE program also includes an investigation of the feasibility of producing syngas by simultaneous electrolytic reduction of steam and carbon dioxide (coelectrolysis) at high temperature using solid-oxide cells. Syngas, a mixture of hydrogen and carbon monoxide, can be used for the production of synthetic liquid fuels via Fischer-Tropsch processes. This concept, coupled with nuclear energy, provides a possible path to reduced greenhouse gas emissions and increased energy independence, without the major infrastructure shift that would be required for a purely hydrogen-based transportation system [4 - 6]. Furthermore, if the carbon dioxide feedstock is obtained from biomass, the entire concept would be carbon-neutral.

1. FUNDAMENTALS

1.1. General Thermodynamics of Thermal Water Splitting Processes

A basic thermodynamic analysis can be applied to any general thermal water-splitting process in order to determine the overall process efficiency limits as a function of temperature. Consider the process diagram for thermal water splitting shown in Fig. 1. Water enters the control volume from the left. Since the ultimate feedstock for any large-scale water-splitting operation will be liquid water, it is reasonable to consider the case in which water enters the control volume in the liquid phase at a specified temperature T and pressure P, typically near ambient conditions. Pure hydrogen and oxygen streams exit the control volume on the right, also at T and P. Two heat reservoirs are available, a high-temperature reservoir at temperature T_H and a low-temperature reservoir at temperature T_L. Heat transfer between these reservoirs and the control volume is indicated in the figure as Q_H and Q_L. Note that there is no work crossing the control-volume boundary. Therefore if the process under consideration is high-temperature electrolysis, both the power cycle (based on a heat engine for the purposes of this discussion) and the electrolyzer are located inside the control volume.

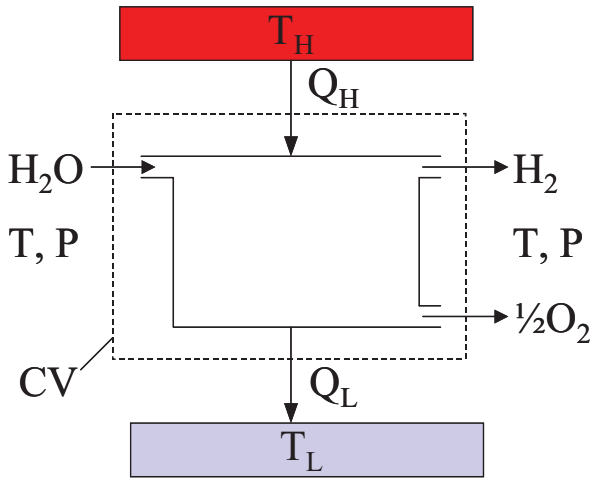

Figure 1. Schematic of a generic thermal water-splitting process operating between temperatures T_H and T_L.

From an overall chemical reaction standpoint, the water-splitting process corresponds to the dissociation or reduction of water:

$$H_2O \rightarrow H_2 + \tfrac{1}{2}\, O_2 \qquad (1)$$

The first and second laws of thermodynamics can be applied to this process as follows:

$$1^{st}\text{ law:} \qquad Q_H - Q_L = \Delta H_R \qquad (2)$$

$$2^{nd}\text{ law:} \qquad \Delta S_R \geq \frac{Q_H}{T_H} - \frac{Q_L}{T_L} \qquad (3)$$

where ΔH_R is the enthalpy of reaction and ΔS_R is the entropy change of the reaction. The overall thermal-to-hydrogen efficiency of thermal water splitting processes can be defined in terms of the net enthalpy increase of the reaction products over the reactants (can also be thought of as the energy content or heating value of the produced hydrogen), divided by the (costly) high-temperature heat added to the system:

$$\eta_H = \frac{\Delta H_R}{Q_H} \qquad (4)$$

Combining the first and second law equations for the reversible case and substituting into the efficiency definition yields:

$$\eta_{H,\max} = \frac{1 - T_L / T_H}{1 - T_L \Delta S_R / \Delta H_R} \qquad (5)$$

Note that the water splitting process defined in Fig. 1 is simply the reverse of the combustion reaction of hydrogen with oxygen. Therefore the enthalpy of reaction for the water-splitting process is the opposite of the enthalpy of combustion, which by definition is equal to the "heating value" of the hydrogen. Since for our process, we have assumed that the water enters the control volume in the liquid phase,

$$\Delta H_R = HHV \tag{6}$$

where HHV is the "high heating value" of hydrogen. If we further assume that T and P represent standard conditions, and that $T_L = T_o$, then

$$\Delta H_R - T_L \Delta S_R = -\Delta G^o_{f,H_2O} \tag{7}$$

and the efficiency expression can be rewritten as:

$$\eta_{H,\max} = \left(1 - \frac{T_L}{T_H}\right)\left(\frac{HHV}{-\Delta G^o_{f,H_2O}}\right) = \left(1 - \frac{T_L}{T_H}\right)\left(\frac{1}{0.83}\right) \tag{8}$$

The high heating value of the hydrogen and the standard-state Gibbs energy of formation for water are fixed quantities such that the second factor on the right-hand side is a constant. This efficiency limit was also derived for the sulfur-iodine thermochemical process based on an exergy analysis in [7].

Comparing Eqn. (8) to Eqn. (4), the high-temperature heat requirement for the process can be stated as:

$$Q_H \geq \frac{T_H}{T_H - T_L}\left(-\Delta G^o_{f,H_2O}\right) \tag{9}$$

This result was derived for thermochemical cycles by Abraham and Schreiner [8], and applied to solar thermal dissociation of water by Fletcher and Moen [9], who noted that the maximum efficiencies of all thermochemical processes can be related to the efficiencies of Carnot engines operating between the same upper and lower temperatures. It is necessary only to add, conceptually, a reversible fuel cell which converts the hydrogen and oxygen to liquid water at the lower temperature, performing an amount of electrical work given by the Gibbs free energy of the reaction.

A plot of thermal water splitting efficiencies is presented in Fig. 2 for T_L = 20°C. The top curve represents the maximum possible water-splitting efficiency result given by Eqn. (8). The exergetic efficiency of the thermal water splitting process is defined as the ratio of the actual efficiency to the maximum possible efficiency. A reasonable value to assume for an achievable exergetic efficiency is 65%, which is represented by the bottom curve in Fig. 2. The 65% value is based on a typical percentage of Carnot efficiency that can be achieved with a well engineered modern power cycle. The first conclusion to be drawn is that high temperature is needed for efficient hydrogen production based on thermal water splitting, regardless of the specific method

used. If we assume that 65% of the maximum possible efficiency might also be achievable with a well engineered thermal water-splitting process, then efficiencies of the magnitude given in the lower curve of Fig. 2 should be expected.

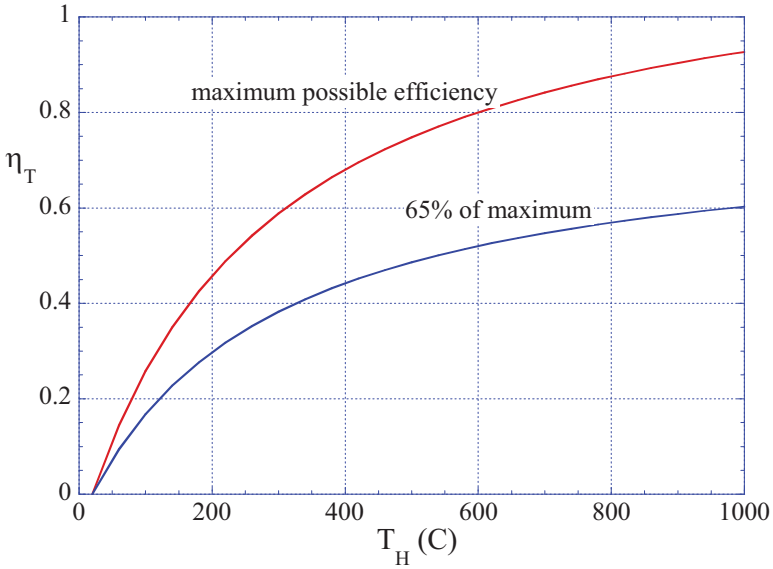

Figure 2. Theoretical thermal water splitting efficiencies.

Detailed process analyses have been performed at INL [10] to analyze HTE-based hydrogen-production systems coupled to advanced nuclear reactors. Results from this study are presented in Fig. 3. This figure shows overall hydrogen production efficiencies, based on high heating value, plotted as a function of reactor outlet temperature. The figure includes the curve that represents 65% of the thermodynamic maximum efficiency, again assuming T_L = 20°C. Three different advanced-reactor/power-conversion combinations were considered: a helium-cooled reactor coupled to a direct recuperative Brayton cycle, a supercritical CO_2-cooled reactor coupled to a direct recompression cycle, and a sodium-cooled fast reactor coupled to a Rankine cycle. The system analyses were performed using UniSim [11] software. Each reactor/power-conversion combination was analyzed over an appropriate reactor outlet temperature range. The figure shows results for both HTE and low-temperature electrolysis

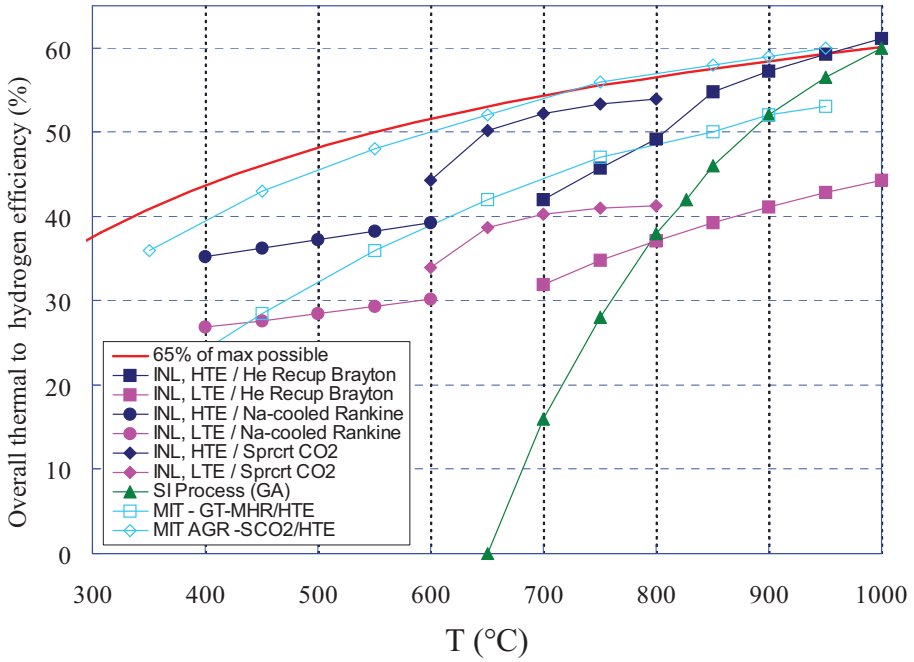

Figure 3. Overall thermal-to-hydrogen efficiencies for HTE coupled to three different reactor types, as a function of reactor outlet temperature.

(LTE). Results of system analyses performed at MIT [12] are also shown. The lower MIT curve, labeled MIT-GT-MHR/HTE represents overall efficiency predictions for a helium-cooled reactor with a direct Brayton cycle power conversion unit. The upper MIT curve, labeled MIT-AGR-SCO2/HTE represents overall efficiency predictions for a CO_2-cooled advanced gas reactor with a supercritical CO_2 power conversion unit. Finally, an efficiency curve for the SI thermochemical process [13] is also shown in Fig. 3. The results presented in Fig. 3 indicate that, even when detailed process models are considered, with realistic component efficiencies, heat exchanger performance, and operating conditions, overall hydrogen production efficiencies in excess of 50% can be achieved for HTE with reactor outlet temperatures above 850°C. For reactor outlet temperatures of 600 - 800°C, the supercritical CO_2/recompression power cycle is superior to the He-cooled/Brayton cycle concept. This conclusion is consistent with results presented in [12]. The efficiency curve for the SI process also includes values above 50% for reactor outlet temperatures above 900°C, but it drops off quickly with decreasing temperature, and falls below values for LTE coupled to high-temperature reactors for outlet temperatures below 800°C. Even LTE benefits from higher reactor outlet temperatures because of the improved power conversion thermal efficiencies associated with higher reactor outlet temperatures. Current planning for NGNP [14] indicates that reactor outlet temperatures will be at or below 900°C, which favors HTE.

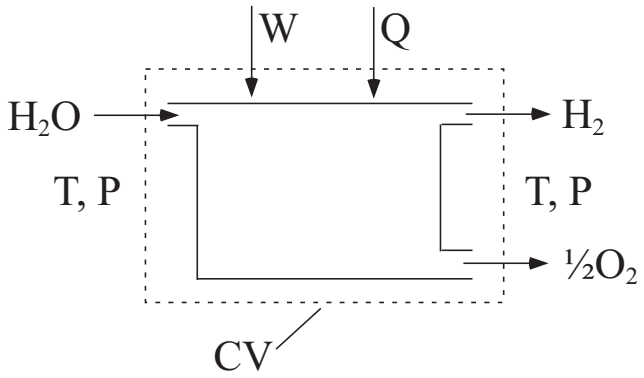

Figure 4. Schematic of a water electrolysis process operating at temperature T.

1.2. Thermodynamics of High Temperature Electrolysis

Focusing now on electrolysis, consider a control volume surrounding an isothermal electrolysis process, as shown in Fig. 4. In this case, both heat and work interactions cross the control volume boundary. The first law for this process is given by:

$$Q - W = \Delta H_R \tag{10}$$

For reversible operation,

$$Q_{rev} = T\Delta S_R \tag{11}$$

such that

$$W_{rev} = \Delta H_R - T\Delta S_R = \Delta G_R \tag{12}$$

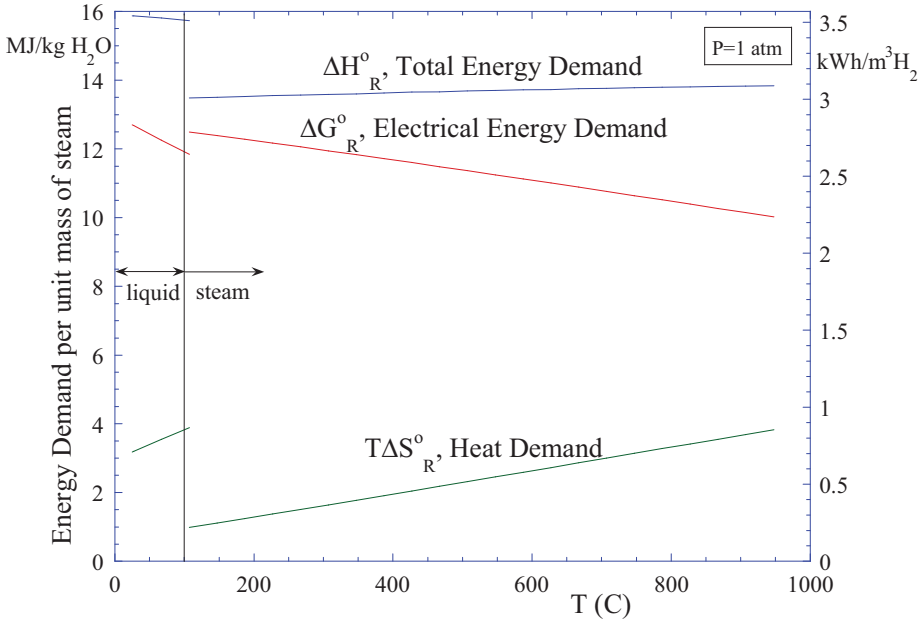

Figure 5. Standard-state ideal energy requirements for electrolysis as a function of temperature.

The thermodynamic properties appearing in Eqn. (12) are plotted in Fig. 5 as a function of temperature for the H_2-H_2O system from 0°C to 1000°C at standard pressure. This figure is often cited as a motivation for high-temperature electrolysis versus low-temperature electrolysis. It shows that the Gibbs free energy change, ΔG_R, for the reacting system decreases with increasing temperature, while the product of temperature and the entropy change, $T\Delta S_R$, increases. Therefore, for reversible operation, the electrical work requirement decreases with temperature, and a larger fraction of the total energy required for electrolysis, ΔH_R, can be supplied in the form of heat, represented by $T\Delta S_R$. Since heat-engine-based electrical work is limited to a production thermal efficiency of 50% or less, decreasing the work requirement results in higher overall thermal-to-hydrogen production efficiencies. Note that the total energy requirement, ΔH_R, increases only slightly with temperature, and is very close in magnitude to the lower heating value of hydrogen. The ratio of ΔG_R to ΔH_R is about 93% at 100°C, decreasing to only about 70% at 1000°C. Operation of the electrolyzer at high temperature is also desirable from the standpoint of reaction kinetics and electrolyte conductivity, both of which improve dramatically at higher operating temperatures. Potential disadvantages of high-temperature operation include the limited availability of very high temperature process heat and materials issues such as corrosion and degradation.

The solid-oxide electrolysis cell is a solid-state electrochemical device consisting of an oxygen-ion-conducting electrolyte (e.g., yttria- or scandia-stabilized zirconia) with porous electrically conducting electrodes deposited on either side of the electrolyte. A cross-section of a planar design is shown in Fig. 6. The design depicted in the figure shows an electrolyte-supported cell with a nickel cermet cathode and a perovskite anode such as strontium-doped lanthanum manganite (LSM). In an electrolyte-supported cell, the electrolyte layer is thicker than either of the electrodes. The flow fields conduct electrical current through the stack and provide flow passages for the process gas streams. The separator plate or bipolar plate separates

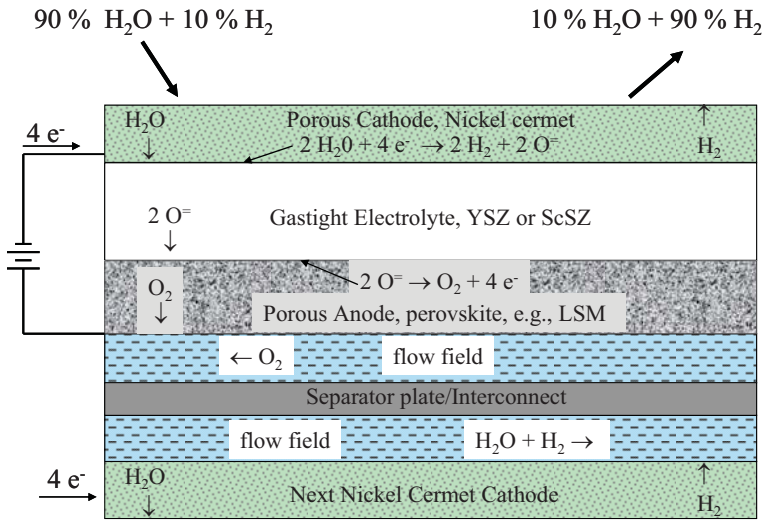

Figure 6. Cross-section of a planar high temperature electrolysis stack.

the process gas streams. It must also be electrically conducting and is usually metallic, such as a ferritic stainless steel.

As shown in the figure, a mixture of steam and hydrogen at 750-950°C is supplied to the cathode side of the electrolyte (note that cathode and anode sides are opposite to their fuel-cell-mode roles). The half-cell electrochemical reactions occur at the triple-phase boundary near the electrode/electrolyte interface, as shown in the figure. Oxygen ions are drawn through the electrolyte by an applied electrochemical potential. The ions liberate their electrons and recombine to form molecular O_2 on the anode side. The inlet steam-hydrogen mixture composition may be as much as 90% steam, with the remainder hydrogen. Hydrogen is included in the inlet stream in order to maintain reducing conditions at the cathode. The exiting mixture may be as much as 90% H_2. It is not desirable to attempt to operate the stack with a higher outlet composition of hydrogen because there is a risk of local steam starvation which can lead to significantly reduced cell performance. Furthermore, based on detailed analyses of large-scale HTE systems, the overall hydrogen production efficiency is almost flat above about 50% steam utilization [15]. Product hydrogen and residual steam is passed through a condenser or membrane separator to purify the hydrogen.

In order to accomplish electrolysis, a voltage must be applied across the cell that is greater in magnitude than the open-cell potential. The standard-state open-cell potential is given by:

$$V^o = \frac{\Delta G_R^o}{jF} \tag{13}$$

where j is the number of electrons transferred per molecule of hydrogen produced. For the steam-hydrogen system, in which the $O^=$ ions are transported through the solid-oxide electrolyte, $j = 2$. The standard-state open-cell potential applies to the case in which pure reactants and products are separated and at one standard atmosphere pressure. In most practical HTE systems, the incoming steam is mixed with some hydrogen and possibly some inert gas. Residual steam can be removed from the product by condensation. On the oxygen-evolution side of the cells, air is often used as a sweep gas, so the oxygen partial pressure is only about 21% of the operating

pressure. In addition, the electrolysis system can operate at elevated pressure. In order to account for the range of gas compositions and pressures that occur in a real system, the open-cell (or Nernst) potential can be obtained from the Nernst equation, which can be written as:

$$V_N = V^o - \frac{R_u T}{jF} \ln\left[\left(\frac{y_{H2O}}{y_{H2} y_{O2}^{1/2}}\right)\left(\frac{P}{P_{std}}\right)^{-1/2}\right] \tag{14}$$

Operation of a solid-oxide stack in the electrolysis mode is fundamentally different than operation in the fuel-cell mode for several reasons, aside from the obvious change in direction of the electrochemical reaction. From the standpoint of heat transfer, operation in the fuel-cell mode typically necessitates the use of significant excess air flow in order to prevent overheating of the stack. The potential for overheating arises from two sources: (1) the exothermic nature of the hydrogen oxidation reaction, and (2) ohmic heating associated with the electrolyte ionic resistance and other loss mechanisms.

Conversely, in the electrolysis mode, the steam reduction reaction is endothermic. Therefore, depending on the operating voltage, the net heat generation in the stack may be negative, zero, or positive. This phenomenon is illustrated in Fig. 7. The figure shows the respective internal heat sink/source fluxes in a planar solid-oxide stack associated with the electrochemical reaction and the ohmic heating. The ohmic heat flux (W/cm^2) is given by:

$$q''_{Ohm} = i^2 ASR = i(V_{op} - V_N) \tag{15}$$

where i is the current density (A/cm^2), V_N is the mean Nernst potential for the operating cell, and ASR (Ohm·cm^2) is the area-specific resistance of the cell. The reaction heat flux is given by:

$$q''_R = \frac{i}{2F}(T\Delta S_e) = \frac{i}{2F}(\Delta G_e - \Delta H_R) \tag{16}$$

where ΔS_e is the entropy change for the actual electrolysis process, accounting for the reactant and product partial pressures.

The net heat flux is also shown in Fig. 7. An area-specific resistance of 1.25, an operating temperature of 1200 K, and hydrogen mole fractions of 0.1 and 0.95 at the inlet and outlet, respectively, were assumed for these calculations. In the fuel-cell mode, the net heat flux is always positive and increases rapidly with operating voltage and current density. In the electrolysis mode, the net heat flux is negative for low operating voltages, increases to zero at the "thermal-neutral" voltage, and is positive at higher voltages and current densities. The thermal-neutral voltage can be predicted from direct application of the rate-based First Law to the isothermal system shown in Fig. 4:

$$\dot{Q} - \dot{W} = \Delta\dot{N}_{H_2} \Delta H_R \tag{17}$$

where, from Faraday's law,

$$\Delta\dot{N}_{H_2} = I / 2F \tag{18}$$

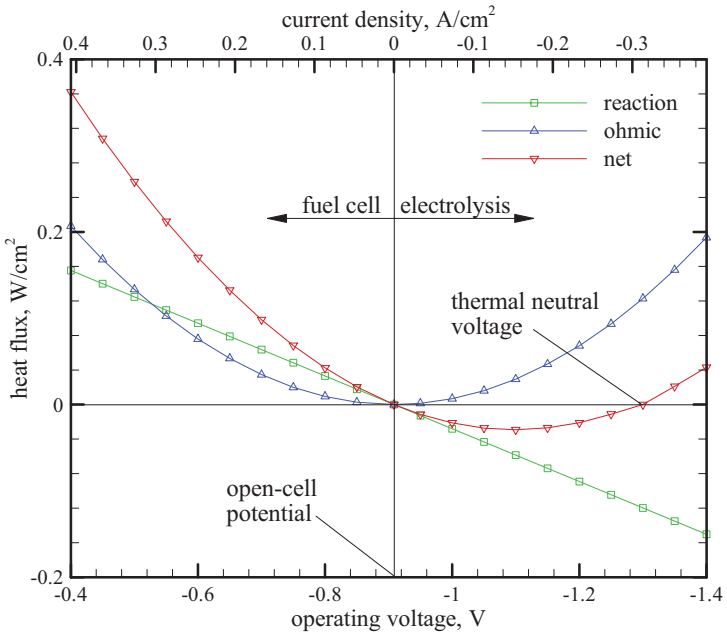

Figure 7. Thermal contributions in electrolysis and fuel cell modes of operation.

Letting $\dot{Q} = 0$ (no external heat transfer), $\dot{W} = IV_{tn}$, yielding:

$$V_{tn} = \Delta H_R / 2F \tag{19}$$

Note that the reaction heat flux of Eqn. (16) can also be written in terms of the thermal-neutral voltage as:

$$q''_R = i(V_N - V_{tn}) \tag{20}$$

Since the enthalpy of reaction, ΔH_R, is strictly a function of temperature (ideal gas approximation), the thermal-neutral voltage is also strictly a function of temperature, independent of cell *ASR* and gas compositions. The particular values of net cell heat flux at other operating voltages do however depend on cell *ASR* and gas compositions. The thermal-neutral voltage increases only slightly in magnitude over the typical operating temperature range for solid-oxide cells, from 1.287 V at 800°C to 1.292 V at 1000°C. At typical solid-oxide electrolysis stack temperatures and *ASR* values, operation at the thermal-neutral voltage yields current densities in the 0.2 – 0.6 A/cm^2 range, which is very close to the current density range that has yielded successful long-term operation in solid-oxide fuel cell stacks.

Operation at or near the thermal-neutral voltage simplifies thermal management of the stack since no significant excess gas flow is required and component thermal stresses are minimized. In fact, in the electrolysis mode, since oxygen is being produced, there is also no theoretical need for air flow to support the reaction at all. In a large-scale electrolysis plant, the pure oxygen produced by the process could be saved as a valuable commodity. However, there are several good reasons to consider the use of a sweep gas on the oxygen side. First, the use of a sweep gas will minimize the performance degradation associated with any small leakage of hydrogen from the steam/hydrogen side to the oxygen side of the cell. Second, there are serious materials issues associated with the handling of pure oxygen at elevated temperatures. Finally, the use of a sweep gas (especially one that does not contain oxygen) on the oxygen side of the electrolysis

cell reduces the average mole fraction and partial pressure of oxygen, thereby reducing the open-cell and operating potentials, resulting in higher electrolysis efficiencies, as we shall see shortly.

There are some additional thermodynamic implications related to the thermal neutral voltage. In particular, electrolyzer operation at or above the thermal neutral voltage negates the argument that is often stated as a motivation for high-temperature electrolysis that a fraction of the total energy requirement can be supplied in the form of heat. In fact, for isothermal operation at voltages greater than thermal neutral, heat rejection is required.

Electrolysis efficiency, η_e, can be defined for HTE, analogous to the definition of fuel cell efficiency [16]. The electrolysis efficiency quantifies the heating value of the hydrogen produced by electrolysis per unit of electrical energy consumed in the stack. Based on this definition,

$$\eta_e = \frac{\dot{N}_{H_2} \Delta H_R}{VI} \tag{21}$$

and since the stack electrical current is directly related to the molar production rate of hydrogen via Faraday's law, the electrolysis efficiency can be expressed strictly in terms of cell operating potentials as:

$$\eta_e = \frac{\Delta H_R / 2F}{V_{op}} = \frac{V_{tn}}{V_{op}}. \tag{22}$$

The efficiency for the fuel-cell mode of operation is the inverse of Eqn. (22). A fuel utilization factor is often included in the fuel-cell efficiency definition, but it is not needed in the electrolysis definition since no fuel (only steam) is wasted at low utilization.

It should be noted that the value of the efficiency defined in this manner for electrolysis is greater than 1.0 for operating voltages lower than thermal neutral. As an example, for the reversible standard-state reference case, from Eqn. (12), on a rate basis:

$$\dot{W}_{rev} = \dot{N}_{H_2} \Delta G_R^o = IV^o \tag{23}$$

Invoking Faraday's law, the operating cell potential for this case approaches the reference open-cell value, $V^o = \Delta G_R / 2F$, yielding:

$$\eta_{e,o} = \frac{\Delta H_R^o}{\Delta G_R^o} \tag{24}$$

which for steam electrolysis at 850ºC is equal to 1.34. For cases with variable gas composition or partial pressure, the open-cell potential is given by the Nernst Equation (14) and the corresponding efficiency limit varies accordingly. It is not desirable to operate an electrolysis stack near the maximum efficiency limit, however, because the only way to approach this limit is to operate with very low current density. There is a trade-off between efficiency and hydrogen production rate in selecting an electrolysis stack operating voltage. This trade-off is illustrated in Fig. 8. The upper curve in the figure shows the decrease in electrolysis efficiency that occurs as the per-cell operating voltage is increased above the open-cell voltage, V_N, according to Eqn. (22). Operation at the thermal-neutral voltage yields an electrolysis efficiency of 1.0. Area-

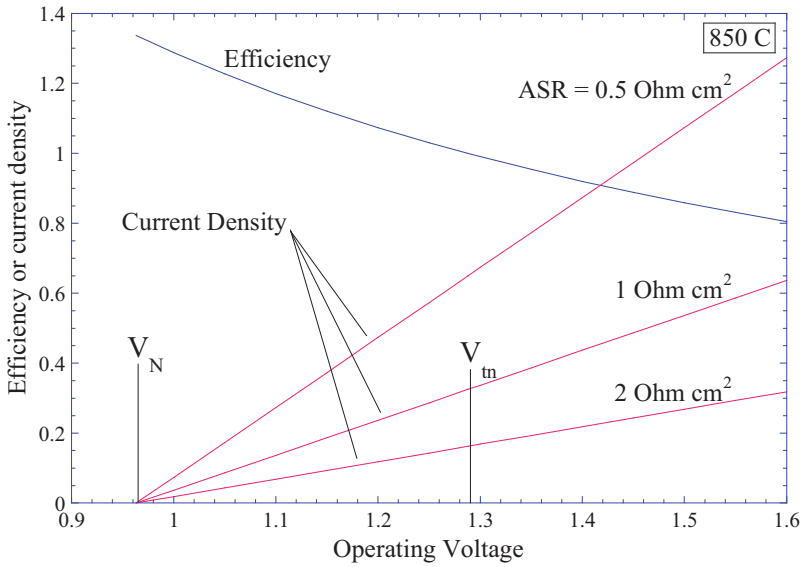

Figure 8. Effect of operating voltage and area-specific resistance on electrolysis efficiency.

specific resistance (*ASR*) represents the net effect of all the loss mechanisms in the electrolysis stack including, ohmic losses, activation and concentration overpotentials, etc. The bottom curves show the effect of operating voltage and *ASR* on the current density. Noting that:

$$V_{op} = \overline{V}_N + i \times ASR\,, \tag{25}$$

if a target current density (and corresponding hydrogen production rate) is selected, lower *ASR* values allow for stack operation at lower voltages and correspondingly higher efficiencies. Similarly, in the fuel-cell mode, there is a tradeoff between efficiency and maximum power production. Maximum power production for solid-oxide fuel cells occurs for operation at around 0.5 V, whereas maximum efficiency occurs at the open-cell potential, around 1.1 V for hydrogen-dominated SOFC fuel cell inlet gas compositions. Depending on cell performance and optimization parameters, a good operating point usually occurs at around 0.7 V in the fuel-cell mode of operation. In the electrolysis mode, a good tradeoff between efficiency and hydrogen production rate will occur at operating voltages below $\Delta H_R/2F$, around 1.1 V. The challenge is to develop SOEC stacks with low *ASR* such that a reasonable current density will be achievable at lower operating voltages.

Low operating voltages can also be maintained at a specified current density if the mean Nernst potential, $\overline{V}_{Nernst}$, is low. The mean Nernst potential can be reduced by increasing the cell operating temperature, increasing the steam content and flow rate in the feed stream, or by decreasing the oxygen content on the sweep gas side (anode) of the electrolysis cell. Of course, as the cell current density and hydrogen production rate is increased, the average steam content on the cathode side decreases and the average oxygen content on the anode side increases. These considerations indicate that, for maximum cell efficiency at a specified current density, steam utilization should be kept low and a high flow rate of a non-oxygen-containing sweep gas should be used. Unfortunately, results of large-scale system analyses [17] show that operating with low steam utilization results in low overall hydrogen production system efficiencies. For the system, the thermodynamic benefit of excess steam (lower average Nernst potential) is outweighed by the penalties associated with handling of the excess steam and incomplete heat recuperation.

Similar conclusions were drawn when considering the use of a non-oxygen-containing sweep gas (e.g., steam) on the oxygen side. Again, the thermodynamic benefits were outweighed by system considerations. In fact, the highest overall efficiencies for pressurized electrolyzers were achieved with no sweep gas, where the oxygen is allowed to evolve from the cells undiluted.

1.3. Isothermal vs. Non-Isothermal Operation

The analyses presented so far have all assumed isothermal electrolysis operation such that the outlet temperature of the products is the same as the inlet temperature of the reactants. For operating voltages between the open-cell potential and thermal neutral, isothermal operation requires heat addition during the electrolysis process. For operating voltages above thermal neutral, heat rejection is required to maintain isothermal operation. The enthalpy change for the electrolysis process under isothermal conditions is, by definition, the "enthalpy of reaction," ΔH_R. The enthalpy of reaction for steam reduction is a weak function of temperature, with a numerical value very close to the low heating value of hydrogen over a wide range of temperatures, as shown in Fig. 5. The magnitude of the heat transfer required to achieve isothermal operation, $\dot{Q}_T(T)$, can be calculated directly from the following form of the first law:

$$\dot{Q}_T(T) = \Delta\dot{N}_{H2}\Delta H_R(T) - IV_{op} \tag{26}$$

and since the hydrogen production rate, $\Delta\dot{N}_{H2}$ is equal to $I/2F$, and the thermal neutral voltage, $V_{tn} = \Delta H_R(T)/2F$,

$$\dot{Q}_T(T) = I(V_{tn} - V_{op}) \tag{27}$$

Note that this result predicts positive heat transfer to the electrolyzer for operating voltages less than thermal neutral and negative heat transfer (i.e., heat rejection from the electrolyzer) for operating voltages greater than thermal neutral. Since there is no sensible enthalpy change, this result is valid for all isothermal cases, even if excess reactants and/or inert gases are present. A graphical interpretation of the isothermal heat requirement on V-i coordinates is shown in Fig. 9. The figure shows the heat fluxes required to maintain isothermal operation for a target current density of 0.3 A/cm^2 for two values of ASR: 0.5 and 1.5 Ohm·cm^2 represented by the area enclosed between the vertical line at $V = V_{tn}$, the vertical line $V = V_{op}$ (V_{op} = 1.113 V for ASR = 0.5 Ohm·cm^2; V_{op} = 1.413 V for ASR = 1.5 Ohm·cm^2), and the horizontal lines at i = 0 and at i = 0.3 A/cm^2. Note that the higher ASR case requires an operating voltage that is above V_{tn} in order to achieve the target current density of 0.3 A/cm^2. Consequently, the associated isothermal heat transfer requirement is negative, indicating that heat rejection is needed to maintain isothermal operation at that condition.

Eqn. (27) can also be used to show that the maximum isothermal heat addition operating point corresponds to an operating voltage equal to the average of the open-cell potential and the thermal neutral voltage. Accordingly, the maximum isothermal heat addition is given by:

$$\dot{Q}_{\max}(T) = I\left(V_{tn} - \frac{V_{tn} + V_N}{2}\right) = I\left(\frac{V_{tn} - V_N}{2}\right) \tag{28}$$

where V_N is the open-cell potential. The total stack current, I, at any operating voltage is dependent on the stack ASR value, which is typically temperature-dependent.

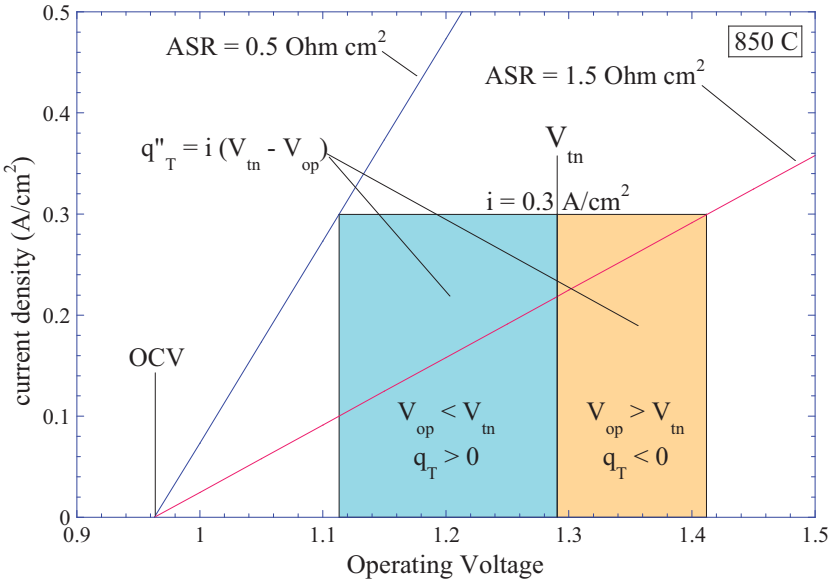

Figure 9. Graphical interpretation of isothermal heat requirements for two values of *ASR*.

Actual high-temperature electrolysis processes will generally not operate isothermally unless the operating voltage is very close to the thermal neutral voltage. For non-isothermal cases, the first law for electrolysis process must be written as:

$$\dot{Q} - \dot{W} = \sum_{P} \dot{N}_i [\Delta H^o_{f_i} + H_i(T_P) - H^o_i] - \sum_{R} \dot{N}_i [\Delta H^o_{f_i} + H_i(T_R) - H^o_i] \tag{29}$$

In this form, all reacting and non-reacting species included in the inlet and outlet streams can be accounted for, including inert gases, inlet hydrogen (introduced to maintain reducing conditions on the steam/hydrogen electrode), and any excess unreacted steam. In general, determination of the outlet temperature from Eqn. (29) is an iterative process [18]. The heat transferred during the process must first be specified (e.g., zero for the adiabatic case). The temperature-dependent enthalpy values of all species must be taken into account. The solution procedure begins with specification of the cathode-side inlet flow rates of steam, hydrogen, and any inert carrier gas such as nitrogen (if applicable). The inlet flow rate of the sweep gas (e.g., air or steam) on the anode side must also be specified. Specification of these flow rates allows for the determination of the inlet mole fractions of steam, hydrogen, and oxygen that appear in the Nernst equation. The steam mole fraction is expressed in terms of the hydrogen mole fraction as $1\text{-}y_{H2}\text{-}y_{N2}$. The desired current density and active cell area are then specified, yielding the total operating current. The corresponding hydrogen production rate is obtained from Faraday's law.

Once the per-cell hydrogen production rate is known, the outlet flow rates of hydrogen and steam on the cathode side and oxygen on the anode side can be determined. The flow rates of any inert gases, the anode-side sweep gas, and any excess steam or hydrogen are the same at the inlet and the outlet. Once all these flow rates are known, the summations in Eqn. (29) can be evaluated. The product summation must be evaluated initially at a guessed value of the product temperature, T_P.

The operating voltage corresponding to the specified current density is obtained from Eqn.

(25), where the stack area-specific resistance, *ASR*, must be estimated and specified as a function of temperature. To account for the variation in temperature and composition across an operating cell, the mean Nernst potential can be obtained from an integrated version of the Nernst equation:

$$\overline{V}_N = \frac{1}{2F(T_P - T_R)(y_{o,O2,A} - y_{i,O2,A})(y_{o,H2,C} - y_{i,H2,C})} \times \int_{T_R}^{T_P} \int_{y_{i,O2,A}}^{y_{o,O2,A}} \int_{y_{i,H2,C}}^{y_{o,H2,C}} \Delta G_R(T) + R_u T \ln\left(\frac{1 - y_{H2} - y_{N2}}{y_{H2} y_{O2}^{1/2}}\right) dy_{H2} dy_{O2} dT \qquad (30)$$

where $y_{i,\,O2,\,A}$ is the anode-side inlet mole fraction of oxygen, etc. Note that the upper limit of integration on the temperature integral is initially unknown. Once the *ASR* and the mean Nernst potential are known, the operating voltage is obtained from Eqn. (25) and the electrical work term in Eqn. (29) is obtained from $\dot{W} = -V_{op} I$. An algorithm then must be developed to iteratively solve for the product temperature, T_P, in order to satisfy Eqn. (29).

Results of sample parametric calculations based on this procedure are presented in Fig. 10. The inlet mass flow rates of steam-hydrogen and sweep air per cm^2 of active cell area are indicated in the caption. The calculations were performed for an inlet hydrogen mole fraction of 0.1 and an inlet temperature of 800°C (1073 K). Fig. 10(a) shows the heat flux required to maintain isothermal operation as a function of per-cell operating voltage for three different *ASR* values. This heat flux is positive (heat addition required) for voltages between open-cell and thermal neutral and negative for higher operating voltages. The peak heat flux requirement occurs halfway between the open-cell potential and the thermal neutral voltage. The magnitude of the peak heat flux is highest for the lowest *ASR* value since the current density (and hydrogen production rate) corresponding to each voltage value is highest for the lowest *ASR* value. Fig. 10(b) shows the mean outlet gas temperature as a function of per-cell operating voltage for adiabatic operation for three different *ASR* values. For adiabatic conditions, outlet temperatures are lower than inlet temperatures for voltages between open-cell and thermal neutral. For higher voltages, outlet temperatures increase rapidly with voltage. Again, the low-ASR case exhibits the largest effect due to its higher current density at each operating voltage.

Actual electrolyzers will generally operate at conditions that are neither isothermal, nor adiabatic. These two cases represent limits. For optimal electrolyzer performance, isothermal operation at an operating voltage below thermal neutral is desirable. In this case, some of the electrolysis energy is indeed supplied in the form of heat. One way to supply the required heat directly to the stack is through the use of a heated sweep gas. This strategy is just the opposite of the situation encountered in the fuel cell mode in which excess air is used for cell cooling.

2. SOLID OXIDE ELECTROLYSIS CELLS AND STACKS

2.1 Cell Materials

The solid-oxide electrolysis cell is a solid-state electrochemical device consisting of an oxygen-ion-conducting electrolyte (e.g., yttria- or scandia-stabilized zirconia) with porous electrically conducting electrodes deposited on either side of the electrolyte. The standard electrolyte material is formed by doping zirconia (ZrO_2) with, e.g., 8 molar pct. of yttria (yttrium oxide, Y_2O_3). A dopant composition of 8% or higher yields a "fully stabilized" electrolyte. The

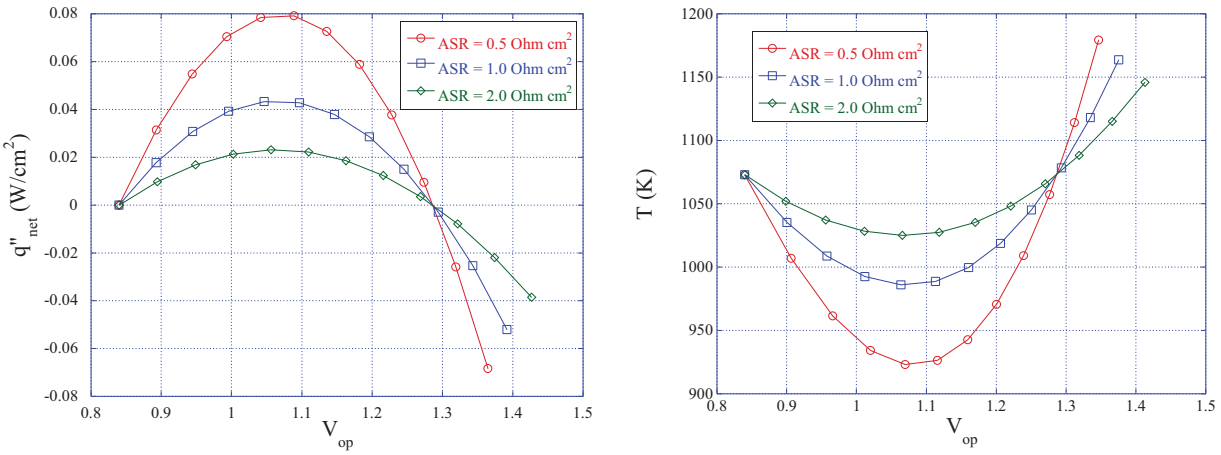

Figure 10. (a) Heat flux required for isothermal operation; (b) Outlet temperature for adiabatic operation; steam-hydrogen inlet flow rate: 0.0085 gm/min/cm^2, y_{H2i} = 0.1, sweep air inlet flow rate: 0.00561 gm/min/cm^2, T_{in} = 1073 K.

dopant serves two purposes. It "stabilizes" the cubic (or fluorite) crystal structure over a wide temperature range. Undoped zirconia exhibits a monoclinic crystal structure at room temperature and a tetragonal phase above 1170°C. Zirconia doped with yttria is called yttria-stabilized zirconia, or YSZ. In addition to stabilizing the crystal structure, when trivalent Y is substituted for tetravalent Zr, holes (unfilled positions) in the oxygen sub-lattice are introduced at the same time. This makes it possible for oxygen ions to move through the solid by hopping from hole to hole in the lattice. YSZ is therefore a good oxygen ion conductor. Other compounds such as scandia (Sc_2O_3) can also be used as the dopant. Scandia-stabilized zirconia (ScSZ) has a significantly higher ionic conductivity than YSZ, but is more expensive. Other potential electrolyte materials include samaria-doped ceria and calcia-doped lanthanum gallate.

The most common steam-hydrogen electrode material is porous nickel-zirconia (YSZ) cermet, but a nickel-ceria cermet can also be used. In the electrolysis mode, this electrode serves as the cathode. Because the cathode contains nickel metal, reducing conditions must be maintained on this electrode during cell operation. This is typically accomplished by including ~10% mole fraction hydrogen in the inlet flow. The nickel in the cathode acts as a catalyst for steam reduction. The zirconia in the cermet provides ionic conductivity. Porosity allows the steam to migrate to the active electrochemical reaction site and hydrogen to migrate away from the sites. The active reaction sites correspond to what is typically termed the "triple-phase boundary" where the electronic, ionic and gas phases coexist. These sites occur at locations where a pore structure intersects with nickel and zirconia particles.

Several materials have been studied for the air-oxygen electrode. This electrode must operate in a highly oxidizing environment. The most common material used is strontium-doped lanthanum manganite $La_{0.8}Sr_{0.2}MnO_3$, or LSM. This material provides good electronic conductivity and good catalytic activity and tolerance to the oxidizing environment. LSM is an example of a class of materials called perovskites, which have the general chemical formula ABO_3 where 'A' and 'B' are two cations of very different sizes (A much larger than B), and O is the anion that bonds to both. These perovskites exhibit p-type electrical conductivity that is enhanced by the introduction of lower-valence dopant cations such as Sr^{2+} to replace La^{3+} cations. Strontium and cobalt-doped lanthanum ferrites (LSF, LSCF) have also received lots of

attention recently. These materials are more catalytically active than LSM and therefore yield generally better performance, especially at temperatures below 800°C.

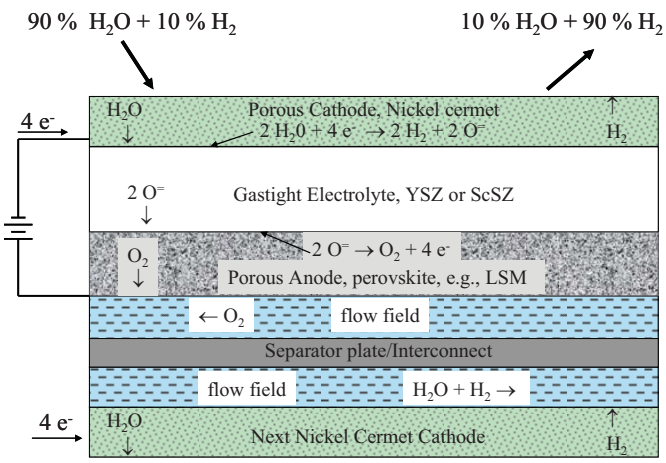

Figure 11. Cross-section of a planar high temperature electrolysis stack.

2.2. Electrolysis Cell Designs and Stack Configurations

Several basic cell designs have been developed for SOFC applications including electrolyte-supported, electrode-supported, and porous ceramic or metal substrate-supported cells. A full discussion of these various cell designs and the various fabrication techniques is beyond the scope of this report. Common cell characteristics include a dense gas-tight electrolyte layer, with porous electrodes on either side. In an electrolyte-supported cell, the electrolyte layer is thicker than either of the electrodes and must have sufficient mechanical strength to withstand any stresses. However, as a result of the relatively thick electrolyte, ionic resistance across the electrolyte is large for this design. The best performing SOFC cells of recent design are the anode-supported cells in which the mechanical strength is provided by a thick (~ 1.5 mm) layer of anode (usually nickel-YSZ cermet) material [19]. Thin electrolyte and cathode layers are deposited on the anode material by screen printing or other techniques. This design has exhibited very high performance in SOFC tests. Some researchers have suggested that the best performance for the electrolysis mode of operation could be obtained using air-side (e.g., LSM) electrode-supported cells [20]. A wealth of additional information on materials, configurations, and designs of solid-oxide electrochemical systems is available in reference [21].

The highest energy density configuration for a high-temperature electrolysis stack is the planar geometry. A cross-section of a planar stack design is shown again in Fig. 11. The design depicted in the figure shows an electrolyte-supported cell with a nickel cermet cathode and a perovskite anode such as strontium-doped lanthanum manganite (LSM). The flow fields conduct electrical current through the stack and provide flow passages for the process gas streams. The separator plate or bipolar plate separates the process gas streams. It must also be electrically conducting and is usually metallic, such as a ferritic stainless steel. The electrochemical half-cell reactions are shown in the figure. At the steam-hydrogen electrode-electrolyte interface (cathode in the electrolysis mode), the steam is electrochemically reduced according to

$$H_2O + 2e^- \rightarrow H_2 + O^{2-} . \quad (31).$$

This net reaction can be further subdivided mechanistically as:

$$H_2O \rightarrow 2H^+ + O^{2-} \quad (32)$$

$$2H^+ + 2e^- \rightarrow H_2 . \quad (33)$$

At the oxygen electrode-electrolyte interface (anode in the electrolysis mode), oxygen is produced according to

$$2O^{2-} \rightarrow$$

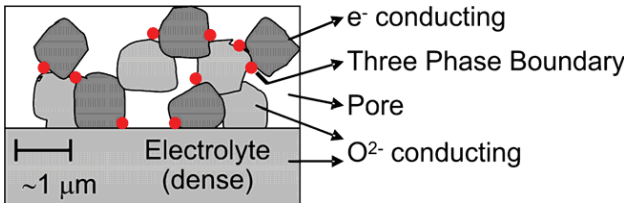

Figure 12. Triple phase boundary (TPB) sites in a solid oxide cell, shown as red dots [45].

The electrons are driven from the anode to the cathode by means of an external power source. The electrolyte conducts the oxygen ions from the cathode to the anode where they liberate their extra electrons to the external circuit. These electrochemical reactions occur at the electrode-electrolyte interface at active triple-phase boundary (TPB) sites where the ionic, electronic, and gas phases meet. These sites therefore correspond to locations where electrode, electrolyte, and gas are all in contact. At the steam-hydrogen electrode, a supply of gas in the porous electrode, a means of transporting oxygen ions to the electrolyte, and a source of electrons from the electronically conducting Ni phase are simultaneously required. Consequently, for a TPB to be an active reaction site, the electrode must be porous, Ni grains must be in electrical contact with the interconnect plate and simultaneously in contact with the ionic and gas phases, and electrolyte grains must be in contact with the bulk electrolyte either directly or via electrolyte grains dispersed in the electrode, as shown in Fig. 12. Changes in the electrode-electrolyte interfaces and grain boundaries are highly influential in the degradation of the cell. These interfaces not only provide the TPB, but are also active for mass transport, diffusion, and segregation of species involved in the electrochemical reactions during operation. Microstructural changes in the interfacial regions, such as impurity segregation, will also affect the cell performance.

The majority of the electrolysis stack testing that has been performed at INL to date has been with planar stacks fabricated by Ceramatec, Inc. of Salt Lake City, UT. An exploded view of the internal components of one of these stacks is shown in Fig. 13. The cells have an active area of 64 cm^2. The stacks are designed to operate in cross flow, with the steam / hydrogen gas mixture flowing from front to back in the figure and air flowing from right to left. Air flow enters at the rear though an air inlet manifold and exits at the front directly into the furnace. A photograph of a 10-cell stack is provided in Fig. 14. The steam/hydrogen inlet and outlet manifolds are visible in the photograph. The power lead attachment tabs, integral with the upper and lower interconnect plates are also visible in Figs. 13 and 14. Stack operating voltages were measured using wires that were directly spot-welded onto these tabs. The interconnect plates are fabricated from ferritic

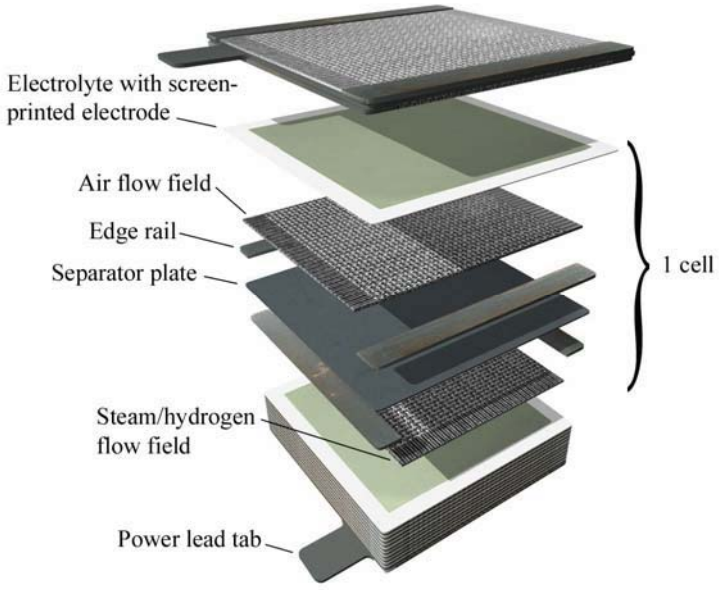

Figure 13. Exploded view of electrolysis stack components.

stainless steel. Each interconnect includes an impermeable separator plate (~0.46 mm thick) with edge rails and two corrugated "flow fields," one on the air side and one on the steam/hydrogen side. The height of the flow channel formed by the edge rails and flow fields is 1.0 mm. Each flow field includes 32 perforated flow channels across its width to provide uniform gas-flow distribution. The steam/ hydrogen flow fields are fabricated from nickel foil. The air-side flow fields are ferritic stainless steel. The interconnect plates and flow fields also serve as electrical conductors and current distributors. To improve performance, the air-side separator plates and flow fields are pre-surface-treated to form a rare-earth stable conductive oxide scale. A perovskite rare-earth coating is also applied as a bond layer to the separator-plate oxide scale by either screen printing or plasma spraying. On the steam/hydrogen side of the separator plate, a thin (~10 μm) nickel metal coating is applied as a bond layer.

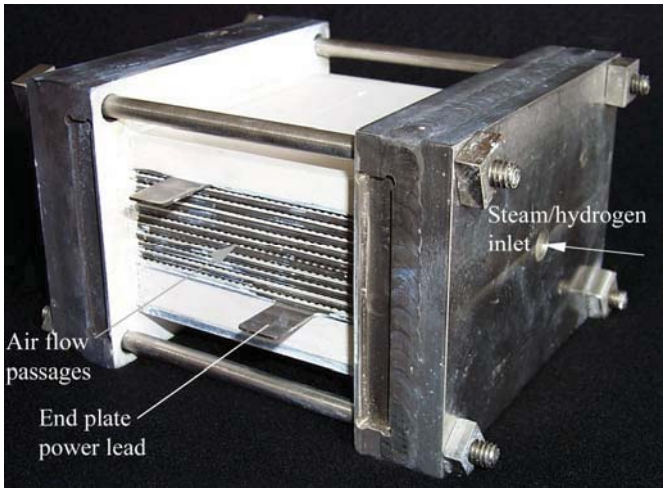

Figure 14. Detail of 10-cell short stack.

The stack electrolytes are scandia-stabilized zirconia, about 140 μm thick. The air-side electrodes (anode in the electrolysis mode), are a strontium-doped manganite. The electrodes are graded, with an inner layer of manganite/ zirconia (~13 μm) immediately adjacent to the electrolyte, a middle layer of pure manganite (~18 μm), and an outer bond layer of cobaltite. The steam/ hydrogen electrodes (cathode in the electrolysis mode) are also graded, with a nickel-zirconia cermet layer (~13 μm) immediately adjacent to the electrolyte and a pure nickel outer

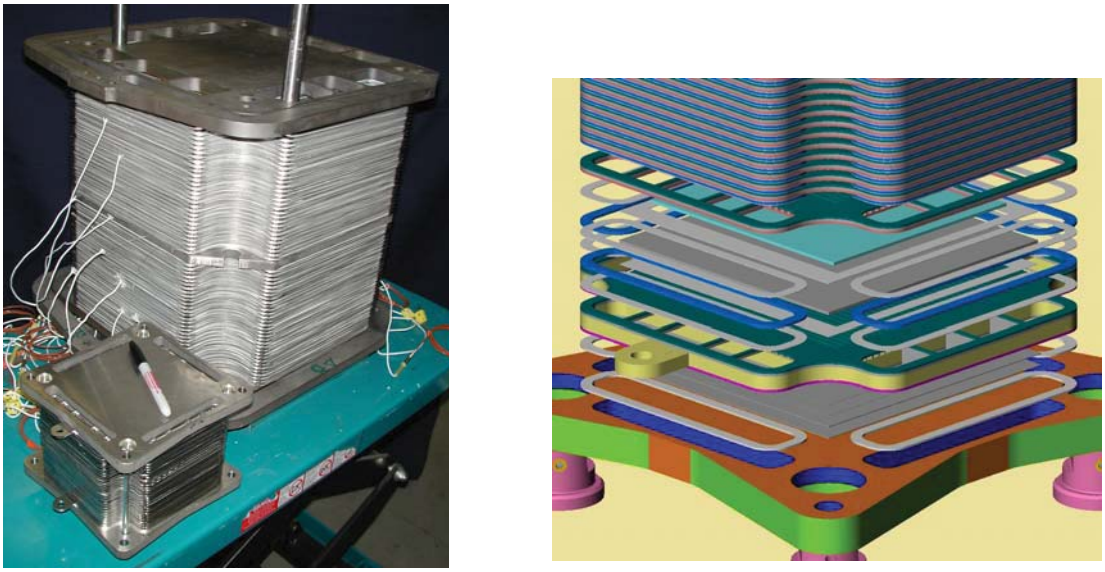

Figure 15. Planar stack with anode-supported cells, developed by Versa Power.

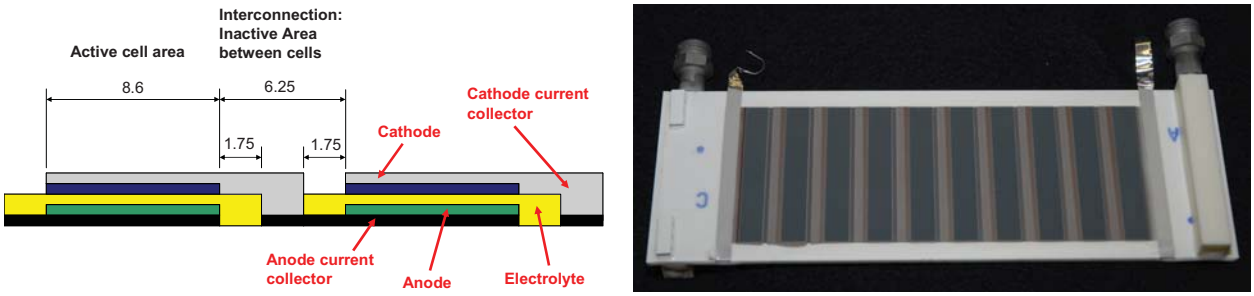

Figure 16. Rolls Royce integrated planar cells; (a) schematic of cells layers, (b) photograph of IP-SOFC tube.

layer (~10 μm).

Planar stacks can also be assembled using electrode-supported cells. Advanced technology SOFC stacks based on anode-supported cell technology have been developed by several manufacturers under the Solid-State Energy Conversion Alliance (SECA) [19] program. For example, Versa Power (partnered with Fuel Cell Energy) has developed anode-supported planar cells with dimensions as large as 33 × 33 cm. Their stacks are internally manifolded, as shown in Fig. 15. INL is in the process of establishing a CRADA with Versa Power to assess the performance of their cells and stacks operating in the electrolysis mode.

Additional cell and stack configurations are under development for SOFC applications, including tubular and integrated planar designs. INL participated in a CRADA with Rolls Royce Fuel Cell Systems (RRFCS) to evaluate the performance of their cells operating in the electrolysis mode. The RRFCS cells utilize a segmented-in-series integrated planar (IP-SOFC) design in which thin electrode and electrolyte layers are screen printed on the surface of a flattened ceramic tube, as shown in Fig. 16. Fig 16(a) is a schematic representation of the electrochemical layers. Fig. 16(b) is a photograph of one of the tubes that were tested at INL.

3. INL HTE EXPERIMENTAL PROGRAM

3.1 Small-scale tests

The experimental program at INL includes a range of test activities designed to characterize the performance of solid-oxide cells operating in the electrolysis mode. Small-scale activities are intended to examine candidate electrolyte, electrode, and interconnect materials with single cells and small stacks. Initial cell and stack performance and long-term degradation characteristics have been examined. Larger scale experiments are designed to demonstrate the technology and to address system-level issues such as hydrogen recycle and heat recuperation.

A photograph of the INL high-temperature electrolysis laboratory is shown in Fig. 17. This part of the laboratory is dedicated to small-scale experiments with single cells and small stacks. The laboratory is currently being upgraded and will soon include three furnaces for single and button cell tests, plus two larger furnaces for stack testing. A schematic of the experimental apparatus used for single-cell testing is presented in Fig. 18. The schematic for stack testing is similar. Primary components include gas supply cylinders, mass-flow controllers, a humidifier, on-line dewpoint and CO_2 measurement stations, temperature and pressure measurement, high temperature furnace, a solid oxide electrolysis cell, and a gas chromatograph. Nitrogen is used as an inert carrier gas. Carbon dioxide and related instrumentation is included for co-electrolysis

Figure 17. High-temperature electrolysis laboratory at INL – small-scale experiments.

experiments. Inlet flow rates of nitrogen, hydrogen, carbon dioxide and air are established by means of precision mass-flow controllers. Hydrogen is included in the inlet flow as a reducing gas in order to prevent oxidation of the Nickel cermet electrode material. Air flow to the stack is supplied by the shop air system, after passing through a two-stage extractor / dryer unit. The cathode-side inlet gas mixture, consisting of hydrogen, nitrogen, and possibly carbon dioxide (for coelectrolysis tests) is mixed with steam by means of a heated humidifier. The dewpoint temperature of the nitrogen / hydrogen / CO_2 / steam gas mixture exiting the humidifier is monitored continuously using a precision dewpoint sensor. All gas lines located downstream of the humidifier are heat-traced in order to prevent steam condensation. Inlet and outlet CO_2 concentrations are also monitored continuously using on-line infra-red CO_2 sensors, when applicable.

For single button-cell testing, an electrolysis cell is bonded to the bottom of a zirconia tube, using a glass seal. During testing, the tube is suspended in the furnace. The cells are electrolyte-supported with a scandia-stabilized zirconia electrolyte, about 150 μm thick. The outside electrode, which is exposed to air, acts as the cathode in fuel cell mode and the anode in electrolysis mode. This electrode is a doped manganite. The inside steam-hydrogen electrode (electrolysis cathode) material is a nickel cermet. Both button-cell electrodes incorporate a platinum wire mesh for current distribution and collection. The button cells include both an active cell area (2.5 cm^2 for the cell shown) and a reference cell area. The active cell area is wired with both power lead wires and voltage taps. The reference cell area is wired only with voltage taps, allowing for continuous monitoring of open-cell potential. The power lead and voltage wires are routed to the far end of the zirconia tube via several small-diameter alumina tubes fixed to the outside of the zirconia manifold tube. A type-K stainless-steel sheathed thermocouple is mounted on the manifold tube and bent around in front of the button cell in order to allow for continuous monitoring of the button-cell temperature. The inlet gas mixture enters this tube, directing the gas to the steam/hydrogen/CO_2 side (inside) of the cell. The cell is maintained at an appropriate operating temperature (800 to 850°C) via computer-based feedback control. The furnace also preheats the inlet gas mixture and the air sweep gas. Oxygen produced

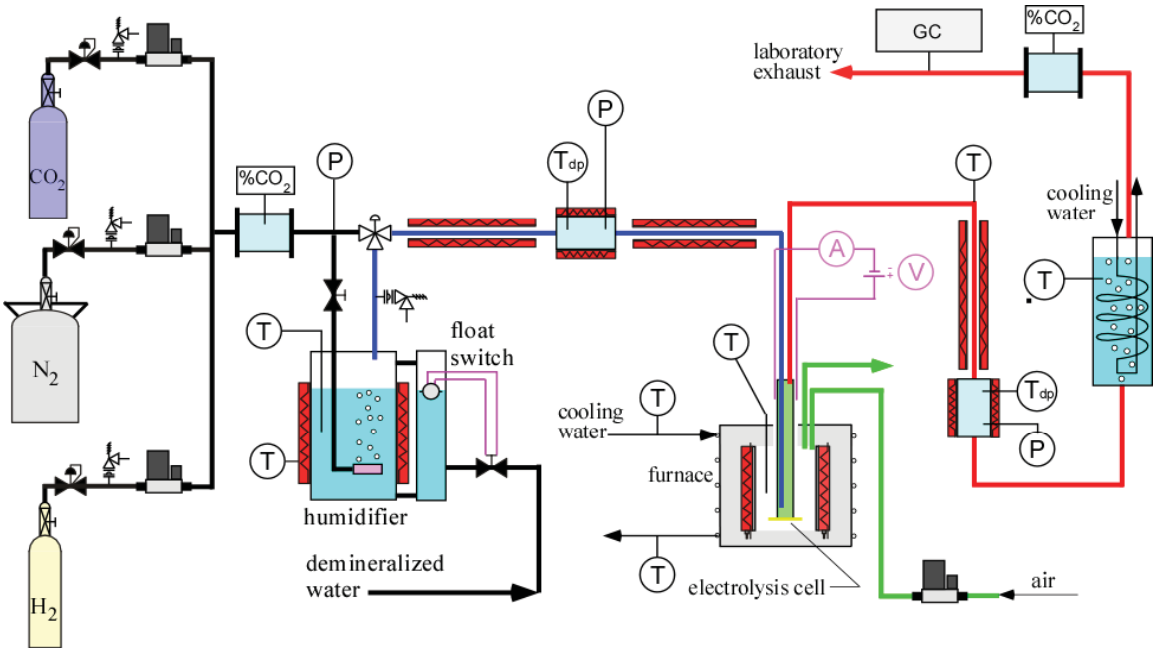

Figure 18. Schematic of single-cell co-electrolysis test apparatus.

by electrolysis is captured by the sweep gas stream and expelled into the laboratory. The product stream exits the zirconia tube and is directed towards the downstream dewpoint and CO_2 sensors and then to a condenser through a heat-traced line. The condenser removes most of the residual steam from the exhaust. The final exhaust stream is vented outside the laboratory through the roof. Rates of steam and CO_2 electrolysis are monitored by the measured change in inlet and outlet steam and CO_2 concentration as measured by the on-line sensors. In addition, a Gas Chromatograph (GC) has been incorporated into the facility downstream of the condenser to precisely quantify the composition of the dry constituents in the electrolysis product stream (including any CH_4 that may be produced).

The majority of the stack testing that has been performed at INL to date has been with planar stacks fabricated by Ceramatec, Inc. of Salt Lake City, UT, such as those shown in Figs. 13 and 14. The cells have an active area of 64 cm^2. The stacks are designed to operate in cross flow, with the steam / hydrogen gas mixture flowing from front to back in the figure and air flowing from right to left. Air flow enters at the rear though an air inlet manifold and exits at the front directly into the furnace. The power lead attachment tabs, integral with the upper and lower interconnect plates are also visible in Figs. 13 and 14. Stack operating voltages were measured using wires that were directly spot-welded onto these tabs. The interconnect plates are fabricated from ferritic stainless steel. Each interconnect includes an impermeable separator plate (~0.46 mm thick) with edge rails and two corrugated "flow fields," one on the air side and one on the steam/hydrogen side. The height of the flow channel formed by the edge rails and flow fields is 1.0 mm. Each flow field includes 32 perforated flow channels across its width to provide uniform gas-flow distribution. The steam/ hydrogen flow fields are fabricated from nickel foil. The air-side flow fields are ferritic stainless steel. The interconnect plates and flow fields also serve as electrical conductors and current distributors. To improve performance, the air-side separator plates and flow fields are pre-surface-treated to form a rare-earth stable conductive oxide scale. A perovskite rare-earth coating is also applied as a bond layer to the separator-plate

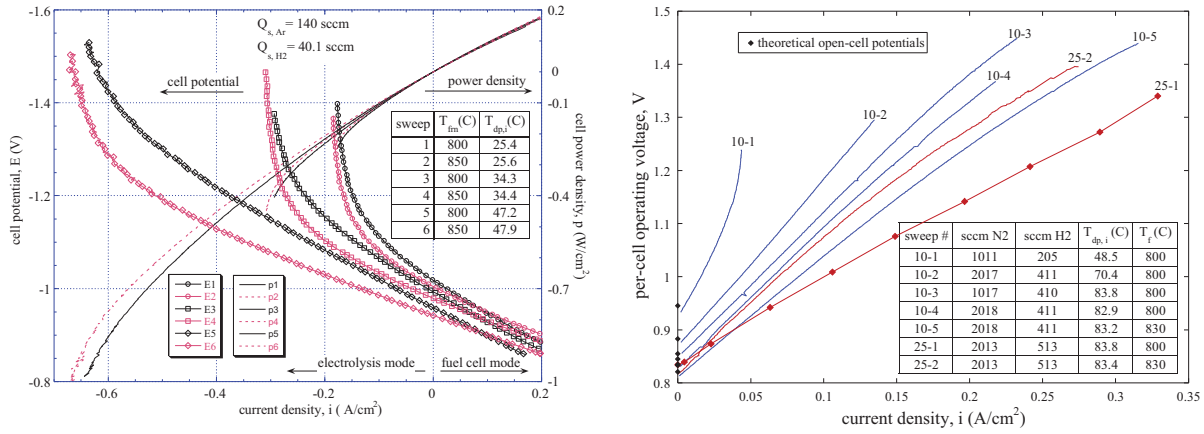

(a) (b)

Figure 19. Polarization curves; (a) button cell, (b) planar stack.

oxide scale by either screen printing or plasma spraying. On the steam/hydrogen side of the separator plate, a thin (~10 μm) nickel metal coating is applied as a bond layer.

The stack electrolytes are scandia-stabilized zirconia, about 140 μm thick. The air-side electrodes (anode in the electrolysis mode), are a strontium-doped manganite. The electrodes are graded, with an inner layer of manganite/ zirconia (~13 μm) immediately adjacent to the electrolyte, a middle layer of pure manganite (~18 μm), and an outer bond layer of cobaltite. The steam/ hydrogen electrodes (cathode in the electrolysis mode) are also graded, with a nickel-zirconia cermet layer (~13 μm) immediately adjacent to the electrolyte and a pure nickel outer layer (~10 μm).

Results of initial single (button) cell HTE tests completed at the INL were documented in detail in reference [22]. Button cell tests are useful for basic performance characterization of electrode and electrolyte materials and of different cell designs (e.g., electrode-supported, integrated planar, tubular). Polarization curves for several representative DC potential sweeps are presented in Fig. 19(a). Both the applied cell potentials and the corresponding power densities are plotted in the figure as a function of cell current density. Positive current densities indicate fuel cell mode of operation and negative current densities indicate electrolysis mode. Cell potential values at zero current density correspond to open-circuit potentials, which depend on the furnace temperature and the gas composition. The three sweeps acquired at 800ºC (sweeps 1, 3, and 5) have a steeper E-i slope, due to the lower zirconia ionic conductivity at the lower temperature. The continuous nature of the E-i curves across the zero-current-density (open-circuit) point provides no indication of significant activation overpotential for these electrolyte-supported cells. In the electrolysis mode, the voltage data vary linearly with current density up to a value that depends on the inlet steam flow rate, which for a fixed dry-gas flow rate depends on the inlet dewpoint temperature. For low inlet dewpoint values (sweeps 1 and 2), the voltage begins to increase rapidly at relatively low values of current density (~ -0.15 A/cm^2), due to steam starvation. For higher inlet dewpoints, the steam starvation effect is forestalled to higher current densities. The single-cell results demonstrated the feasibility of HTE for hydrogen production with linear operation from the fuel-cell to the electrolysis mode.

Results of initial short-stack HTE tests performed at INL are provided in references [23, 24]. A good summary of our experience is provided by the results plotted in Fig. 19(b), from [24].

Results of several representative sweeps are shown in the form of polarization curves, representing per-cell operating voltage versus current density. Test conditions for each of the seven sweeps are tabulated in the figure. Five of the sweeps were obtained from a 10-cell stack (sweeps 10-1 through 10-5) and two were obtained from a 25-cell stack (25-1 and 25-2). Theoretical open-cell potential values are shown in the figure for each sweep using a single data point at zero current density. Note that the measured open-cell potentials are in excellent agreement with the theoretical values for each sweep. Sweep 10-1 was performed with a relatively low inlet steam flow rate, corresponding to the low inlet dewpoint value of 48.5ºC and relatively low nitrogen and hydrogen flow rates. This sweep has a relatively high slope on i-V coordinates, indicating a relatively high ASR. This sweep also clearly shows the effects of steam starvation; the slope of the *i-V* curve increases dramatically as the current density is increased. The outlet dewpoint temperature corresponding to the highest current density shown in this figure was only 4ºC for this sweep. Sweep 10-2 was performed at an intermediate steam concentration, with an inlet dewpoint temperature of 70ºC. This sweep exhibits nearly linear behavior over the range of current densities shown, with a much smaller slope than sweep 10-1. Sweeps 10-3 and 10-4 are nearly linear at low current densities, then slightly concave-down at higher current densities. Sweep 10-5 has a shallower slope than the others, consistent with the higher operating temperature of 830ºC. Sweep 25-1 was performed in a stepwise fashion, rather than as a continuous sweep. This was done in order to ensure sufficient time for the internal stack temperatures to achieve steady-state values at each operating voltage. Note that the slope of this sweep is small, indicating low *ASR* (~1.5 $\Omega \cdot cm^2$). This sweep was performed at the beginning of a 1000-hour long-duration 25-cell stack test. Sweep 25-2 was acquired at the end of the long-duration test. The stack operating temperature was increased form 800°C to 830°C part way through the test. Note that the slope of sweep 25-2 is higher than that of sweep 25-1, despite the higher temperature, due to performance degradation over 1000 hours of operation.

Representative coelectrolysis results are presented in Fig. 20, from [25]. This figure shows the outlet gas composition (dry basis) from a ten-cell electrolysis stack as a function of stack current. The solid data symbols represent measurements obtained from the gas chromatograph. The lines represent predictions based on our chemical equilibrium coelectrolysis model [25]. The open data symbols show the cold inlet mole fractions of CO_2, H_2, and CO (zero). Note that these values are different than the zero-current outlet compositions shown in the figure. Even without any electrolysis, the reverse-shift reaction occurs in the stack at 800°C, resulting in the production of some CO and consumption of CO_2 and H_2. During coelectrolysis, the mole fractions of CO_2 and steam (not shown in Fig. 20) decrease with current, while the mole fractions of H_2 and CO increase. For the conditions chosen for these tests, the ratio of H_2 to CO is close to the desired 2-to-1 value for syngas

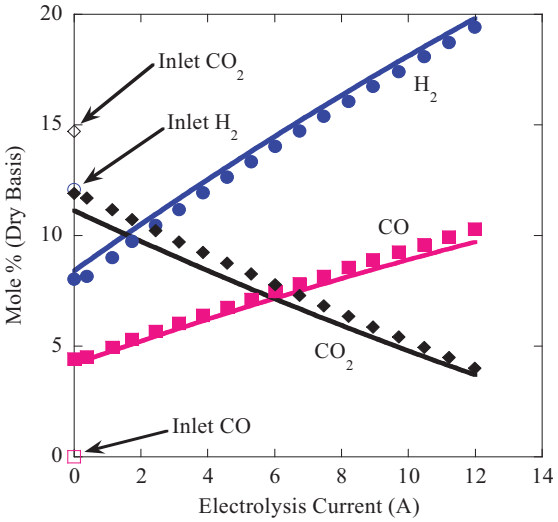

Figure 20. Outlet gas composition as a function of current density for co-electrolysis experiments, 10-cell stack.

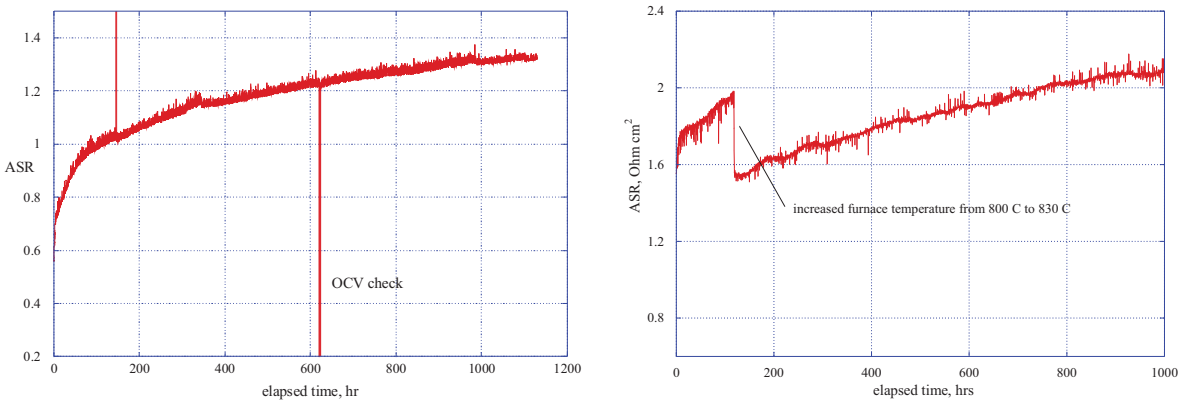

Figure 21. (a) Area-specific resistance of a button cell as a function of time for 1100-hour test; (b) Area-specific resistance of a 25-cell stack as a function of time for a 1000-hour test.

production.

3.2 Degradation.

The issue of long-term performance degradation is critical if the potential of large-scale hydrogen production based on HTE is ever to be realized. Performance degradation is also an important issue for solid-oxide fuel cells (SOFCs) and addressing this issue has been a major focus of both the US DOE SECA program [19] and the European Real-SOFC program [26]. Significant progress has been made in identifying and mitigating degradation mechanisms in SOFCs. But the electrolysis mode of operation presents some unique possible degradation mechanisms that have received much less attention. Observations of long-term performance degradation of solid-oxide electrolysis cells have been documented at INL. It should be noted that most of the cells and stacks tested at INL utilize scandia-stablized zirconia (ScSZ) electrolyte-supported cells which do not necessarily represent the state-of-the-art in cell design. Furthermore, the scandia dopant level in these cells was only about 6 mol%, which is not high enough to be considered fully stabilized. ScSZ with dopant levels less than 10% have been shown to exhibit an aging effect with annealing at 1000°C [27].

Long-term degradation in button cell tests can only be due to degradation of the electrodes, the electrolyte, or electrode-electrolyte delamination. There are no effects associated with corrosion, contact resistance, flow fields, or interconnects, since these components are not present. Results of one long-term button-cell test are presented in Fig. 21(a). This figure shows the area-specific resistance (ASR) of a button cell plotted as a function of time over the duration of an 1100 – hour test. The ASR increases relatively rapidly at the start of the test from an initial value of ~0.6 Ohm cm^2 to a value of 0.9 Ohm cm^2 over about 40 hours. Between 100 hours and 1100 hours, the ASR increases from 0.98 Ohm cm^2 to 1.33 Ohm cm^2. If the initial 100 hours is considered to be a cell conditioning period, the degradation rate over the following 1000 hours is about 35%. This is obviously an unacceptable rate of degradation. As a comparison, the Phase-III SECA target degradation rate is 0.1%/1000 hr. Several companies are currently coming very close to meeting that target in the SOFC mode of operation.

Performance degradation results with an SOEC stack tested at INL were also presented in [24]. Results of a 1000-hour test performed with a 25-cell stack are presented in Fig. 21(b).

This figure provides a plot of the stack area-specific resistance as a function of time for the 1000 hours. The furnace temperature was increased from 800 to 830°C an elapsed time of 118 hours, resulting in a sudden drop in ASR. The increase in ASR with time represents degradation in stack performance. The degradation rate decreases with time and is relatively low for the last 200 hours of the test. However, from the 118-hour mark to the end of the test, the ASR increased more than 40% over approximately 900 hours. Reduction of this performance degradation is an objective of ongoing research.

3.3. Large-Scale Demonstration – The INL Integrated laboratory Scale Facility

One of the objectives of the INL HTE program is technology scale-up and demonstration. To this end, the INL has developed a 15 kW HTE test facility, termed the Integrated Laboratory Scale (ILS) HTE test facility. Details of the design and initial operation of this facility are documented in references [28 -30]. A condensed description of the facility will be provided here. The ILS includes three electrolysis modules, each consisting of four stacks of 60 cells, yielding 240 cells per module and 720 cells total. The cells are similar to those discussed earlier. Each electrolysis module utilizes an independent support system supplying electrical power for electrolysis, a feedstock gas mixture of hydrogen and steam (and sometimes nitrogen), a sweep gas, and appropriate exhaust handling. Each module includes a controlled inlet flow of deionized water, a steam generator, a controlled inlet flow of hydrogen, a superheater, inlet and outlet dewpoint measurement stations, a condenser for residual steam, and a hydrogen vent. All three modules were located within a single hot zone. Heat recuperation and hydrogen product recycle were also incorporated into the facility. An overview photograph of the ILS is provided in Fig. 22.

An exploded view of one of the ILS module assemblies including the recuperative heat exchanger, base manifold unit, and four-stack electrolysis unit is presented in Fig. 23. For each four-stack electrolysis module, there were two heat exchangers and one base manifold unit.

Figure 22. INL 15 kW Integrated Laboratory Scale HTE test facility.

Each base manifold unit has nine flow tubes entering or exiting at its top and only four flow tubes entering or exiting at the bottom of the unit and at the bottom of the heat exchangers, thereby reducing the number of tube penetrations passing through the hot zone base plate from nine to just four. This feature also reduces the thermal load on the hot zone base plate. An internally manifolded plate-fin design concept was selected for this heat recuperator application. This design provides excellent configuration flexibility in terms of selecting the number of flow elements per pass and the total number of passes in order to satisfy the heat transfer and pressure drop requirements. Theoretical counterflow heat exchanger performance can be approached with this design. This design can also accommodate multiple fluids in a single unit. More details of the design of the recuperative heat exchangers are provided in [31].

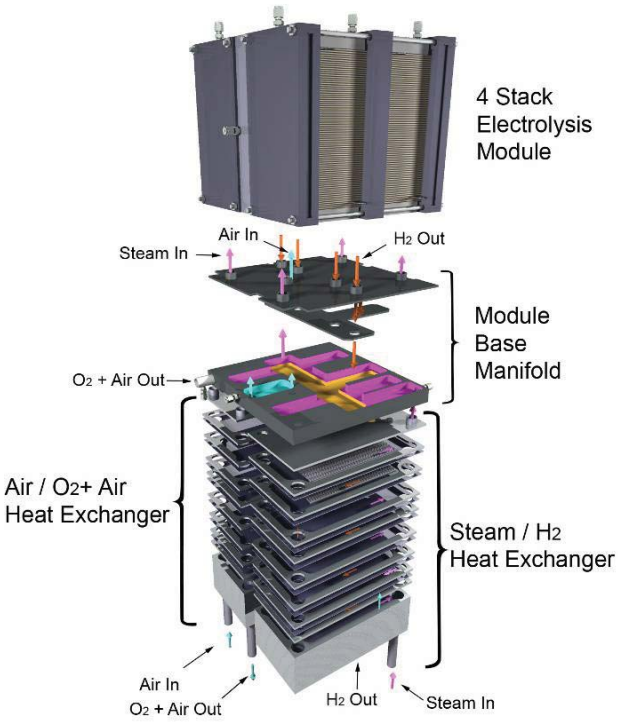

Figure 23. Exploded view of heat exchanger, base manifold unit, and four-stack electrolysis unit.

Fig. 24 shows a cut-away design rendering of the three ILS electrolysis modules with their base manifolds and heat exchangers beneath. This illustration also shows the instrumentation wires for intermediate voltage and temperature readings. Each module is instrumented with twelve 1/16" sheathed thermocouples for monitoring gas temperatures in the electrolysis module manifolds and in the base manifold. These thermocouples are attached to the manifolds using compression fittings. There are also twelve miniature 0.020" diameter inconel-sheathed type-K thermocouples per module that are used for monitoring internal stack temperatures. Access to the internal region of the stacks is provided via the air outlet face. The internal thermocouples are inserted into the small exit air flow channels. Similarly, seven intermediate voltage tap wires per module are inserted into the air flow channels of the four stacks.

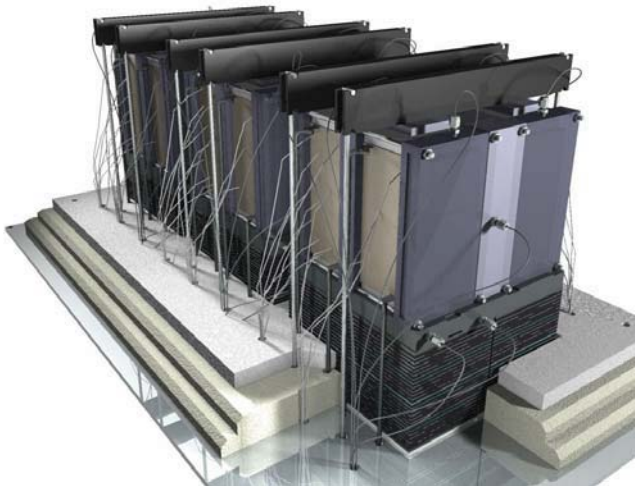

Figure 24. ILS modules, mounted in hot zone.

Two compression bars are shown across the top of each module in Fig. 24. These bars are used to maintain compression on all of the stacks during operation in order to minimize electrical contact resistance between the cells, flow fields, and interconnects. The bars are held in compression via spring-loaded tie-

Figure 25. HTE ILS hot zone with three modules installed.

downs located outside of the hot zone under the base plate.

Note that the heat exchangers are partially imbedded in the insulation thickness. The top portion of each heat exchanger is exposed to the hot zone radiant environment, which helps to insure that the inlet gas streams achieve the desired electrolyzer operating temperature prior to entering the stacks. The temperature at the bottom of each heat exchanger will be close to the inlet stream temperature, minimizing the thermal load on the hot zone base plate in the vicinity of the tubing penetrations. A photograph of the three ILS electrolysis modules installed in the hot zone is shown in Fig. 25.

Performance degradation with the ILS system is documented in Fig. 26. Over a period of 700 hours of test time, module-average ASR values increased by about a factor of 5, from an initial value near 1.5 Ohm·cm^2. Some of the observed degradation was related to balance-of-plant issues. For example, prior to about 480 hours of operation, unanticipated condensation occurred in the hydrogen recycle system which led to erratic control of the hydrogen recycle flow rate due to the intermittent presence of liquid water in the mass flow controllers. This problem resulted in time periods during which there may have been no hydrogen flow to the ILS stacks, leading to accelerated performance degradation associated with oxidation of the nickel cermet electrodes. Despite the problems with the ILS, we were able to successfully demonstrate large-scale hydrogen production with heat recuperation and hydrogen recycle, as would be required in a large-scale plant. A plot of the time history of ILS hydrogen production is given in Fig. 26. Peak electrolysis power consumption and hydrogen production rate were

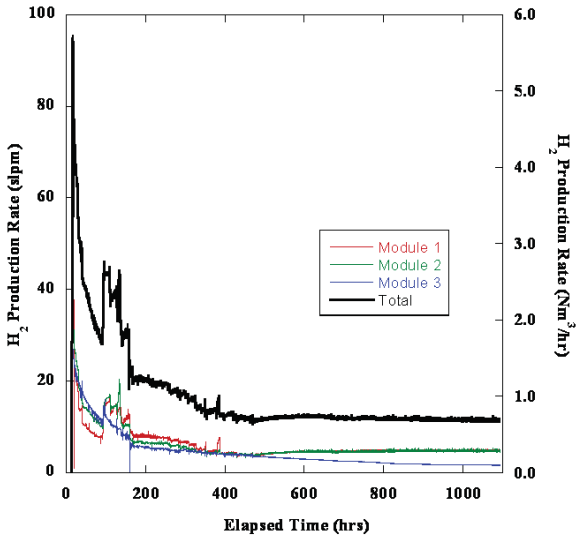

Figure 26. Time history of ILS hydrogen production rate.

18 kW and 5.7 Nm^3/hr, respectively, achieved at about 17 hours of elapsed test time.

3.4. Single Cell Tests – Anode-Supported Cells

INL is currently in the process of testing several state-of-the-art single 5 cm x 5 cm anode-supported cells in the electrolysis mode. A new test apparatus has been developed for this purpose. Referring to the exploded view given in Fig. 27, the steam hydrogen mixture enters through the inlet hole in the bottom of the HastX base plate. It then flows through a diverging flow channel milled into the HastX base plate and passes through a slot in the bottom of the alumina cell holder. The steam/hydrogen then flows under the cell through a corrugated/perforated nickel flow field. A nickel foil underneath the flow field will serve as a current collector. A power lead and voltage tap double-ended wire will be spot welded to the nickel foil and will be situated in one of the grooves of the flow field. These wires will be fed out through holes in the bottom of the alumina cell holder. There will also be a nickel mesh (not shown) in direct contact with the anode above the flow field. A nickel paste will be used to enhance electrical contact between the cell and the nickel mesh, flow field, and foil. The steam-hydrogen flow exits through a slot in the cell holder and then through a converging flow channel cut into the base plate and out through the steam/H_2 outlet hole in the base plate.

Air is introduced to the cathode side of the cell through holes in the HastX top plate and the alumina air flow distributor. The air flow inlet tube will be welded to the HastX top plate and will protrude into the hole in the alumina air flow distributor. A seal will be formed between the HastX top plate and the alumina air flow distributor by means of a mica gasket or ceramic paste. After exiting the air flow distributor, the air will impinge on the air side of the cell and flow radially outward through an array of protuberances milled into the bottom side of the alumina air flow distributor plate. The air then exits into the furnace volume. A platinum or silver mesh is situated between the air flow distributor and the cathode. A platinum or silver ink will be used to enhance electrical contact between the air electrode and the mesh. A power lead/voltage tap double-ended wire will be spot-welded to the current collector mesh and will be situated in one of the grooves formed by the array of protuberances. It can then be fed out of the fixture from the side.

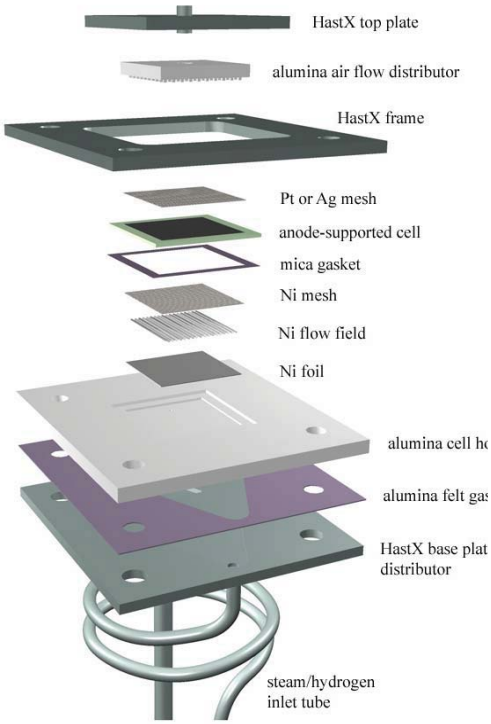

Figure 27. Exploded detail view of single cell fixture.

A fixed compressive load is applied to the entire cell stackup between the alumina cell holder and the HastX top plate by means of weights, as shown in the test stand overview, Fig. 28(a). This load must simultaneously compress the cell against the mesh, flow field and foil on the steam/hydrogen side and against the seal around the outer edge of the cell. The outer edge of the cell rests on a window frame shelf milled into the alumina cell holder. The seal will be accomplished using a high-temperature SOFC sealing paste. The weight plates are held in alignment by the upper portion of the threaded rods which extend upward for this purpose. There are eight weight plates,

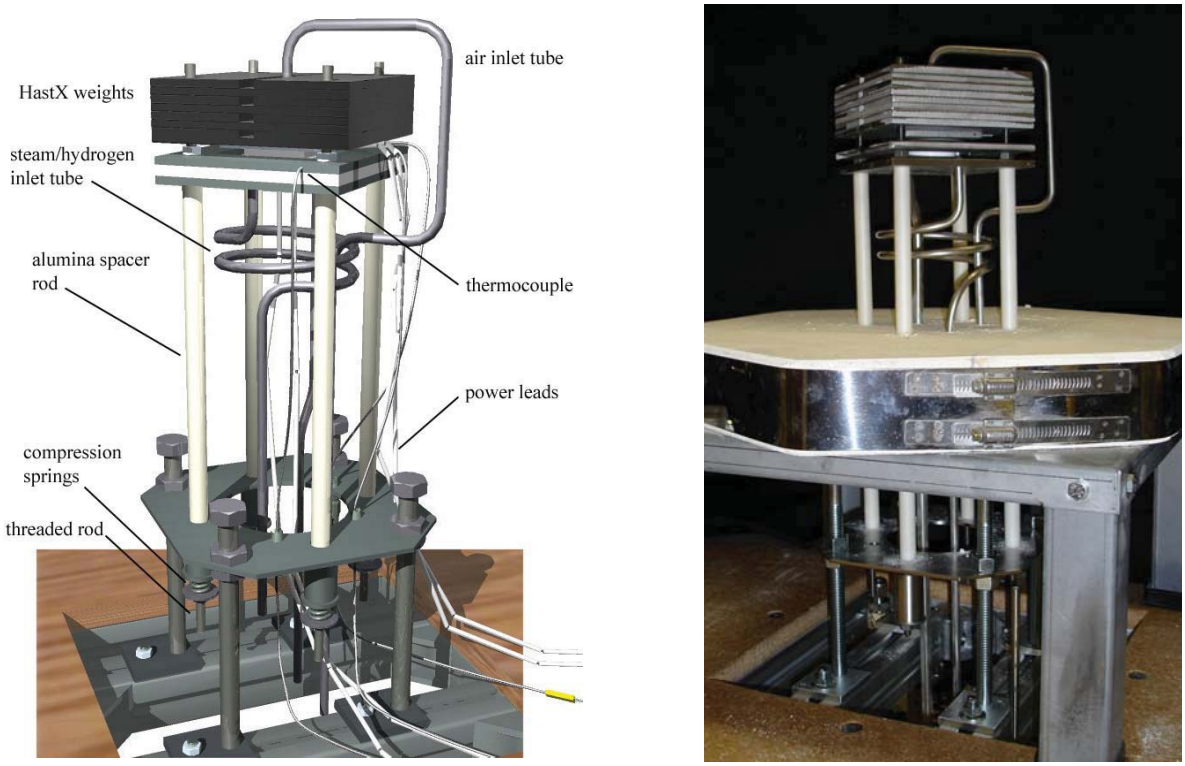

(a) (b)

Figure 28. (a) Single-cell test stand overview; (b) Assembled test fixture with furnace base.

each 1.2 lbs, for a total of 9.6 lbs, which yields a compressive pressure of about 20,000 Pa on the cell active area.

A fixed compressive load is independently applied between the HastX frame, the alumina cell holder, and the HastX base plate. This load is generated by the compression of four springs located under the test stand base support outside of the furnace. The springs will be compressed a fixed amount that is determined by the height of the spool pieces. This load is intended to compress the seal between the cell holder and the base plate. This seal will be formed by either a mica gasket or a ceramic sealing paste. A nut is visible on the threaded rod in Fig. 28 just above the HastX frame and below the weight plates. This nut represents the upper stop for this compressive load. The extension of the threaded rods above the nuts is for the purpose of aligning the weight plates. Note that the weight plates are floating above these nuts since they are resting on the HastX top plate. A photograph of the completed test fixture assembly is provided in Fig. 28(b).

The air and steam/hydrogen flow tubes have been fabricated from inconel. HastX was specified for the base plate, the frame, and the weight plates. The spacer rods are specified as alumina in order to minimize heat conduction out of the bottom of the furnace.

4. LARGE-SCALE SYSTEM ANALYSIS STUDIES

4.1. System Models

A number of detailed process models have been developed at INL for large-scale system analysis of high-temperature electrolysis plants. These analyses have been performed using

UniSim process analysis software [11]. UniSim is a derivative of HYSYS. The software inherently ensures mass and energy balances across all components and includes thermodynamic data for all chemical species. The overall process flow diagram for a very high-temperature helium-cooled reactor (VHTR) coupled to the direct helium recuperated Brayton power cycle and the HTE plant with air sweep is presented in Fig. 29 [10]. The reactor thermal power assumed for the high-temperature helium-cooled reactor is 600 MW_{th}. The primary helium coolant exits the reactor at 900°C. This helium flow is split at T1, with more than 90% of the flow directed toward the power cycle and the remainder directed to the intermediate heat exchanger to provide process heat to the HTE loop. Within the power-cycle loop, helium flows through the power turbine where the gas is expanded to produce electric power. The helium, at a reduced pressure and temperature, then passes through a recuperator and precooler where it is further cooled before entering the low-pressure compressor. To improve compression efficiencies, the helium is again cooled in an intercooler heat exchanger before entering the high-pressure compressor. The helium exits the high-pressure compressor at a pressure that is slightly higher than the reactor operating pressure of 7 MPa. The coolant then circulates back through the recuperator where the recovered heat raises its temperature to the reactor inlet temperature of 647°C, completing the cycle.

Liquid water feedstock to the HTE process enters at the left in the diagram. The water is compressed to the HTE process pressure of 3.5 MPa in the liquid phase using a pump. The HTE process is operated at elevated pressure for two reasons. Elevated pressure supports higher mass flow rates for the same size components. Furthermore, the gaseous hydrogen product will ultimately be delivered at elevated pressure either for storage or pipeline. Therefore, from the standpoint of overall process efficiency, it is logical to compress the liquid water feedstock at the process inlet since liquid-phase compression work is very small compared to compression of the gaseous product.

Downstream of the pump, condensate from the water knockout tank is recycled back into the inlet stream at M3. The water stream is then vaporized and pre-heated in the electrolysis recuperator, which recovers heat from the post-electrolyzer process and sweep-gas outlet streams. Downstream of the recuperator, at M2, the steam is mixed with recycled hydrogen product gas. A fraction of the product gas is recycled in this way in order to assure that reducing conditions are maintained on the steam/hydrogen electrode. Downstream of the mixer, the process gas mixture enters the intermediate heat exchanger (IHX), where final heating to the electrolysis operating temperature occurs, using high-temperature process heat from the nuclear reactor. The process stream then enters the electrolyzer, where the steam is electrolytically reduced, yielding hydrogen on the cathode side of each cell and oxygen on the anode side. Most of the components included in the process flow diagram are standard UniSim components. However, a custom electrolyzer module was developed at INL for direct incorporation into the UniSim system analysis code, as described in detail in reference [18].

Downstream of the electrolyzer, the hydrogen-rich product stream flows through the electrolysis recuperator where it is cooled and the inlet process stream is preheated. The cooled product stream is split at T2 and a fraction of the product gas is recycled into the inlet process stream, as discussed previously. A recirculating blower is required to repressurize the recycle stream to the upstream pressure at M2. The remainder of the product stream is cooled further at the water knockout tank, where the majority of any residual steam is condensed and separated, yielding dry hydrogen product.

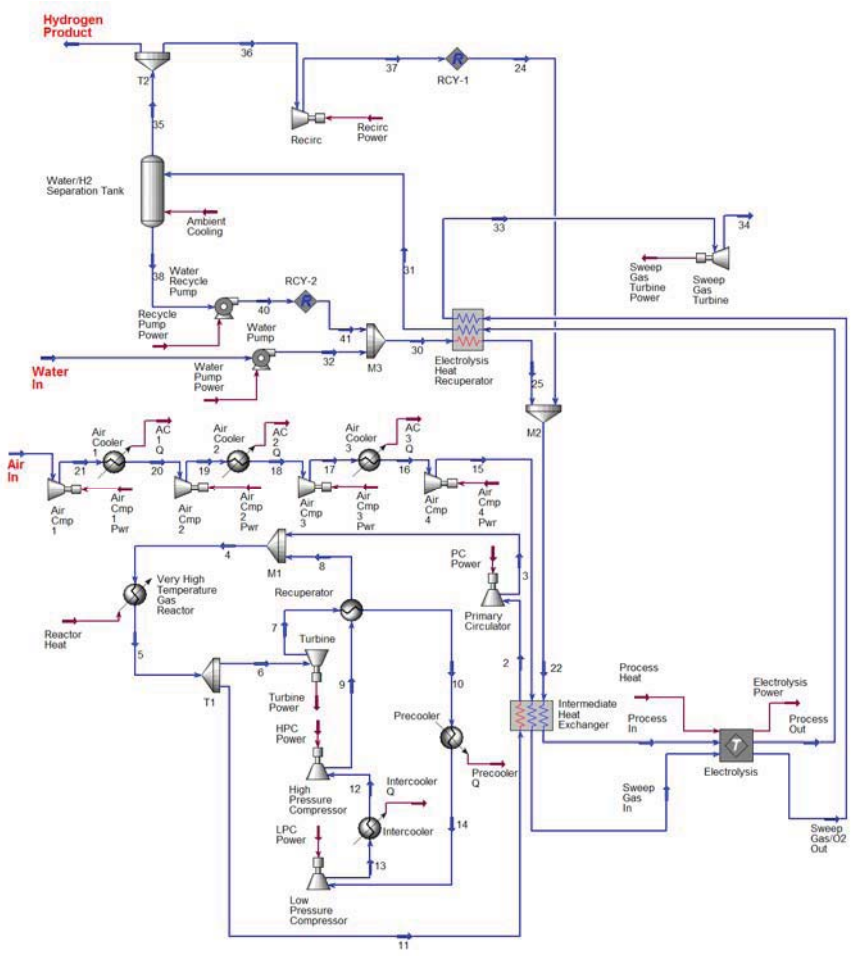

Figure 29. Process flow diagram for a helium-cooled reactor/direct Brayton/HTE system with air sweep.

The process flow diagram shows air in use as a sweep gas, to remove the excess oxygen that is evolved on the anode side of the electrolyzer. For the air-sweep cases, inlet air is compressed to the system operating pressure of 3.5 MPa in a four-stage compressor with intercooling. The final compression stage is not followed by a cooler, so the air enters the IHX at about 120°C. The sweep gas is heated to the electrolyzer operating temperature of 800°C via the IHX which supplies high-temperature nuclear process heat directly to the system. The sweep gas then enters the electrolyzer, where it is combined with product oxygen. Finally, it passes through the electrolysis recuperator to help preheat the incoming process gas. Some of the sweep gas compression work is recovered using a sweep-gas turbine located at the sweep-gas exit.

In order to avoid the work requirement associated with compression of the sweep gas, it is possible to operate with no sweep gas, and to allow the system to produce pure oxygen, which could potentially be supplied to another collocated process such as an oxygen-blown gasifier. For this mode of operation, the four-stage air compressor would not be included in the process flow diagram and there would be no air flow through the intermediate heat exchanger. Air preheat at the IHX is no longer needed. Oxygen would simply be evolved from the anode side of the electrolyzer at the electrolysis operating pressure and temperature. It would flow through the electrolysis heat recuperator and the outlet turbine. The results of our system analyses have

shown that this concept is desirable from the standpoint of overall process efficiency, but there are significant technical issues associated with handling high-temperature pure oxygen that would have to be addressed.

Similar system analyses have been performed to evaluate the concept of direct syngas production from steam and carbon dioxide using HTE. A flow diagram of the process model developed for this study is presented in Fig. 30. The primary process feedstock streams are liquid water and carbon dioxide. The inlet water stream is compressed in the liquid phase to the process operating pressure of 3.5 MPa using a pump. This operating pressure was selected because it is approximately equal to the desired operating pressure for a Fisher-Tropsch process using a cobalt catalyst. Downstream of the pump, condensate from the water knockout tank is recycled back into the inlet stream at M3. The water stream is then vaporized and pre-heated in the electrolysis recuperator, which recovers heat from the post-electrolyzer process and sweep-gas outlet streams. Downstream of the recuperator, at M2, the steam is mixed with carbon dioxide plus recycled hydrogen and carbon monoxide product gas. A fraction of the product gas is recycled in this way in order to ensure that reducing conditions are maintained on the steam/hydrogen electrode. Downstream of the mixer, the process gas mixture enters the intermediate heat exchanger (IHX), where final heating to the electrolysis operating temperature

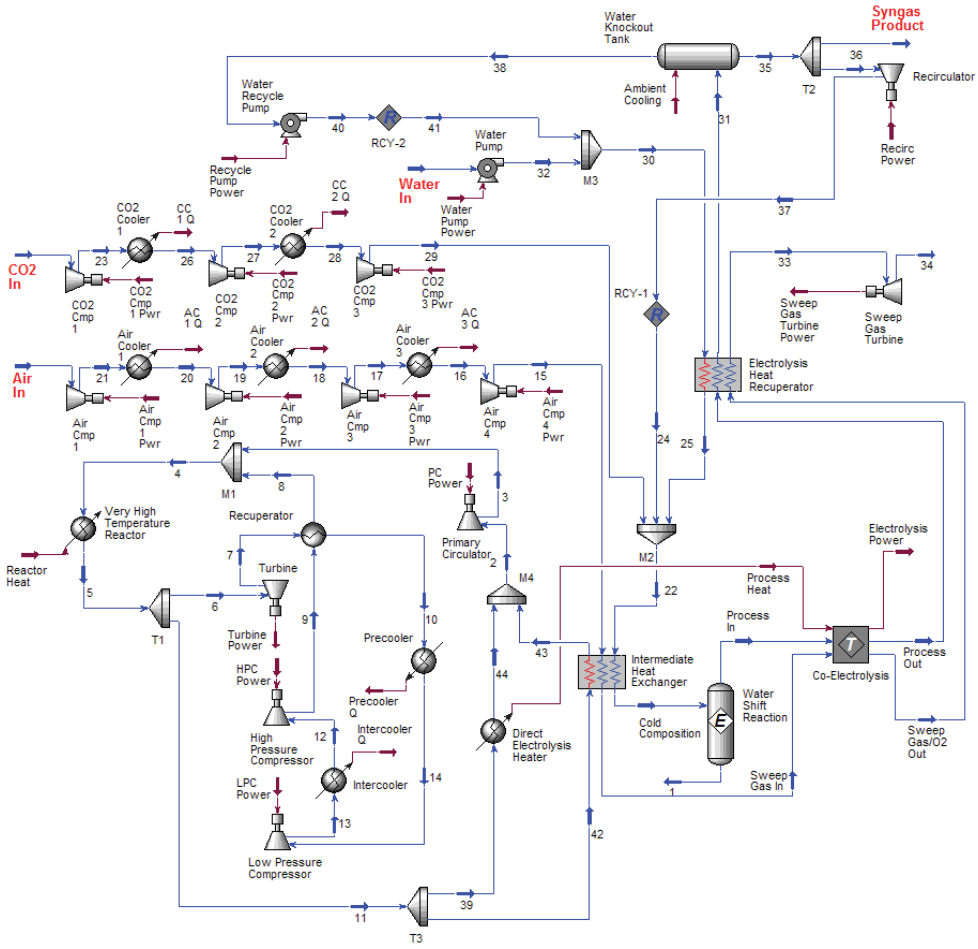

Figure 30. Process flow diagram for co-electrolysis plant.

occurs, using high-temperature process heat from the nuclear reactor. A gas shift reaction occurs with the heated gas mixture represented by an equilibrium reactor in the process flow diagram, allowing chemical equilibrium to be achieved. The process stream then enters the electrolyzer, where oxygen is electrolytically removed from the system, producing hydrogen and carbon monoxide.

For these simulations, the per-cell active area for electrolysis was assumed to be 225 cm^2. This cell size is well within the limits of current technology for planar cells. Area-specific resistance (*ASR*) was used to characterize the performance of the electrolysis cells. This parameter incorporates the loss mechanisms in the cells. The *ASR* value used in the electrolyzer module is temperature-dependent per the following Arrhenius equation:

$$ASR(T) = ASR_{1100K} - 0.463 + 3.973 \times 10^{-5} \exp\left(\frac{10300}{T(K)}\right) \tag{35}$$

where ASR_{1100K} represents the user-specified cell ASR at the temperature 1100 K (e.g., 0.25 or 1.25). This constant allows one to shift the entire *ASR* curve to higher or lower *ASR* values, to mimic lower or higher performing cells, respectively. This equation for *ASR(T)* is based on empirical data obtained from an actual operating stack, modified to allow user specification of the *ASR* value at 1100 K. In order to show the trends that can be expected with higher or lower ASR, two values of ASR_{1100K} have been included in this study. The ASR_{1100K} value of 1.25 represents a stack-average *ASR* value at 1100 K that is achievable in the short term with existing technology. The ASR_{1100K} value of 0.25 is an optimistic value that has been observed in button cells, but will be difficult to achieve in a stack in the short term. The temperature dependence of the *ASR* is important for the adiabatic cases (since the outlet temperature in these cases is generally different than the inlet temperature) and for evaluating the effect of electrolyzer inlet temperature on overall process efficiency.

The total number of cells used in the process simulations was determined by specifying a maximum current density for each *ASR* value considered that was large enough to ensure that the operating voltage would just exceed the thermal neutral voltage. For the higher nominal *ASR* value of 1.25 Ohm·cm^2, the maximum current density was set at 0.25 A/cm^2 and an adiabatic thermal boundary condition was assumed. The total number of cells for this base case was adjusted until the total remaining power was zero. In other words, the full power cycle output at this operating point is dedicated to electrolysis. This procedure resulted in 1.615×10^6 cells required. At lower current densities, the power cycle output exceeds the value required for electrolysis and this excess power would be supplied to the grid. For the case of *ASR* = 0.25 Ohm·cm^2, the maximum current density was set at 1.0 A/cm^2. A much higher maximum current density was required for the lower *ASR* case, again in order to assure that the thermal neutral voltage was just exceeded.

Two thermal boundary condition limits were considered for the electrolyzer: isothermal and adiabatic. Actual electrolyzer operation will generally lie between these limits. For the isothermal cases, heat from the reactor was directly supplied to the electrolyzer to maintain isothermal conditions for operation below the thermal neutral voltage. Heat rejection from the electrolzer is required to maintain isothermal operation at operating voltages above thermal neutral. For the adiabatic cases, the direct electrolyzer heater shown in Fig. 30 was not used.

To allow for comparisons between the performance of the HTE processes to alternate hydrogen and syngas production techniques, we have adopted a general efficiency definition that

can be applied to any thermal water-splitting, or syngas production process, including HTE, low-temperature electrolysis (LTE), thermochemical water splitting, co-electrolysis, coal-to-syngas, and biomass-to-syngas. Since the primary energy input to the thermochemical processes is in the form of heat, the appropriate general efficiency definition to be applied to all of the techniques is the overall thermal-to-hydrogen efficiency, η_H. This efficiency is defined as the heating value of the product hydrogen (plus CO for syngas production processes) divided by the total thermal input required to produce it. In this report, the lower heating value, LHV, of the products has been used:

$$\eta_H = \frac{\sum_i \dot{N}_i LHV_{i,product}}{\sum_i \dot{Q}_i + \sum_i \dot{N}_i LHV_{i,reactant}} \tag{36}$$

The denominator in this efficiency definition quantifies all of the net thermal energy that is consumed in the process plus the heating value of any feedstock reactants, such as coal or biomass. For a thermochemical process, this summation includes the direct nuclear process heat as well as the thermal equivalent of any electrically driven components such as pumps, compressors, etc. The thermal equivalent of any electrical power consumed in the process is the power divided by the thermal efficiency of the power cycle. The power-cycle thermal efficiency for the helium-cooled direct Brayton cycle concept described in this paper was 52.6%. For an electrolysis process, the summation in the denominator of Eqn. (1) includes the thermal equivalent of the primary electrical energy input to the electrolyzer and the secondary contributions from smaller components such as pumps and compressors. In additional, any direct thermal inputs are also included. Direct thermal inputs include any net (not recuperated) heat required to heat the process streams up to the electrolyzer operating temperature and any direct heating of the electrolyzer itself required for isothermal operation. Note that for co-electrolysis of steam and carbon dioxide, the numerator in Eqn. (2) includes the low heating value of the produced carbon monoxide.

4.2. System Analysis Results

4.2.1 Hydrogen Production

A summary of results obtained from the hydrogen production system analyses is presented in Figs. 31 and 32. The results presented in these figures were obtained for a fixed steam utilization of 89% (i.e., 89% of the inlet steam was converted to hydrogen). In order to maintain fixed steam utilization, the flow rates of the process streams were adjusted with lower flow rates for lower current densities and higher flow rates for higher current densities. Results of eight cases are presented in Fig. 31: low and high *ASR*, adiabatic and isothermal electrolyzer operation, air-sweep and no-sweep. The figure provides overall hydrogen production efficiencies (Eqn. 2) as a function of per-cell operating voltage. Recall that electrolyzer efficiency is inversely proportional to operating voltage [3]. Higher operating voltages yield higher current densities and higher hydrogen production rates, but lower overall efficiencies, so the selection of electrolyzer operating condition is a tradeoff between production rate and efficiency. For a specified target production rate, higher production efficiency requires a higher capital cost, since more cells would be required to achieve the target production rate. In general, a good tradeoff between production rate and efficiency occurs for operating voltages near or slightly below the thermal neutral value, around 1.29 V. This operating voltage is also desirable from the

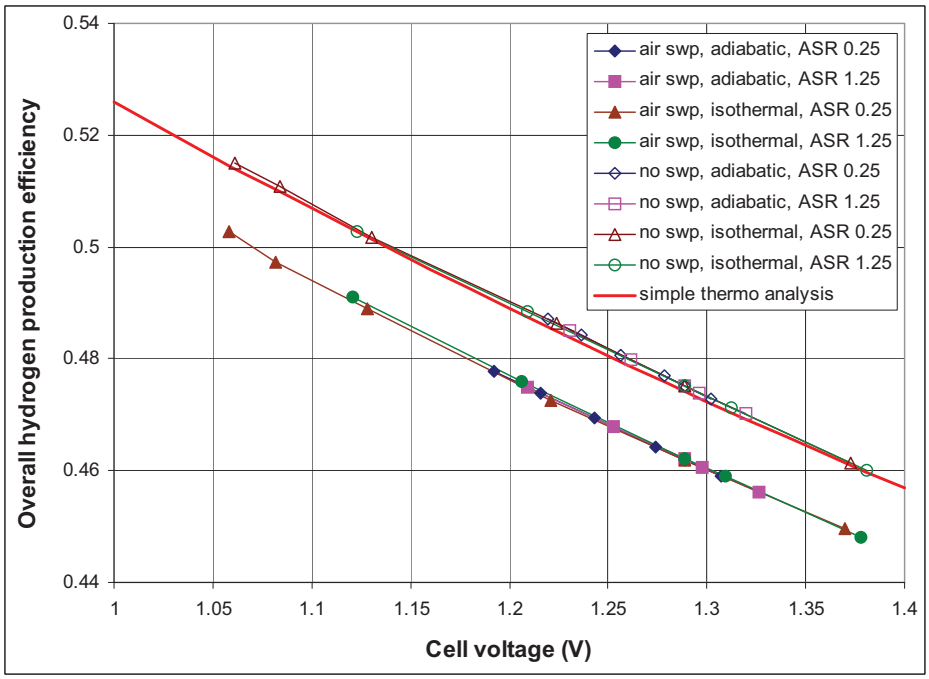

Figure 31. Overall HTE hydrogen production efficiencies for the VHTR/recuperated direct Brayton cycle, as a function of per-cell operating voltage.

standpoint that the electrolysis stack operates nearly isothermally at this voltage. Predicted overall thermal-to-hydrogen efficiency values shown in Fig. 31 are generally within 8 percentage points of the power-cycle efficiency of 52.6%, decreasing with operating voltage. It is interesting to note that the overall process efficiencies for these fixed-utilization cases collapse onto individual lines, one for the air-sweep cases and another for the no-sweep cases, when plotted as a function of per-cell operating voltage, regardless of the electrolyzer mode of operation (adiabatic or isothermal) and ASR value. Note that the highest operating voltages shown are just above the thermal neutral voltage of 1.29 V. Note also that the highest overall efficiency plotted in Fig. 31 (for no-sweep, ASR = 0.25, isothermal, V = 1.06 A/cm^2) exceeds 51%.

An additional line, based on a simple thermodynamic analysis [3] is also shown in Fig. 31. This analysis considers a control volume drawn around the electrolysis process, with the process consuming the electrical work from the power cycle, and heat from a high-temperature source. If the inlet and outlet streams are assumed to be liquid water, and gaseous hydrogen and oxygen, respectively, at $T = T^o$, $P = P^o$, direct application of the first law, Faraday's law, and the definition of the overall thermal-to-hydrogen efficiency yields:

$$\eta_H = \frac{LHV}{2FV_{op}(1/\eta_{th} - 1) + HHV} \tag{37}$$

The curve labeled "simple thermo analysis" in Fig. 31 represents Eqn. (3). This equation provides a useful reference against which detailed system analyses can be measured. The simple thermodynamic analysis agrees quite closely with the detailed system analysis results for the no-sweep cases, which correspond directly with the conditions of simple analysis since it does not

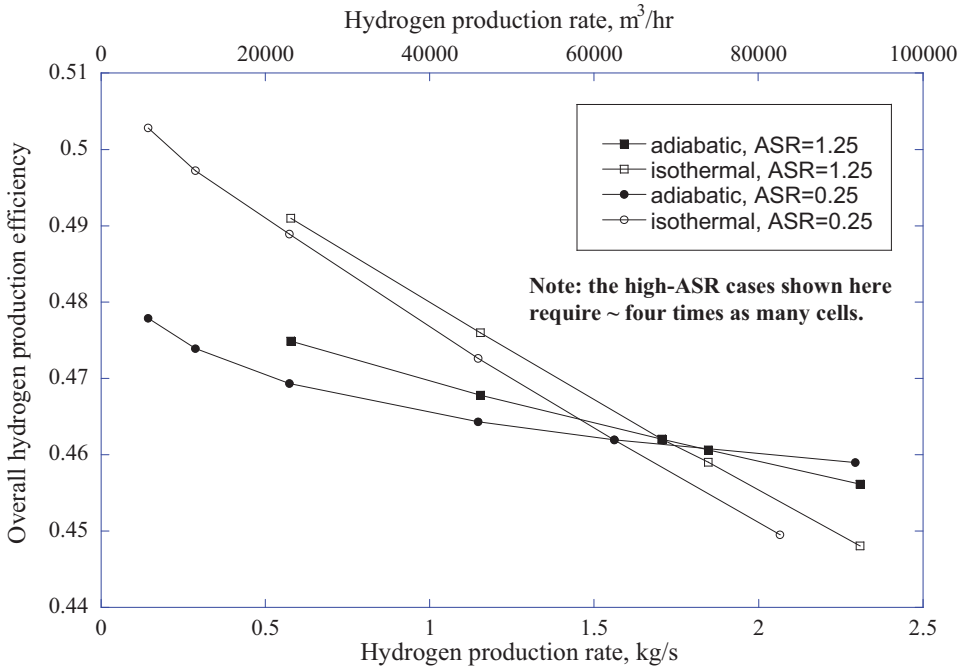

Figure 32. Overall hydrogen production efficiency as a function of hydrogen production rate, with air sweep.

include consideration of a sweep gas. Overall hydrogen efficiency results of the air-sweep cases are about 1% lower than the no-sweep cases.

Hydrogen production efficiencies can also be plotted as a function of hydrogen production rate, as shown in Fig. 32. As expected, efficiencies decrease with production rate since higher production rates require higher current densities and higher per-cell operating voltages, for a

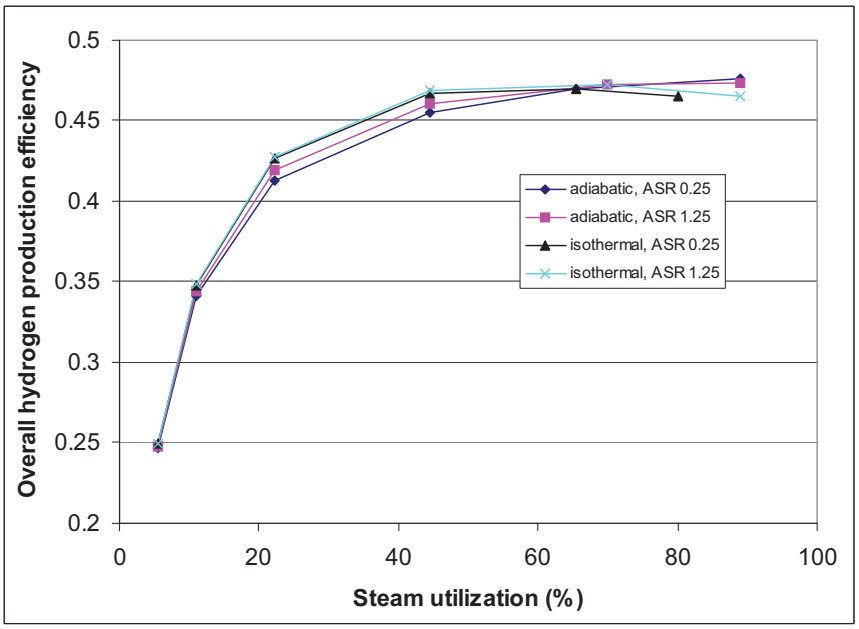

Figure 33. Effect of steam utilization on overall hydrogen production efficiency.

fixed number of cells. For this plot, the full 600 MW_{th} output of the reactor is assumed to be dedicated to hydrogen production. Under this assumption about four times as many electrolysis cells are required for the high-ASR cases than for the low-ASR cases, with a correspondingly higher associated capital cost. Fig. 32 shows that hydrogen production rates in excess of 2.3 kg/s (92,000 SCMH, 78×10^6 SCF/day) could be achieved with a dedicated 600 MW_{th} hydrogen-production plant. This rate is the same order of magnitude as a large hydrogen production plant based on steam-methane reforming. Fig. 32 indicates similar overall efficiencies for the low-*ASR* and high-*ASR* cases at a specified electrolyzer thermal operating condition (adiabatic or isothermal) and hydrogen production rate.

The effect of steam utilization was examined by fixing the electrolyzer inlet process gas flow rates at the values corresponding to the highest current density achievable with each ASR value, then varying the current density over the full range of values considered for the fixed-utilization cases. Low current densities for this case yield low values of steam utilization since the inlet steam flow rate is fixed at a value that yields 89% utilization at the highest current density. Results of this exercise are presented in Fig. 33. The overall efficiency results for the variable-utilization cases nearly collapse onto a single curve when plotted versus utilization. The plot indicates a strong dependence on utilization, with overall hydrogen production efficiencies less than 25% at the lowest utilization values shown (~5.5%), increasing to a maximum value of ~47% at the highest utilization value considered (89%). So, from the overall system perspective, low steam utilization is bad. This is an interesting result because, from the perspective of the electrolyzer alone, low utilization yields high electrolyzer (not overall) efficiency values. Excess steam in the electrolyzer keeps the average Nernst potential low for each cell, which assures a low operating voltage for a specified current density (or hydrogen production rate). However, from the overall system perspective, low steam utilization means that the system is processing

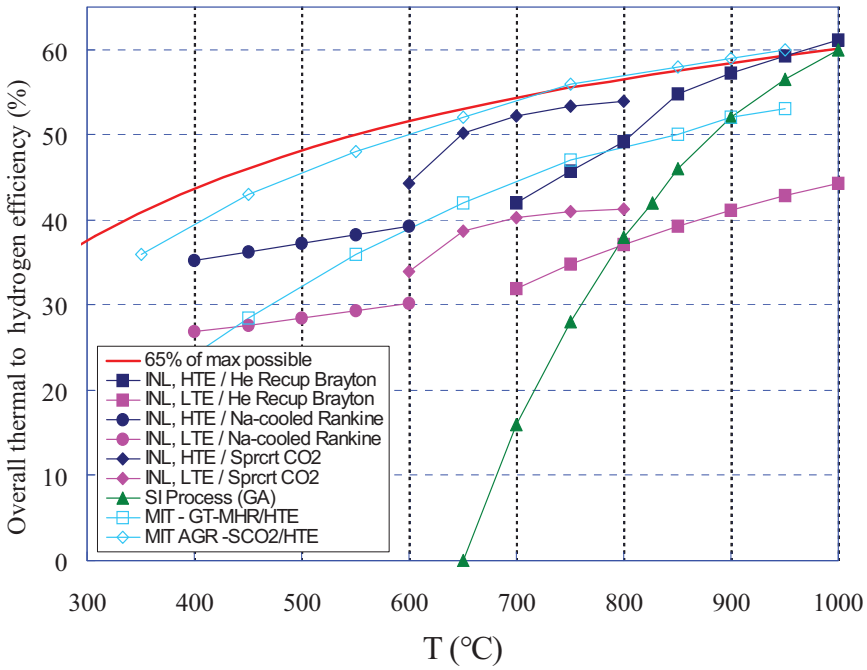

Figure 34. Overall thermal-to-hydrogen efficiencies (based on HHV) for HTE coupled to three different reactor types, as a function of reactor outlet temperature.

lots of excess material, resulting in relatively high irreversibilities associated with incomplete heat recuperation, pumping and compression of excess process streams, etc. Above ~50% utilization, however, the efficiency curves are relatively flat, even decreasing slightly for the isothermal cases. Regarding very high utilization values, achievement of steam utilization values much above 90% is not practical from an operational standpoint because localized steam starvation can occur on the cells, with associated severe performance penalties and possible accelerated cell lifetime degradation.

The effect of reactor outlet temperature has also been considered. Fig. 34 shows overall hydrogen production efficiencies, based on high heating value in this case, plotted as a function of reactor outlet temperature. This figure was also presented in the Fundamentals section of this report. The figure includes a curve that represents 65% of the thermodynamic maximum possible efficiency (i.e., 65% exergetic efficiency) for any thermal water splitting process, assuming heat addition occurs at the reactor outlet temperature and heat rejection occurs at $T_L = 20°C$ [3]. In order to cover a broad range of possible reactor outlet temperatures, three different advanced-reactor/power-conversion combinations were considered: a helium-cooled reactor coupled to a direct recuperative Brayton cycle, a supercritical CO_2-cooled reactor coupled to a direct recompression cycle, and a sodium-cooled fast reactor coupled to a Rankine cycle. Each reactor/power-conversion combination was analyzed over an appropriate reactor outlet temperature range.

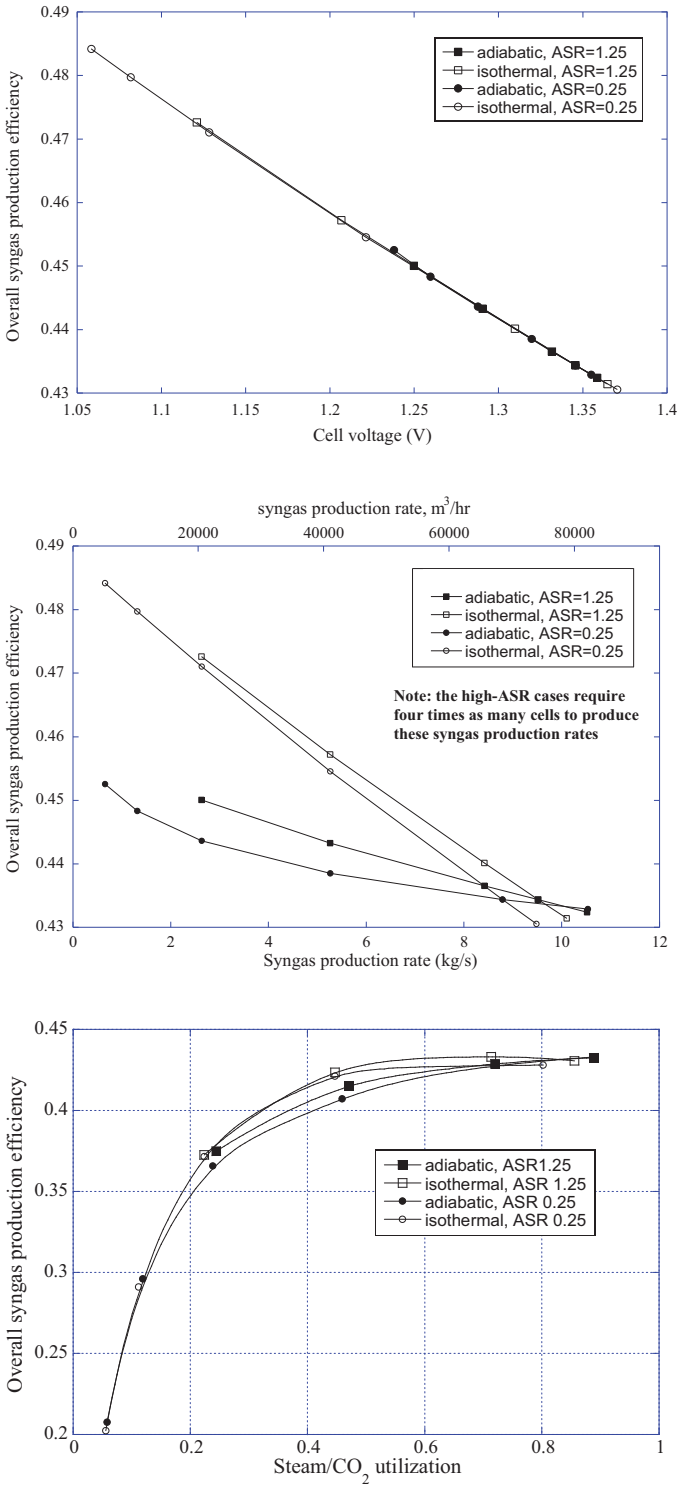

Figure 35. Overall syngas production efficiencies, air-sweep cases; (a) fixed utilization, function of per-cell operating voltage; (b) fixed utilization, function of syngas production rate; (c) variable utilization, function of utilization.

The figure shows results for both HTE and low-temperature electrolysis (LTE). Results of system analyses performed at MIT [1] are also shown. The lower MIT curve, labeled MIT-GT-MHR/HTE represents overall efficiency predictions for a helium-cooled reactor with a direct Brayton cycle power conversion unit. The upper MIT curve, labeled MIT-AGR-SCO2/HTE represents overall efficiency predictions for a CO2-cooled advanced gas reactor with a supercritical CO2 power conversion unit. Finally, an efficiency curve for the SI thermochemical process [18] is also shown. The results presented in Fig. 34 indicate that, even when detailed process models are considered, with realistic component efficiencies, heat exchanger performance, and operating conditions, overall hydrogen production efficiencies in excess of 50% (HHV) can be achieved for HTE with reactor outlet temperatures above 850°C. For reactor outlet temperatures in the range of 600 - 800°C, the supercritical CO_2/recompression power cycle is superior to the He-cooled/Brayton cycle concept. This conclusion is consistent with results presented in [1]. The efficiency curve for the SI process also includes values above 50% for reactor outlet temperatures above 900°C, but it drops off quickly with decreasing temperature, and falls below values for LTE coupled to high-temperature reactors for outlet temperatures below 800°C. Note that even LTE benefits from higher reactor outlet temperatures because of the improved power conversion thermal efficiencies. Current planning for NGNP [14] indicates that reactor outlet temperatures will be at or below 850°C, which favors HTE.

4.2.2. Direct Electrolytic Syngas Production.

System analysis results for direct syngas production from co-electrolysis of steam and CO_2 are qualitatively similar to the straight steam electrolysis results. Representative results are presented in Fig. 35. Once again, overall process efficiencies for fixed utilization collapse onto a single line when plotted as a function of per-cell operating voltage, as shown in Fig. 35(a). Note that the highest operating voltages shown are just above the co-electrolysis thermal neutral voltage of 1.34 V. Note also that the highest overall efficiency plotted in Fig. 35(a) (for ASR = 0.25, isothermal, i = 0.0625 A/cm^2) is actually slightly higher than the power cycle efficiency of 48.3%. Overall syngas production efficiencies are plotted as a function of syngas production rate in Fig. 35(b). This figure shows that syngas production rates in excess of 10 kg/s (78,000 SCMH) could be achieved with a dedicated 600 MW_{th} syngas-production plant. Fig. 35(b) also indicates similar overall efficiencies for the low-*ASR* and high-*ASR* cases at a specified electrolyzer thermal operating condition (adiabatic or isothermal) and syngas production rate. Recall, however, that the high-*ASR* plant requires four times as many cells as the low-*ASR* plant for the same syngas production rate and operating voltage. So the capital cost of the electrolytic plant would be significantly greater with the high-*ASR* cells compared to the low-*ASR* cells. Syngas production efficiencies are plotted as a function of steam/CO_2 utilization in Fig. 35(c). The overall efficiency results for the variable-utilization case nearly collapse onto a single curve when plotted versus utilization. The plot indicates a strong dependence on utilization, with overall efficiencies of only 20% at the lowest utilization values shown (~5.7%), increasing to a maximum value of 43% at the highest utilization value considered (90%). Again, low utilization results in relatively high irreversibilities associated with incomplete heat recuperation, pumping and compression of excess process streams, etc.

4.2.3. Syngas Production from Coal and Biomass

One possible strategy for reducing dependence on imported oil is to utilize alternate carbon sources like coal or biomass for the production of synthetic liquid fuels such as diesel. The first step in the production of synthetic liquid fuels is syngas production. However, the traditional processes for producing syngas from these carbon sources also produce significant quantities of carbon dioxide that must be sequestered or released to the atmosphere. For example, with traditional coal-to-liquids (CTL) technology, only about one-third of the carbon in the coal feedstock ends up in the liquid fuel product [32]. If supplemental hydrogen is available, nearly all of the carbon in the coal can end up in the liquid fuel product. Supplemental hydrogen for this process should be obtained from an efficient non-carbon-emitting process such as high-temperature electrolysis (HTE) of steam powered by nuclear energy [24]. Coupling of the HTE process to CTL is particularly appealing because it is more efficient than conventional electrolysis and because it provides both hydrogen and oxygen at elevated temperature. The oxygen can be fed directly to a gasifier and the hydrogen can be used to reduce the excess carbon dioxide produced in the gasifier, via the reverse shift reaction. A system analysis of the nuclear/HTE-assisted CTL process has been recently completed at INL [33]. A representative result from this study is shown in Fig. 36 which shows the dependence of syngas production efficiency and carbon utilization on coal moisture content. Carbon utilization increases with decreased moisture content, reaching a value of 98.8% for a moisture content of 16.1%. The syngas production efficiency shown in Fig. 36 also appears to increase as the moisture content is reduced, but peaks at about 68.8% at a coal moisture content of 25%. The slight drop in syngas production efficiency as the coal moisture content is reduced below 25% is the result of the need to increase the gasifier temperature to maintain a minimum heat exchanger approach temperature for the steam generator of approximately 20°C. This drop in syngas production efficiency is consistent with results that show a drop in syngas production efficiency as the gasifier temperature increased. Note that the syngas production efficiencies for this process are considerably higher than those associated with the purely electrolytic co-electrolysis process. A similar study has been performed for nuclear-assisted biomass-to-syngas [34]. This study predicted biomass-to syngas efficiencies greater than 70%, with carbon utilization near 95%.

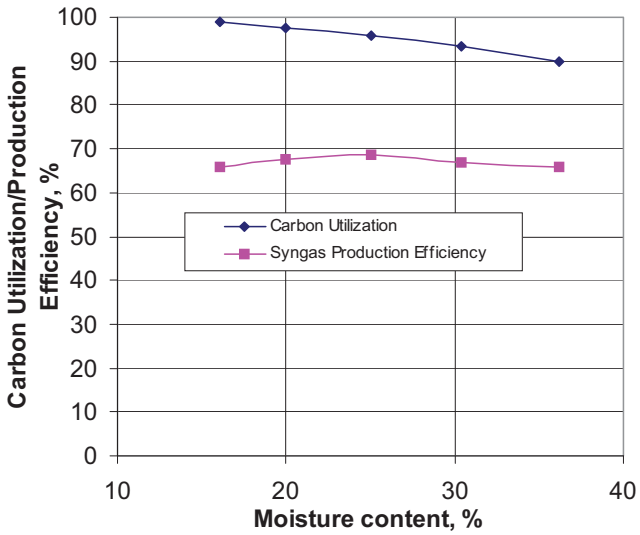

Figure 36. Carbon utilization and syngas production efficiency as a function of coal moisture content.

4.3. Economic Analysis – HTE Hydrogen Production

A preliminary economic analysis has been performed to estimate the cost of hydrogen based on high-temperature electrolysis coupled to an advanced high-temperature gas-cooled reactor [35]. The reference HTE plant is driven by a 600 MW_t high-temperature helium-cooled reactor coupled to a direct Brayton power cycle with a reactor outlet temperature of

900°C. Plant parameters used in the reference plant optimization were based on parametric studies performed using the UniSim process analysis software. For the economic analysis of HTE-produced hydrogen, isothermal operation of the electrolyzer was assumed. An air sweep system is also included in the reference design to remove oxygen from the anode side of the electrolyzer because of concerns with handling of the high-temperature oxygen product gas. Predicted overall thermal-to-hydrogen efficiency values for the reference design with an air-sweep system resulted in hydrogen production efficiencies that were only 1.0–1.5% lower than that for the equivalent design with no sweep-gas system [2]. The operating pressure of 5.0 MPa for the HTE process loop was selected to be consistent with the need to deliver the hydrogen product gas at elevated pressures for storage or pipeline transport. This pressure also represents a trade off between the need for larger components at lower pressures and the need for more massive components for pressure containment at higher pressures. The overall thermal-to-hydrogen efficiency for the reference case is 47.1%.

The economic analysis was performed using the standardized H2A Analysis Methodology developed by the Department of Energy (DOE) Hydrogen Program, using realistic financial and cost estimating assumptions. Based on this methodology, and the various assumptions discussed in detail in reference [35], the estimated price of the hydrogen leaving the plant gate at 5 MPa pressure would be $3.23/kg. Several sensitivity analyses were performed to evaluate the impact of various economic assumptions on hydrogen lifecycle production costs. The assumed after-tax internal rate of return was found to have a significant impact on the cost of hydrogen production. A variation of the internal rate of return from 0 to 25% results in hydrogen production cost variations between $1.64/kg of H_2 and $7.40/kg of H_2, respectively. Figure 37 is a tornado plot that shows the sensitivity of hydrogen production costs to the various economic and operational assumptions used in the H2A economic analysis of the reference HTE plant. The tornado plot shows the impact on hydrogen production cost when a single variable is changed while holding other variables constant at their base case values. In the tornado plot, the parameters that have the largest impact on production costs are shown at the top, and the parameters that have the least impact on hydrogen production costs are shown at the bottom. Therefore, the importance of parameters on hydrogen production costs decreases as the plot is read from top to bottom. As indicated in the plot, the after-tax internal rate of return has the greatest impact on hydrogen production costs. Unplanned replacement costs are next in importance. In this analysis, unplanned replacement costs were assumed to be 2% of the total direct depreciation costs per year. When the unplanned replacement costs are varied from 0 to 10%, the resulting hydrogen production costs vary between $2.94/kg and $4.39/kg, respectively. The third most important parameter in the cost analyses is the assumed cost of the SOE modules. In this analysis, the cost of the SOE modules was assumed to be $200 per kW of electricity to the electrolysis stack. If this cost is varied between $100 and $300/kW, the corresponding cost of hydrogen varies from $2.83 to $3.63/kg, respectively. Variations in the size of the plant staff, the cost of major reactor system components and the frequency at which the SOE cells are replaced, all appear to have moderate affects on the cost of hydrogen production. Variations in engineering design costs seem to have only a small impact on hydrogen production cost. Because the cost of the hydrogen plant equipment (turbomachinery, heat exchangers, piping, etc.) is low compared to the cost of the nuclear plant equipment and the SOE modules, the impact of variations in major hydrogen plant equipment costs has the least impact on hydrogen production costs of the parameters considered.

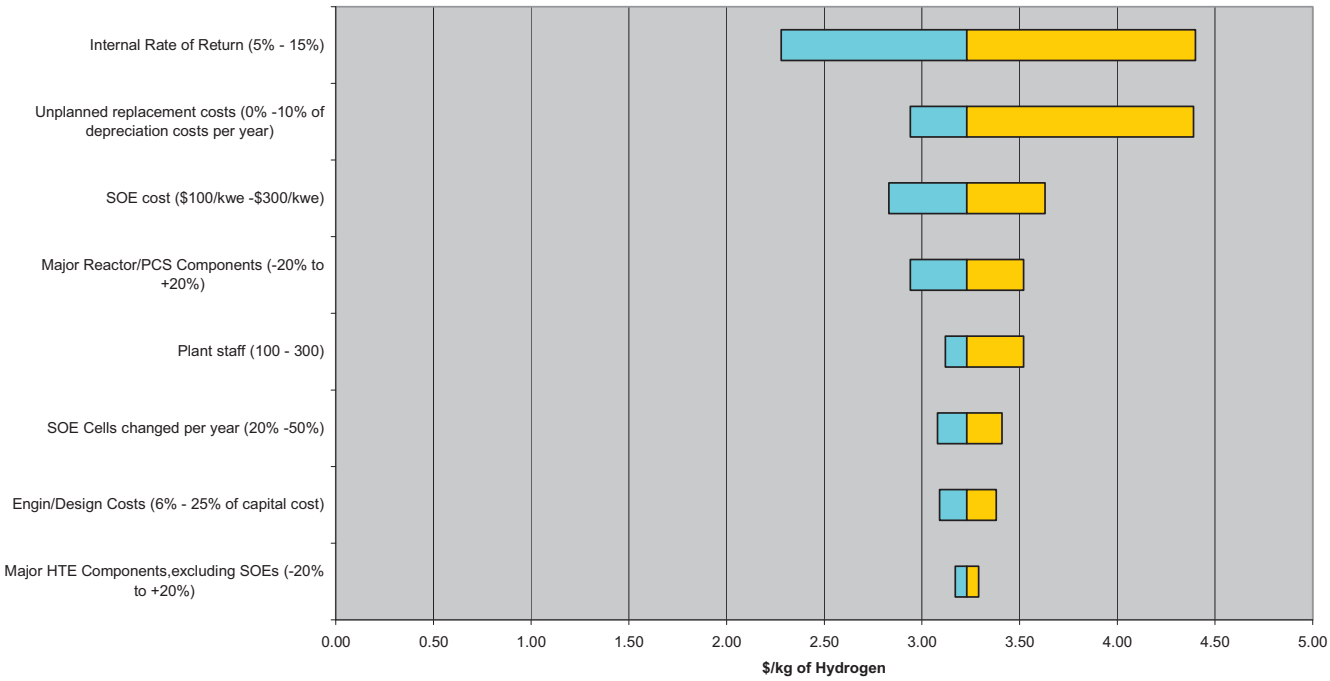

Figure 37. Tornado plot showing sensitivity of hydrogen cost to parameter variations.

Compared to the current hydrogen commodity price of about $2.50/kg (based on steam-methane reforming), the mean estimated cost is not unreasonable considering the volatility of the cost of the natural gas and the fact that the HTE technology does not emit greenhouse gases. Estimates of hydrogen production cost based on LTE depend strongly on electricity prices, but for large systems (1000 kg/day), with an assumed industrial electricity cost of $0.0483/kWh, a hydrogen selling price of $4.15 (FY2000 dollars) has been reported [36], based on the DOE H2A methodology. The lesson here is that any proposed new technology for large-scale hydrogen production must be able to compete with this price.

As noted above, the lifecycle cost analysis of the reference HTE design resulted in a calculated hydrogen cost of $3.23/kg, assuming an after-tax internal rate of return of 10%. This represents the cost of hydrogen leaving the plant gate, and does not include any additional storage, delivery, fuel taxes or other costs that the consumer might pay at the pump. A breakdown of the component costs contributing to the total cost of $3.23/kg shows that capital costs account for over 70% of total costs (i.e., $2.36/kg of H_2). This is expected because of the high construction costs for the nuclear reactor. Fixed operating and maintenance costs ($0.57/kg of H_2) are relatively high because they include operation and maintenance costs for both the reactor and hydrogen production plant. Yearly variable costs ($0.28/kg of H_2) include the reactor fuel cost, a reserve for unplanned equipment replacement costs, and the yearly replacement cost of the solid oxide electrolysis cells. The cost of the SOEC modules was estimated to be $200/kW of power to the electrolysis stack and it is assumed that 1/3 of the modules are replaced annually. The feedstock cost contribution ($0.012/kg of H_2) represents the cost of the demineralized water feedstock, which feeds the electrolysis process. Although the electrolysis process also produces oxygen, which could be sold as a byproduct of the hydrogen production process, the reference HTE design does not attempt to recover the oxygen byproduct. Therefore, while the sale of the oxygen byproduct would lower the overall cost of the hydrogen

production process, no credit for the production of oxygen was taken in this cost analysis.

5. COMPUTATIONAL FLUID DYNAMICS ANALYSIS

The INL HTE research program also includes modeling and materials development tasks. For detailed SOEC modeling, the commercial CFD code FLUENT was selected. Fluent Inc. was funded by the US Department of Energy National Energy Technology Laboratory (DOE-NETL) to develop a solid-oxide fuel cell (SOFC) module for coupling to the core mass, momentum, energy, and species conservation and transport features of the FLUENT CFD code [37]. The SOFC module adds the electrochemical reactions and loss mechanisms and computation of the electric field throughout the cell. The FLUENT SOFC user-defined subroutine was modified for this work to allow for operation in the SOEC mode. Model results provide detailed profiles of temperature, Nernst potential, operating potential, anode-side gas composition, cathode-side gas composition, current density and hydrogen production over a range of stack operating conditions. Results of the numerical model have been compared to experimental results obtained from a ten-cell stack tested at INL.

5.1. Numerical Model

Predictions obtained from the 1-D integral model described earlier in this report have also been compared to results obtained from a full 3-D FLUENT simulation. Complete details of the FLUENT electrolysis stack model are provided in [38]. A condensed description is presented here. The numerical model developed for this paper was based on the geometry of a single solid-oxide electrolysis cell (SOEC) taken from a planar stack described in detail in [39, 40]. The numerical domain extends from the center plane of one separator plate to the center plane of the next separator plate. Symmetry boundaries are applied at the top and bottom of the model. Three representations of the numerical model are presented in Fig. 38. In the top left portion of this figure, the full model is shown to scale. Since the model includes only one cell, the model geometry is quite thin in the vertical (z) direction. To show more detail, the model is shown in the bottom left portion of Fig. 38 with a vertical exaggeration of 10× in the z-direction. An exploded view with the 10× vertical exaggeration is shown in the right half of the figure.

In the exploded view, the bottom element is the bottom separator plate. Since we are trying to represent a unit cell extracted from a larger stack, the bottom and top separator plates in the numerical model are only half as thick (i.e., 0.19 mm) as the hardware separator plates. Therefore, the top and bottom boundaries of the numerical model represent symmetry planes and the boundary conditions on those faces are set accordingly. The edge rails are shown attached to the bottom separator plate. In the stack hardware, the edge rails are fabricated from the same material as the separator plates, but they are separate pieces.

The next element in the numerical model is the steam/hydrogen flow channel. The flow channels are the regions in the stack between the separator plate, the edge rails and the electrodes in which the corrugated/perforated “flow fields” are located. In the FLUENT model, the steam/hydrogen flow channel has been specified as a high-porosity porous-media region with metallic nickel as the solid material and with anisotropic permeability, much higher in the primary flow direction than in the cross flow directions. The height of the flow channel is set by the thickness of the edge rails, 1.019 mm.

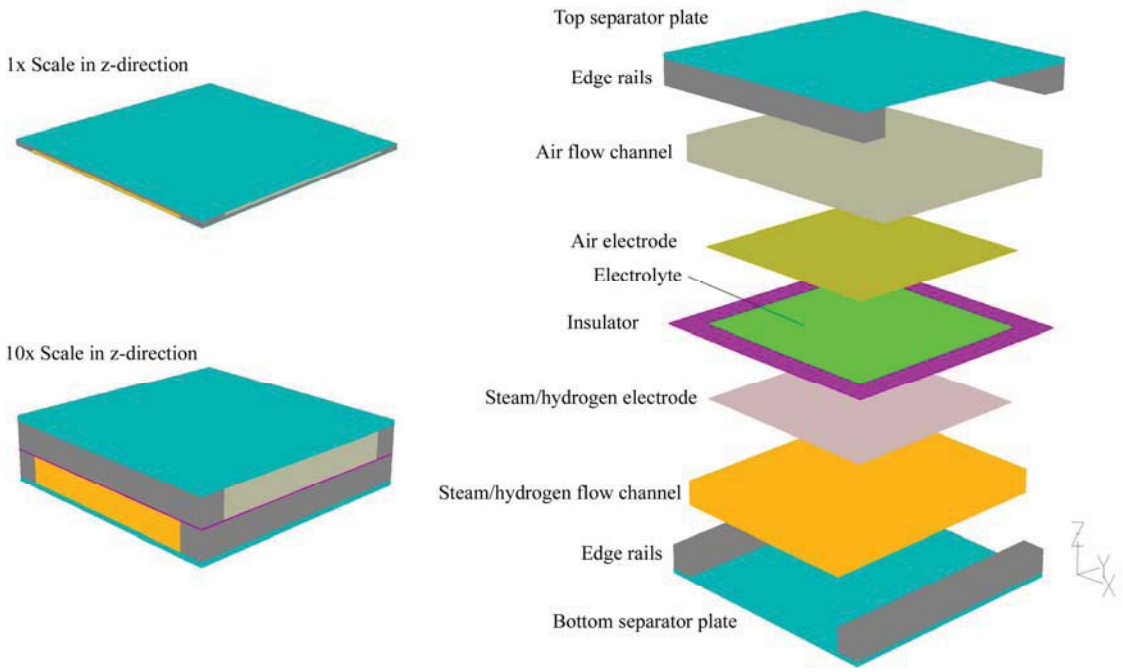

Figure 38. Fluent single-cell SOEC model.

The next three layers in the numerical model are associated with the electrolyte/electrode assembly, as shown in the right half of Fig. 38. The FLUENT solid-oxide fuel cell (SOFC) module treats the electrolyte as a 2-D planar element with the properties of yttria-stabilized zirconia (YSZ). Therefore the electrolyte in the model has geometrical thickness of zero. On either side of the electrolyte are the electrodes which are created with 3-D elements. Therefore, the electrolyte/electrode assembly in the model is only as thick as the two electrodes. Around the outer periphery of the electrolyte/electrode assembly, we have included an "insulator" with the properties of YSZ. The insulator prevents an electrical short circuit between the top and bottom edge rails. No ionic transport occurs through this insulator.

The next element in the numerical model is the air/oxygen flow channel. It has also been specified as a high-porosity porous media region with ferritic stainless steel as the solid material and with the same anisotropic permeabilities and flow channel height used in the steam/hydrogen flow channel. The top separator plate and edge rails are identical to those on the bottom, but the edge rails are oriented perpendicular to the bottom edge rails to allow for the cross-flow arrangement. The bottom separator plate in the FLUENT model serves as the electrical ground and the top separator plate serves as the current source.

Additional parameters specified in the numerical model include the electrode exchange current densities and several gap electrical contact resistances. These quantities were determined empirically by comparing FLUENT predictions with stack performance data. The FLUENT model uses the electrode exchange current densities to quantify the magnitude of the activation overpotentials via a Butler-Volmer equation [37].

The gas flow inlets are specified in the FLUENT model as mass-flow inlets, with the gas inlet temperatures are set at 1103 K and the inlet gas composition determined by specification of the mass fraction of each component. The gas flow rates used in the model were the same as

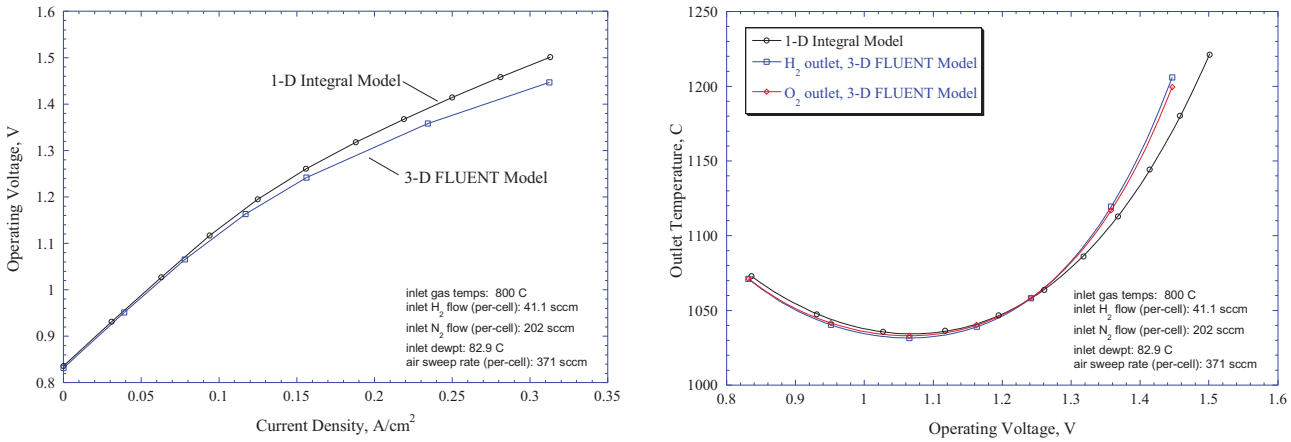

Figure 39. Predicted operating voltage and gas outlet temperatures for adiabatic electrolyzer operation; comparison of 1-D integral MathCad model with full 3-D FLUENT simulation.

those used for the experimental base case, on a per-cell basis. For example, the base case for the steam/hydrogen inlet used a total inlet mass flow rate of 8.053×10^{-6} kg/s, with nitrogen, hydrogen and steam mass fractions of 0.51, 0.0074, and 0.483, respectively. The base case air flow rate was 4.33×10^{-6} kg/s.

Details of the core mass, momentum, energy, and species conservation and transport features of FLUENT are documented in detail in the FLUENT user manual (FLUENT, 2004). An SOFC model adds the electrochemical reactions, loss mechanisms, electric field computation, and electrode porous media constitutive relations [37]. This reference also documents the treatment of species and energy sources and sinks arising from the electrochemistry at the electrode-electrolyte interfaces. The FLUENT SOFC user-defined subroutine was modified for our HTE work to allow for operation in the SOEC mode. Model results provide detailed profiles of temperature, Nernst potential, operating potential, anode-side gas composition, cathode-side gas composition, current density and hydrogen production over a range of stack operating conditions.

5.2. Representative CFD Results

Representative results obtained from the integral electrolyzer model for an adiabatic case are presented in Fig. 39, along with results obtained from FLUENT. Fig. 39 shows predicted voltage-current characteristics and predicted gas outlet temperatures. The 1-D integral model predicts somewhat higher operating voltages compared to the FLUENT results. This makes the 1-D model conservative since higher operating voltages correspond to lower electrolysis efficiencies. The disparity can be explained by noting that the CFD model can more accurately account for the variation in local Nernst potential and local current density associated with the cross-flow geometry of the planar stack. Note that, for an operating voltage near the thermal minimum (~1.06 V), both models predict outlet temperatures for this particular adiabatic case that are about 30ºC lower than the inlet temperatures. This temperature depression is due to the fact that the endothermic heat requirement of the steam dissociation reaction is larger than the ohmic heating in the operating voltage range between open-cell potential and the thermal-neutral voltage. Per-cell gas flow rates for this case were based on the flow rates used in planar HTE stack tests [39, 40]. The 1-D model also predicts the correct value of the thermal neutral voltage for 800ºC, 1.287 V. At this operating voltage, the outlet temperatures are equal to the inlet temperatures under adiabatic conditions. The 1-D model is also useful for assessing the effect of

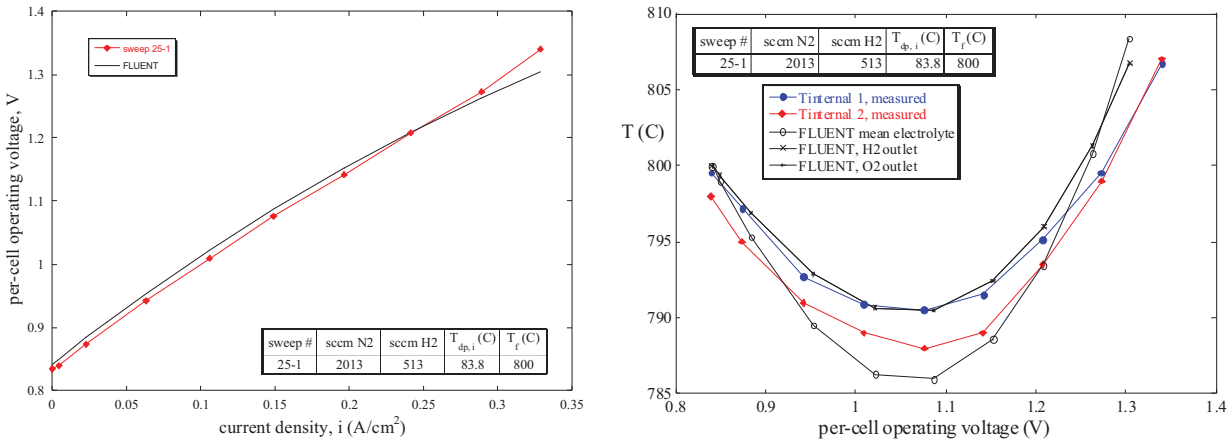

Figure 40. Comparison of internal stack temperature predictions with experimentally measured values.

using a steam sweep rather than an air sweep on the oxygen side. Use of a sweep gas that does not contain oxygen is advantageous because it reduces the Nernst potential, thereby increasing the electrolysis efficiency for a specified current density. We are considering the use of steam for the sweep gas since it would be relatively easy to separate the steam from the produced oxygen by condensation. The produced oxygen then could be sold as a commodity. Incorporation of the 1-D model into our HYSYS system simulation will enable a broad range of parametric studies.

Results obtained from FLUENT were also compared to experimental results. Only one set of representative results are shown here in Fig. 40. The results shown correspond to sweep 25-1 of Fig. 19(b). This sweep was performed in a stepwise fashion in order to allow sufficient time at each operating condition for steady-state thermal conditions to be achieved in the stack. The figure shows experimentally measured voltage-current characteristics and internal stack temperatures obtained during a DC potential sweep, along with FLUENT predictions. The FLUENT model included empirical values for internal stack contact resistances, scaled to match the measured voltage-current values of sweep 25-1 of Fig. 19(b). This scaling is necessary because it is not possible to predict these contact resistance values from first principles. Corresponding predicted and measured internal stack temperatures are shown in Fig. 40(b). The experimental internal stack temperatures were obtained from miniature (inconel-sheathed, 0.020-inch (500 μm) OD, mineral-insulated, ungrounded, type-K) thermocouples that were inserted into selected air-flow channels. The comparison between the experimentally obtained stack internal temperatures and the FLUENT mean electrolyte temperature is quite good, and serve to validate the numerical methods and models used.

Detailed CFD analyses also provide a means of visualizing temperature and current density distributions with operating cells and stacks. A series of contour plots representing local FLUENT results for temperature, current density, Nernst potential and hydrogen mole fraction is presented in Figs. 41-44. In these figures, the steam/hydrogen flow is from top to bottom and the air flow is from left to right. Figure 41 shows electrolyte temperature contour plots for amperages of 10, 15, and 30 amps. These current values correspond to operating voltage regions near the minimum electrolyte temperature (10 amps), near thermal neutral voltage (15 amps), and in the region dominated by ohmic heating (30 amps). The radiant boundary condition at 1103 K tends to hold the outside of the model at a higher temperature for the 10-amp case (Fig.

41 (a))while the endothermic heat requirement maintains the center of the electrolyte at a lower temperature. Minimum and maximum temperatures for this case are 1091 K and 1100 K respectively. The center Fig. 41 (b) shows a temperature difference across the electrolyte of only one degree K, with values very near 1103 K; this current density is very near the thermal neutral voltage. Fig. 41 (c) shows that ohmic heating in the electrolyte is dominating and the thermal boundary condition is keeping the edges cooler than the inside. Minimum and maximum temperatures are 1139 K and 1197 K, respectively, for this case.

Contour plots of local current density on the electrolyte are shown in Figure 42 for 10, 15, and 30 amps. Mean current densities for these three cases are: 0.156, 0.234, and 0.469 A/cm^2. These plots correlate directly with local hydrogen production rates. Since FLUENT is being run in electrolysis mode, the current density values are all negative and hence the blue values have the largest magnitudes. Highest current density magnitudes occur near the steam hydrogen inlet (the top of the figures). This corresponds to the location of the greatest steam concentration. The orange areas show where the current density is lowest because the available steam concentration is lower.

Figure 43 shows the local variation in Nernst potential for currents of 10, 15, and 30 amps. The minimum Nernst voltage occurs at the top left of the plots where the steam and oxygen concentrations are the highest and hydrogen concentration the lowest. The minimum value for the Nernst voltage in these three plots is 0.84 V, while the maximum increases from 0.91 V to 0.93 V to 0.99 V as the current increases from 10 to 30 amps respectively. Maximum Nernst voltage occurs in the bottom right where the steam concentration is the lowest. The highest Nernst potential regions correspond to the lowest current density regions. Note that the variation in Nernst potential indicated in these plots is dominated by gas concentration effects, rather than thermal effects.

Molar hydrogen fraction contours are shown in Figure 44 for currents of 10, 15, and 30 amps. These contours show the entire steam/hydrogen flow channel, including the top and bottom regions adjacent to the edge rails where no hydrogen production is occurring. Hydrogen concentration increases as the flow progresses through the channel from top to bottom. There is a slight bump of higher concentration at the left side of the flow channel for the first two plots and in the center for the third plot. This corresponds to the local variation in current densities. The hydrogen concentrations at the outlet are 0.21, 0.28, and 0.48 for the three cases.

6. KEY TECHNICAL CHALLENGES FOR HIGH TEMPERATURE ELECTROLYSIS

Hydrogen production by means of high temperature electrolysis using solid oxide cells is not yet a commercial-ready technology. The state of the art of solid oxide fuel cells has advanced significantly in recent years, thanks in part to financial support from the DOE SECA program. The development of advanced anode-supported cells represents a major milestone for SOFCs. Solid oxide electrolysis cell technology has also benefitted from advancement of SOFCs, but relatively little direct funding has been available for SOEC research. There are some fundamental differences in the two modes of operation, such that different cell materials, cell designs, and stack configurations will be required for optimal long-term performance in the electrolysis mode. Some of these issues were discussed in the section of this report on cell materials.

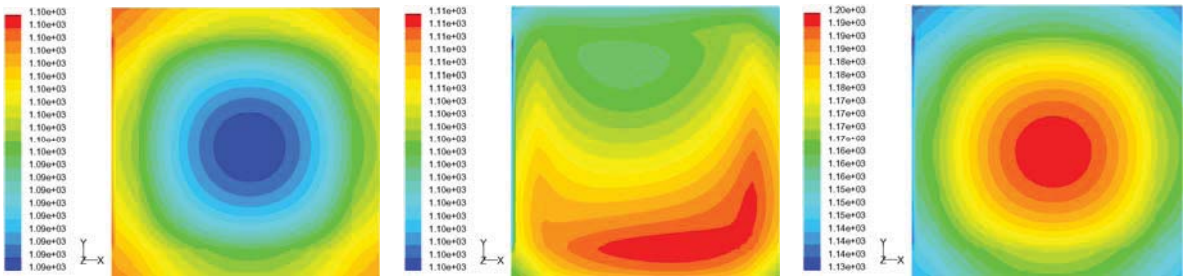

(a) (b) (c)

Figure 41. Temperature (K) contours on the electrolyte and insulator for currents of 10, 15, and 30 amps.

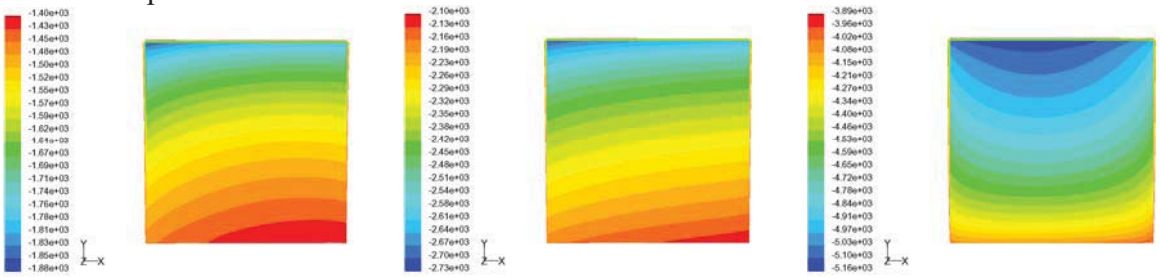

(a) (b) (c)

Figure 42. Current density (A/m^2) contours on the electrolyte for currents of 10, 15, and 30 amps.

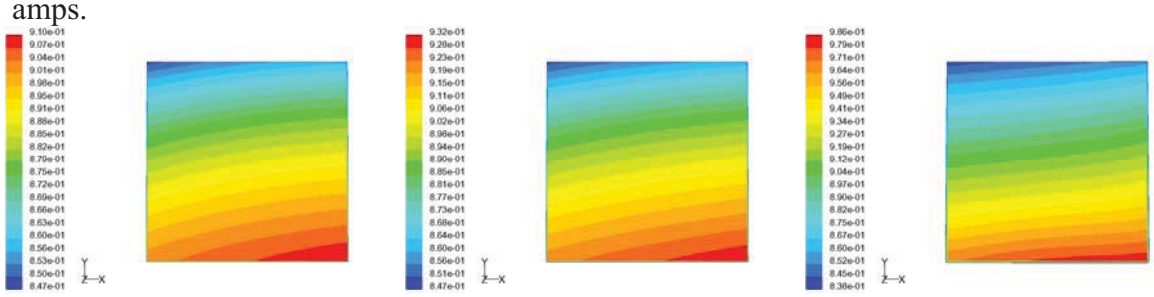

(a) (b) (c)

Figure 43. Nernst potential (V) contours on the electrolyte for currents of 10, 15, and 30 amps.

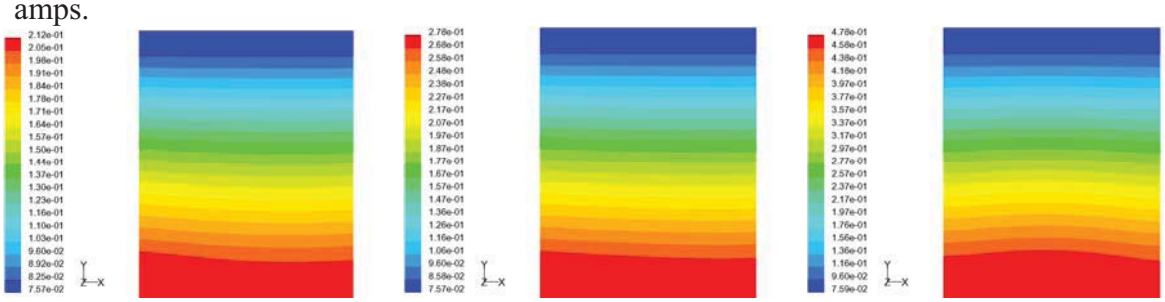

(a) (b) (c)

Figure 44. Contours of hydrogen mole fraction in hydrogen flow channel for currents of 10, 15, and 30 amps.

The ultimate cost of hydrogen production by any technology is dependent on both capital and operating costs. In order to achieve competitive capital costs, HTE cells and stacks must exhibit both high performance and low degradation rates. High performance can be quantified in terms of the area-specific resistance (ASR). Per-cell ASR values of 0.40 Ohm·cm^2 or lower in a stack configuration, with very low degradation rates of less than 1% per 1000 hours will be required

for large-scale hydrogen production. These performance values have already been demonstrated by several SOFC manufacturers in the fuel-cell mode of operation. Cell ASR values lower than 0.4 Ohm·cm^2 have been observed at INL in single-cell tests, but not yet in a stack configuration. The stack testing performed at INL to date has also exhibited large degradation rates. Several mechanisms have been proposed as contributors to the accelerated degradation observed in the electrolysis mode. INL sponsored a workshop on SOEC performance degradation in October of 2008. INL will also be participating in an invitation-only international workshop in June, 2009 on this topic. Our research focus during FY09 is in fact on SOEC degradation. We are working with Ceramatec, Inc. and MSRI, both in Salt Lake City, toward development of improved electrolysis cells and stacks. We are also supporting research activities at MIT and the U. of Utah on understanding degradation mechanisms. A comprehensive summary of the state of knowledge of SOEC degradation and a summary of the topics presented at the INL SOEC degradation workshop is available in reference [41]. A portion of this report is provided in the next section.

6.1. Degradation in SOECs

At present, a complete understanding and reasonable agreement on the causes of degradation and electrochemical mechanisms behind them does not exist. Therefore, the following write-up only represents the collective opinion of workshop attendees. It is not inclusive of all the available literature and all the phenomena relevant to degradation by any means.

Experimental data on degradation can be classified into three main categories: (a) baseline progressive constant-rate degradation, (b) degradation corresponding to transients caused by thermal or redox (**red**uction and **ox**idation) cycling phenomena occurring in a cell, and (c) degradation resulting from a sudden incident or a failure/malfunction of a component or a control in a stack system. However, there is no clear evidence if different events lead to similar or drastically different electrochemical degradation mechanisms within a cell.

6.1.1. SOEC versus SOFC Stacks

Degradation data have been obtained both in single cells as well as in stacks. Degradation mechanisms in a stack are not identical to those in a single cell [42]. Also, degradation in a SOEC is not identical to that in a SOFC. Long-term single cell tests show that SOEC operation exhibits greater degradation rates than SOFC operation. Therefore, SOFC degradation can be used for background information and guidance. But for specific SOEC stack development, all studies have to be done on SOEC stacks. Some researchers observed that higher operating temperatures increase degradation in SOEC, but higher current density does not increase degradation. However, ANL observed higher degradation in higher current flow regions of O_2-electrodes. Such unconfirmed and conflicting opinions need to be resolved during future research.

6.1.2. Air/Oxygen Electrode

It is understood that degradation of the O_2-electrode is more severe than that of the H_2-electrode. Therefore, it was proposed to focus initially on the degradation of the O_2-electrodes in a stack. Argonne National Laboratory's (ANL) examination of an SOEC stack operated by INL for ~1500 hr showed that the O_2-electrode delaminated from the bond layer/electrolyte. However, the causes of the delamination can be termed as speculative, because confirmative tests proving the fundamental cause(s) have not been performed. It is thought that high oxygen

evolution in over-sintered region can build up high pressure at those locations. In SOEC mode, O_2 has to be pushed out, hence chances of delamination increase. Therefore, high porosity of O_2-electrode is very important. This opinion was expressed by many participants and hence deserves further examination. Per ANL observations, the delamination occurs in cell areas with high current flows. It was also suggested that chromium poisoning originating from the interconnects or from balance-of-plant piping may get located at the interface or triple phase boundary (TPB). This can result in separation of the bond layer from the O_2-electrode. Deposition of impurities at the TPB and delamination can adversely impact the electrochemical reactions and ionic conductivity in the cell. It was also mentioned that at the electrode-electrolyte interface, forced electron transfer can also form defects. No detailed discussion on the specifics of the phenomenon took place.

6.1.3. Air/O_2-Electrode Side Bond Layer

An O_2-electrode side protective bond layer is often used. Because it is next to the O_2-electrode, it encounters similar electrochemical phenomena that lead to cell degradation. GE's work also makes reference to bond layer issues. However, besides ANL's observations, at the workshop, no other studies or data were presented that can demonstrate the bond layer's significance relative to the O_2-electrode in terms of overall cell degradation. ANL found an average of 1-8% (~30% maximum) Cr-contamination in the bond layer, probably originating from interconnects. Cr contaminants were found in association with lanthanum strontium chromite (LSC). In the O_2 bond layer, a secondary phase may form. However, there are conflicting opinions about the severity of Cr contamination. ANL observed delamination and weak interface between the O_2-electrode and LSC bond layer, which can prevent solid-state Cr from diffusing into the O_2-electrode. For this reason the O_2-electrode can remain stable. However, a weak interface is not desirable from electrical conductivity point of view.

6.1.4. Electrolyte

In electrolytes, the main cause of degradation is loss of ionic conductivity. Müller et al. [43] showed that during first 1000 hr of testing, yttria- and scandia-doped zirconia (8 mol% Y_2O_3 Sc-ZrO_2 / 8YSZ) electrolytes showed ~ 23% performance degradation. For the next 1700 hr of testing, the decrease in conductivity was as high as 38%. An increase in tetragonal phase during annealing at the expense of cubic and monoclinic phases was detected for the 3YSZ samples. However, 3YSZ and 4YSZ samples showed much smaller decreases in conductivity after 2000 hr of test. Both Steinberger-Wilckens [44] and Hauch [45] reported formation of impurities at the TPBs. A substantial amount of SiO_2 was detected at the Ni/YSZ H2-electrode-electrolyte interface during electrolysis, while no Si was detected in other reference cells. This Si-containing impurities were probably from albite glass sealing. ANL observed that cubic, tetragonal, and monoclinic phases of ZrO_2 remained stable at the present scandia doping level.

6.1.5. Steam/H_2-Electrode

Overall many researchers reported that the contribution of the steam/H_2-electrode to SOEC degradation is much less than that attributed to other cell components. ANL also observed Si as a capping layer on steam/H_2-electrode. It probably was carried by steam from the seals, which contain Si. SiO_x also emanates from interconnect plates. Mn also diffuses from interconnects, but the significance of Mn diffusion is not known. Hauch [45] observed contaminants containing Si to segregate to the innermost few microns of the H2-electrode near the electrolyte. The

impurities that diffused to and accumulated at the TPBs of the H_2-electrode are believed to be the main cause of performance degradation in SOECs [45]. In the literature, it has been noted that a steam content greater than 30% shows conductivity loss. Therefore, an optimum ratio of steam-H_2 mixture and steam utilization percentage needs to be determined.

6.1.6. Interconnects

Interconnects can be a source of serious degradation. Sr, Ti, and Si segregate and build-up at interfaces. Sr segregates to the interconnect–bond layer interface. Mn segregates to the interconnect surface. Si and Ti segregate to the interconnect-passivation layer interface. Cr contamination can originate from interconnects and it can interact with O_2-electrode surface or even diffuse into the O_2-electrode. Chromium reduction (Cr^{6+} to Cr^{3+}) can take place at electrode-electrolyte interface [46]. Under the sponsorship of US-DOE SECA (Solid State Energy Conversion Alliance) program, coatings for the interconnects are being developed. Coated stainless steel interconnects have shown reduced degradation rates. GE observed higher degradation with stainless steel current collectors than with Au current collectors [47].

6.1.7. Contaminants and Impurities

A hydrogen electrolysis plant or a laboratory-scale experiment is always connected to piping, gas storage tanks/cylinders, or other such equipment. These components can be a source of undesirable particles/chemicals, which can get deposited at different locations in a solid oxide electrolysis cells. It has been shown in previous sections that any foreign particles depositing at the triple phase boundary can lead to degradation in the cell performance. The reactant gases can also have some undesirable impurities. It is understood that the balance of plant and gases are merely sources of impurities. The phenomenological causes of the degradation depend on other electrochemical reasons.

CONCLUDING REMARKS

High-temperature nuclear reactors have the potential for substantially increasing the efficiency of hydrogen production from water, with no consumption of fossil fuels, no production of greenhouse gases, and no other forms of air pollution. Water-splitting for hydrogen production can be accomplished via high-temperature electrolysis (HTE) or thermochemical processes, using high-temperature nuclear process heat. In order to achieve high efficiencies, both processes require high-temperature operation. Thus these hydrogen-production technologies are tied to the development of advanced high-temperature nuclear reactors. High-temperature electrolytic water-splitting supported by nuclear process heat and electricity has the potential to produce hydrogen with overall thermal-to-hydrogen efficiencies of 50% or higher, based on high heating value. This efficiency is near that of the thermochemical processes, but without the severe corrosive conditions of the thermochemical processes and without the fossil fuel consumption and greenhouse gas emissions associated with hydrocarbon processes.

An overview of the high-temperature electrolysis technology status and the HTE research and development program at the Idaho National Laboratory has been presented. Large-scale system analyses performed at the INL and elsewhere indicate very promising potential for high-temperature electrolysis as a large-scale hydrogen production technology. The INL HTE experimental program has demonstrated hydrogen production at a variety of scales from single button cells (~1 W) and short stacks (~500 W) to the successful operation of the 15 kW integrated laboratory scale facility (ILS). These experiments also served to demonstrate the

straightforward scalability of the HTE technology. The ILS demonstrated a peak hydrogen production rate in excess of 5.6 m^3/hr and operated for over 1000 hours the fall of 2008. Although some issues require further research and development, including cell and stack long-term performance degradation, HTE is the only advanced hydrogen production technology that has successfully demonstrated hydrogen production rates greater than ~100 L/hr.

Industry is currently preparing to begin mass production of solid oxide fuels cells, primarily for stationary power application. This commitment indicates that the issues of fuel cell manufacturing cost and long-term performance have reached a level of maturity that industry is comfortable in moving on to commercial deployment. It is likely that once the fundamental mechanisms of high-temperature electrolyzer cell degradation have been identified, long-term performance of solid-oxide electrolyzers will also improve drastically.

ACKNOWLEDGMENTS

This work was supported by the U.S. Department of Energy, Office of Nuclear Energy, Next Generation Nuclear Plant program as well as the Idaho National Laboratory, Laboratory Directed Research and Development Program. The Idaho National Laboratory is operated for the U.S. Department of Energy's Office of Nuclear Energy by the Battelle Energy Alliance under contract number DE-AC07-05ID14517.

REFERENCES

1. Yildiz, B., and Kazimi, M. S., "Efficiency of hydrogen production systems using alternative nuclear energy technologies," *Int. J. Hydrogen Energy*, Vol. 31, pp. 77-92, 2006.
2. O'Brien, J. E., McKellar, M. G., and Herring, J. S., "Performance Predictions for Commercial-Scale High-Temperature Electrolysis Plants Coupled to Three Advanced Reactor Types," 2008 International Congress on Advances in Nuclear Power Plants, Anaheim, CA, June 8-12, 2008.
3. O'Brien, J. E., "Thermodynamic Considerations for Thermal Water Splitting Processes and High-Temperature Electrolysis," 2008 ASME International Congress and Exposition, paper# IMECE2008-68880, Boston, Nov., 2008.
4. O'Brien, J. E., McKellar, M. G., Stoots, C. M., Herring, J. S., and Hawkes, G. L., "Parametric Study of Large-Scale Production of Syngas via High Temperature Electrolysis," in press, *International Journal of Hydrogen Energy*, 2009.
5. Stoots, C. M., O'Brien, J. E., "Results of Recent High-Temperature Co-electrolysis Studies at the Idaho National Laboratory," in press, *International Journal of Hydrogen Energy*, 2009.
6. Mogensen, M., Jensen, S. H., Hauch, A., Chorkendorff, lb., and Jacobsen, T., "Reversible Solid Oxide Cells*," Ceramic Engineering and Science Proceedings*, V 28, n 4, Advances in Solid Oxide Fuel Cells III - A Collection of Papers Presented at the 31st International Conference on Advanced Ceramics and Composites, 2008, p 91-101.
7. Nomura, M., Kasahara, S., and Onuki, K., "Estimation of Thermal Efficiency to produce Hydrogen from Water through IS Process," Proc., 2nd Topical Conference on Fuel Cell Technology, AIChE Spring National Meeting, New Orleans, 2003.
8. Abraham, B. M., and Schreiner, F., "General Principles Underlying Chemical Cycles which Thermally Decompose Water into the Elements," *Ind. Eng. Chem. Fundam.*, Vol. 13, No. 4, 1974.

9. Fletcher, E. A., and Moen, R. L., "Hydrogen and Oxygen from Water," Science, Vol. 197, pp. 1050-1056, 1977.
10. O'Brien, J. E., McKellar, M. G., and Herring, J. S., "Performance Predictions for Commercial-Scale High-Temperature Electrolysis Plants Coupled to Three Advanced Reactor Types," ANS International Congress on Advances in Nuclear Power Plants (ICAPP08), June 8-12, 2008, Anaheim, CA.
11. UniSim Design, R360 Build 12073, Copyright ©2005-2006 Honeywell International Inc.
12. Yildiz, B., and Kazimi, M. S., "Efficiency of hydrogen production systems using alternative nuclear energy technologies," *Int. J. Hydrogen Energy*, Vol. 31, pp. 77-92, 2006.
13. Brown, L. C., Lentsch, R. D., Besenbruch, G. E., Schultz, K. R., "Alternative Flowsheets for the Sulfur-Iodine Thermochemical Hydrogen Cycle," *AIChE Journal,* April 2003.
14. Southworth, F., Macdonald, P. E., Harrell, D. J., Park, C. V., Shaber, E. L., Holbrook, M. R., and Petti, D. A., "The Next Generation Nuclear Plant (NGNP) Project," Proceedings, Global 2003, pp. 276-287, 2003.
15. O'Brien, J. E., Stoots, C. M., McKellar, M. G., Harvego, E. A., Condie, K. G., Housley, G. K., Herring, J. S., and Hartvigsen, J. J., "Status of the INL High Temperature Electrolysis Research Program – Experimental and Modeling," Fourth Information Exchange Meeting on Nuclear Hydrogen, NEA, Oakbrook, IL, April 14-16, 2009.
16. Larminie, J. and Dicks, A., *Fuel Cell Systems Explained*, John Wiley & Sons, New York, 2003.
17. Stoots, C. M., O'Brien, J. E., McKellar, M. G., Hawkes, G. L., and Herring, J. S., "Engineering Process Model for High-Temperature Steam Electrolysis System Performance Evaluation," AIChE 2005 Annual Meeting, Cincinnati, Oct. 30 – Nov. 4, 2005.
18. O'Brien, J. E., Stoots, C. M., and Hawkes, G. L., "Comparison of a One-Dimensional Model of a High-Temperature Solid-Oxide Electrolysis Stack with CFD and Experimental Results," Proceedings, 2005 ASME International Mechanical Engineering Congress and Exposition, Nov. 5 – 11, Orlando.
19. Williams, M. C., Strakey, J. P., Surdoval, W. A., Wilson, L. C., "Solid oxide fuel cell technology development in the US," *Solid State Ionics*, V. 177, No. 19-25, pp. 2039-2044, Oct. 2006.
20. Ni, M., Leung, M. K. H., and Leung, D. Y. C. (2006). "A Modeling Study on Concentration Overpotentials of a Reversible Solid Oxide Fuel Cell," J. Power Sources, 163, 460-466.
21. Singhal, S. C., and Kendall, K., *Solid Oxide Fuel Cells*, Elsevier Advanced Technology, Oxford, UK, 2003.
22. O'Brien, J. E., Stoots, C. M., Herring, J. S., Lessing, P. A., Hartvigsen, J. J., and Elangovan, S., "Performance Measurements of Solid-Oxide Electrolysis Cells for Hydrogen Production," Journal of Fuel Cell Science and Technology, Vol. 2, pp. 156-163, August 2005.
23. O'Brien, J. E., Stoots, C. M., Herring, J. S., and Hartvigsen, J. J.,"Hydrogen Production Performance of a 10-Cell Planar Solid-Oxide Electrolysis Stack," *Journal of Fuel Cell Science and Technology*, Vol. 3, pp. 213-219, May, 2006.
24. O'Brien, J. E., Stoots, C. M., Herring, J. S., and Hartvigsen, J. J., "Performance of Planar High-Temperature Electrolysis Stacks for Hydrogen Production from Nuclear Energy," *Nuclear Technology*, Vol. 158, pp. 118 - 131, May, 2007.
25. Stoots, C. M., O'Brien, J. E., Herring, J. S., and Hartvigsen, J. J., "Syngas Production via High-Temperature Coelectrolysis of Steam and Carbon Dioxide," *Journal of Fuel Cell Science and Technology*, Vol. 6, part 1, paper no. 011014, pp. 1-12, February, 2009.

26. Steinberger-Wilkens, R. Tietz, F., Smith, M. J., Mougin, J., Rietveld, B., Bucheli, O., Van Herle, J., Mohsine, Z., and Holtappels, P., "Real-SOFC – A Joint European Effort in Understanding SOFC Degradation," *ECS Transactions*, v 7, n 1 PART 1, *ECS Transactions - 10th International Symposium on Solid Oxide Fuel Cells, SOFC-X*, 2007, pp. 67-76.
27. Haering, C., Roosen, A., Schichl, H., and Schnoller, M., "Degradation of the electrical conductivity in stabilized zirconia system Part II: Scandia-stabilised zirconia," *Solid Sate Ionics*, Vol. 176, No 3-4, pp. 261-268, Jan., 2005.
28. Housley, G., Condie, K., O'Brien, J.E., Stoots, C.M., "Design of an Integrated Laboratory Scale Experiment for Hydrogen Production via High Temperature Electrolysis," paper no. 172431, ANS Embedded Topical: International Topical Meeting on the Safety and Technology of Nuclear Hydrogen Production, Control, and Management, June 24 - 28, 2007, Boston, Massachusetts, USA.
29. Stoots, C. M., O'Brien, J. E., "Initial Operation of the High-Temperature Electrolysis Integrated Laboratory Scale Experiment at INL," 2008 International Congress on Advances in Nuclear Power Plants, June 8-12, 2008, Anaheim, CA.
30. Stoots, C. M., O'Brien, J. E., Condie, K., Moore-McAteer, L., Housley, G. K., Hartvigsen, J. J., and Herring, J. S., "The High-Temperature Electrolysis Integrated Laboratory Experiment," *Nuclear Technology*, April, 2009.
31. Housley, G. K., O'Brien, J. E., and Hawkes, G. L., "Design of a Compact Heat Exchanger for Heat Recuperation from a High Temperature Electrolysis System," 2008 ASME International Congress and Exposition, paper# IMECE2008-68917, Boston, Nov., 2008.
32. Forsberg, C. W., "Is Hydrogen the Future of Nuclear Energy?" Proceedings, International Topical Meeting on the Safety and Technology of Nuclear Hydrogen Production, Control, and Management, ANS Embedded Topical, 2007.
33. Harvego, E. A., McKellar, M. G., and O'Brien, J. E., "System Analysis of Nuclear-Assisted Syngas Production from Coal," *Journal of Engineering for Gas Turbines and Power*, Vol. 131, July, 2009.
34. McKellar, M. G., Hawkes, G. L., and O'Brien, J. E., "The Production of Syngas via High-Temperature Electrolysis and Bio-Mass Gasification, Proceedings of the 2008 ASME International Mechanical Engineering Congress and Exposition, paper# IMECE2008-68900, Boston, MA, Nov., 2008.
35. Harvego, E. A., McKellar, M. G., Sohal, M. S., O'Brien, J. E., and Herring, J. S., "Economic Analysis of a Nuclear Reactor Powered High Temperature Electrolysis Hydrogen Production Plant," ASME 2nd International Conference on Energy Sustainability, Jacksonville, FL, August 10-14, 2008.
36. Ivy, J., "Summary of Electrolytic Hydrogen Production," NREL Report NREL/MP-560-36734, September, 2004.
37. Prinkey, M., Shahnam, M., and Rogers, W. A., "SOFC FLUENT Model Theory Guide and User Manual," Release Version 1.0, FLUENT, Inc., 2004.
38. Hawkes, G. L., O'Brien, J. E., Stoots, C. M., Herring, J. S., Shahnam, M., "CFD Model of a Planar Solid Oxide Electrolysis Cell for Hydrogen Production from Nuclear Energy," to be presented at the 11th International Topical Meeting on Nuclear Reactor Thermal-Hydraulics NURETH-11, Popes Palace Conference Center, Avignon, France, October 2-6, 2005.

39. O'Brien, J. E., Stoots, C. M., Herring, J. S., and Hartvigsen, J. J.,"Hydrogen Production Performance of a 10-Cell Planar Solid-Oxide Electrolysis Stack," Proceedings, ASME 3rd International Conference on Fuel Cell Science, Engineering, and Technology, May 23 – 25, 2005, Ypsilanti, MI.
40. O'Brien, J. E., Herring, J. S., Stoots, C. M., Lessing, P. A., "High-Temperature Electrolysis for Hydrogen Production From Nuclear Energy," to be presented at the 11th International Topical Meeting on Nuclear Reactor Thermal-Hydraulics NURETH-11, Popes Palace Conference Center, Avignon, France, October 2-6, 2005.
41. Sohal, M. S., "Degradation in Solid Oxide Cells during High Temperature Electrolysis," INL External report, INL/EXT-09-15617, June, 2009.
42. Virkar, A. V. (2007). "A Model for Solid Oxide Fuel Cell (SOFC) Stack Degradation," J. Power Sources, 172, 713-724.
43. Müller, A.C., Weber, A., Herbstritt, D., and Ivers-Tiffée, E. (2003). "Long Term Stability of Yttria and Scandia doped Zirconia Electrolytes," Proceedings 8th International Symposium on SOFC, (Edited by) Singhal, S. C., Dokiya, M., PV 2003-07, The Electrochemical Society, 196-199.
44. Steinberger-Wilckens, R. (2008), "Degradation Issues in SOFCs," Presented at the Workshop on Degradation in Solid Oxide Electrolysis Cells and Strategies for its Mitigation, October 27, 2008, Fuel Cell Seminar & Exposition, Phoenix, AZ.
45. Hauch, A. (2007). "Solid Oxide Electrolysis Cells – Performance and Durability," Ph.D. Thesis, Technical University of Denmark, Risø National Laboratory, Roskilde, Denmark.
46. Singh, P., Pederson, L. R., Stevenson, J. W., King, D. L., and McVay, G. L., "Understanding Degradation Processes in Solid Oxide Fuel Cell Systems," Presented at the Workshop on Degradation in Solid Oxide Electrolysis Cells and Strategies for its Mitigation, October 27, 2008, Fuel Cell Seminar & Exposition, Phoenix, AZ.
47. Guan, J. et al. (2006). "High Performance Flexible Reversible Solid Oxide Fuel Cell," GE Global Research Center Final Report for DOE Cooperative Agreement DE-FC36-04GO-14351.

BIBLIOGRAPHY OF INL PUBLICATIONS ON HIGH TEMPERATURE ELECTROLYSIS

Journal Articles

J1. O'Brien, J. E., McKellar, M. G., Harvego, E. A., and Stoots, C. M., "High-Temperature Electrolysis for Large-Scale Hydrogen and Syngas Production from Nuclear Energy – Summary of System Simulation and Economic Analyses," *International Journal of Hydrogen Energy*, in press, 2009.

J2. Harvego, E. A., McKellar, M. G., Sohal, M. S., O'Brien, J. E., and Herring, J. S., "System Evaluation and Economic Analysis of a Nuclear Reactor Powered High Temperature Electrolysis Hydrogen Production Plant," *Journal of Energy Resources Technology*, in review, 2009.

J3. Stoots, C. M., O'Brien, J. E., Condie, K. G., and Hartvigsen, J. J., "High-Temperature Electrolysis for Large-Scale Hydrogen Production from Nuclear Energy – Experimental Investigations," *International Journal of Hydrogen Energy*, in press, 2009.

J4. O'Brien, J. E., Stoots, C. M., Hawkes, G. L., McKellar, M. G., and Herring, J. S., and "High Temperature Electrolysis of Steam," Chapter 18, High Temperature Electrolysis, in *The CRC Nuclear Hydrogen Production Handbook*, edited by Ryutaro Hino and Xing Yan of the Japan Atomic energy Agency, Taylor and Francis, New York, 2010.

J5. Stoots, C. M., O'Brien, J. E., Herring, J. S., Hartvigsen, J. J., "High Temperature Electrolysis of Steam and CO2 for Syngas Production," Chapter 8, *Syngas: Production Methods, Post Treatment, and Economics,* edited by Dr. Frank Columbus, Nova Science Publishers, New York, 2009.

J6. Stoots, C. M., O'Brien, J. E., Condie, K., Moore-McAteer, L., Housley, G. K., Hartvigsen, J. J., and Herring, J. S., "The High-Temperature Electrolysis Integrated Laboratory Experiment," *Nuclear Technology*, Vol. 166, No. 1, pp. 32 – 42, April, 2009.

J7. Harvego, E. A., McKellar, M. G., and O'Brien, J. E., "System analysis of Nuclear-Assisted Syngas Production from Coal," *Journal of Engineering for Gas Turbines and Power*, Vol. 131, pp. 042901-1-5, July, 2009.2008.

J8. O'Brien, J. E., McKellar, M. G., Stoots, C. M., Herring, J. S., and Hawkes, G. L., "Parametric Study of Large-Scale Production of Syngas via High Temperature Electrolysis," *International Journal of Hydrogen Energy*, Vol. 34, pp. 4216-4226, May, 2009.

J9. Hartvigsen, J. J., Elangovan, S., Frost, L., Nickens, A., Stoots, C. M., O'Brien, J. E., and Herring, J. S., "Carbon Dioxide Recycling by High Temperature Co-electrolysis and Hydrocarbon Synthesis," *Electrochemical Society Transactions*, Vol. 12, March, 2008.

J10. Stoots, C. M., O'Brien, J. E., "Results of Recent High-Temperature Co-electrolysis Studies at the Idaho National Laboratory," *International Journal of Hydrogen Energy,* Vol. 34, Issue 9, pp. 4208-4215, May 2009, , 2009.

J11. Hawkes, G. L., O'Brien, J. E., and Stoots, C. M., "3D CFD Model of a Multi-Cell High Temperature Electrolysis Stack, *International Journal of Hydrogen Energy*, Vol. 34, Issue 9, pp. 4189-4197, May 2009.

J12. Stoots, C. M., O'Brien, J. E., Herring, J. S., and Hartvigsen, J. J., "Syngas Production via High-Temperature Coelectrolysis of Steam and Carbon Dioxide," *Journal of Fuel Cell Science and Technology*, Vol. 6, issue 1, paper no. 011014, pp. 1-12, February, 2009.

J13. Harvego, E. A., McKellar, M. G., O'Brien, J. E., Herring, J. S., "Parametric Evaluation of High-Temperature Electrolysis Hydrogen Production Processes using Different Advanced Nuclear Reactor Heat Sources," *Nuclear Engineering and Design*, in press, November, 2007.

J14. O'Brien, J. E., Stoots, C. M., Herring, J. S., and Hartvigsen, J. J., "Performance of Planar High-Temperature Electrolysis Stacks for Hydrogen Production from Nuclear Energy," *Nuclear Technology*, Vol. 158, pp. 118 - 131, May, 2007.

J15. Hawkes, G. L., O'Brien, J. E., Stoots, C. M., Herring, J. S., "CFD Model of a Planar Solid Oxide Electrolysis Cell for Hydrogen Production from Nuclear Energy," *Nuclear Technology*, Vol. 158, pp. 132 - 144, May, 2007.

J16. Herring, J. S., O'Brien, J. E., Stoots, C. M., and Hawkes, G. L., "Progress in High-Temperature Electrolysis for Hydrogen Production using Planar SOFC Technology," *International Journal of Hydrogen Energy*, Vol. 32, Issue 4, pp. 440-450, March 2007.

J17. Harvego, E. A., Reza, S. M. M., Richards, M., and Shenoy, A., "An Evaluation of Reactor Cooling and Coupled Hydrogen Production Processes using the Modular Helium Reactor," *Nuclear Engineering and Design*, Vol. 236, pp. 1481-1489, 2006.

J18. Richards, M., Shenoy, A., Schultz, K., Brown, L., Harvego, E. A., McKellar, M. G., Coupey, J. P., Reza, S. M. M., and Okamoto, F., "H2-MHR Conceptual Designs based on the Sulphur–Iodine Process and High-Temperature Electrolysis," *Int. J. Nuclear Hydrogen Production and Applications,* Vol. 1, No. 1, 2006, pp. 36 – 50.

J19. O'Brien, J. E., Stoots, C. M., Herring, J. S., and Hartvigsen, J. J.,"Hydrogen Production Performance of a 10-Cell Planar Solid-Oxide Electrolysis Stack," *Journal of Fuel Cell Science and Technology*, Vol. 3, pp. 213-219, May, 2006.

J20. Lessing, P. A., "A Review of Sealing Technologies Applicable to Solid Oxide Electrolysis Cells," *Journal of Materials Science*, Vol. 42, No. 10, pp. 3465-3476, May 2007.

J21. Lessing, P. A., "Materials for Hydrogen Generation via Water Electrolysis," *Journal of Materials Science*, Vol. 42, No. 10, pp. 3477-3487, May 2006.

J22. Lessing, P. A., "Materials for Water Electrolysis Cells", Chapter 2, *Materials for the Hydrogen Economy*, Russ Jones and George Thomas, editors; CRC Press, Taylor&Francis Group, Boca Raton, FL, 2008.

J23. O'Brien, J. E., Stoots, C. M., Herring, J. S., Lessing, P. A., Hartvigsen, J. J., and Elangovan, S., "Performance Measurements of Solid-Oxide Electrolysis Cells for Hydrogen Production," *Journal of Fuel Cell Science and Technology*, Vol. 2, pp. 156-163, August 2005.

J24. Herring, J. S., O'Brien, J. E., Stoots, C. M., Lessing, P. A., Anderson, R. P., Hartvigsen, J. J., and Elangovan, S., "Hydrogen Production through High-Temperature Electrolysis," *Nuclear Production of Hydrogen - Technologies and Perspectives for Global Deployment*, Chapter 3, edited by Dr. Masao Hori, *Current Issues in Nuclear Energy Series*, International Nuclear Societies Council, 2004.

Conference Papers

C1. Hartvigsen, J. J., Elangovan, S., Frost, L., Stoots, C. M., O'Brien, J. E., Herring, J. S., Sohal, M. S., and Hawkes, G. H., "Carbon Dioxide Recycling by High Temperature Co-electrolysis and Hydrocarbon Synthesis," Carbon Dioxide and other Greenhouse Gas Reduction Metallurgy Symposium, TMS 2010, February 14 – 18, 2010, Seattle, WA.

C2. Milobar, D. G., Li, P., and O'Brien, J. E., "Analytical Study, 1-D Optimization Modeling, and Testing of Electrode-Supported Solid Oxide Electrolysis Cells," Proceedings, ASME Micro/Nanoscale Heat and Mass Transfer International Conference, paper no. MNHMT2009-18261, December 18-22, 2009, Shanghai, China.

C3. O'Brien, J. E., Housley, G. K., Milobar, D. G., and Petigny, N., "Performance of Single Electrode-Supported Cells Operating in the Electrolysis Mode, Proceedings, 2009 ASME International Congress and Exposition, paper no. IMECE2009-11683, November 13-19, 2009, Lake Buena Vista, FL.

C4. Stoots, C. M., O'Brien, J. E., and Cable, T., "Test Results from the Idaho National Laboratory of the NASA Bi-Supported Cell Design," Proceedings, 2009 ASME International Congress and Exposition, paper no. IMECE2009-11646, November 13-19, 2009, Lake Buena Vista, FL.

C5. Stoots, C. M., O'Brien, J. E., Herring, J. S., Condie, K. G., Moore-McAteer, L., Hartvigsen, J. J., and Larsen, D., "High Temperature Solid-Oxide Electrolyzer 2500-Hour Test Results at the Idaho National Laboratory," 2009 AIChE Annual Meeting, November 8 – 13, 2009, Nashville, TN.

C6. Hawkes, G. L. and McKellar, M. G., "Liquid Fuel Production from Biomass via High Temperature Steam Electrolysis," 2009 AIChE Annual Meeting, November 8 – 13, 2009, Nashville, TN.

C7. Harvego, E. A., O'Brien, J. E., McKellar, M. G., "System Analysis of High and Low Temperature Interface Designs for a Nuclear-Driven High Temperature Electrolysis Hydrogen Production Plant," International Conference on Nuclear Energy, paper no. ICONE17-75473, Brussels, Belgium, July 12-16, 2009.

C8. Stoots, C. M., Condie, K. G., O'Brien, J. E., Herring, J. S., and Hartvigsen, J. J., "Test Results from the Idaho National Laboratory 15 kW High Temperature Electrolysis Test Facility," International Conference on Nuclear Energy, paper no. ICONE17-75417, Brussels, Belgium, July 12-16, 2009.

C9. O'Brien, J. E., Stoots, C. M., Herring, J. S., Condie, K. G., and Housley, G. K., "The High-Temperature Electrolysis Program at the Idaho National Laboratory: Observations on Performance Degradation," High Temperature Water Electrolysis Limiting Factors, Eifer, Karlsruhe, Germany, June 9-10, 2009.

C10. Stoots, C. M., O'Brien, J. E., Herring, J. S., Hartvigsen, J. J., "High Temperature Electrolysis Experimental Activities at the Idaho National Laboratory," High Temperature Water Electrolysis Limiting Factors, Eifer, Karlsruhe, Germany, June 9-10, 2009.

C11. O'Brien, J. E., McKellar, M. G., Harvego, E. A., and Stoots, C. M., "High-Temperature Electrolysis for Large-Scale Hydrogen and Syngas Production from Nuclear Energy – system Simulation and Economics," International Conference on Hydrogen Production, ICH2P-09, Oshawa, Canada, May 3-6, 2009.

C12. Stoots, C. M., O'Brien, J. E., Condie, K. G., and Hartvigsen, J. J., "High-Temperature Electrolysis for Large-Scale Hydrogen Production from Nuclear Energy – Experimental Investigations," International Conference on Hydrogen Production, ICH2P-09, Oshawa, Canada, May 3-6, 2009.

C13. O'Brien, J. E., Stoots, C. M., McKellar, M. G., Harvego, E. A., Condie, K. G., Housley, G. K., Herring, J. S., and Hartvigsen, J. J., "Status of the INL High Temperature Electrolysis Research Program – Experimental and Modeling," Proceedings, Fourth Information Exchange Meeting on Nuclear Hydrogen, NEA, Oakbrook, IL, April 14-16, 2009.

C14. O'Brien, J. E., "Thermodynamic Considerations for Thermal Water Splitting Processes and High-Temperature Electrolysis," 2008 ASME International Congress and Exposition, paper# IMECE2008-68880, Boston, Nov., 2008.

C15. Housley, G. K., O'Brien, J. E., and Hawkes, G. L., "Design of a Compact Heat Exchanger for Heat Recuperation from a High Temperature Electrolysis System," 2008 ASME International Congress and Exposition, paper# IMECE2008-68917, Boston, Nov., 2008.

C16. Hawkes, G. L., O'Brien, "3D CFD Electrochemical and Heat Transfer Model of an Integrated-Planar Solid Oxide Electrolysis Cell," 2008 ASME International Congress and Exposition, paper# IMECE2008-68866, Boston, Nov., 2008.

C17. Stoots, C. M., O'Brien, J. E, Herring, J. S., and Hartvigsen, J. J., "Recent Progress at the Idaho National Laboratory in High Temperature Electrolysis for Hydrogen and Syngas Production," 2008 ASME International Mechanical Engineering Congress and Exposition, paper# IMECE2008-68440, Boston, MA, Nov., 2008.

C18. McKellar, M. G., Hawkes, G. L., and O'Brien, J. E., "The Production of Syngas via High-Temperature Electrolysis and Bio-Mass Gasification," 2008 ASME International Mechanical Engineering Congress and Exposition, paper# IMECE2008-68900, Boston, MA, Nov., 2008.

C19. Harvego, E. A., McKellar, M. G., and O'Brien, J. E., "System Analysis of Nuclear-Assisted Syngas Production from Coal," Proceedings, 4th International Topical Meeting on High Temperature Reactor Technology, paper# HTR2008-58085, Washington, DC, Sept. 2008.

C20. Stoots, C. M., O'Brien, J. E., Herring, J. S., Condie, K. G., and Hartvigsen, J. J., "Idaho National Laboratory Experimental Research in High Temperature Electrolysis for Hydrogen and Syngas Production, Proceedings, 4th International Topical Meeting on High Temperature Reactor Technology, paper# HTR2008-58086, Washington, DC, Sept. 2008.

C21. Harvego, E. A., McKellar, M. G., Sohal, M. S., O'Brien, J. E., and Herring, J. S., "Reference Design and Economic Analysis for a Nuclear-Driven High-Temperature-Electrolysis Hydrogen Production Plant," ASME 2nd International Conference on Energy Sustainability, paper# 54206, Jacksonville, FL, August 10-14, 2008.

C22. Hawkes, G L., O'Brien, J. E., Stoots, C. M., and Herring, J. S., "3D CFD Modeling of Solid Oxide Electrolysis Cells and Stacks," 8th European Solid Oxide Fuel Cell Forum, Lucerne, June 30 – July 4, 2008.

C23. Stoots, C. M., O'Brien, J. E., Herring, J. S., and Hartvigsen, J. J., "High Temperature Coelectrolysis For Direct Syngas Production Using Solid-Oxide Cells," 8th European Solid Oxide Fuel Cell Forum, paper# A112, Lucerne, June 30 – July 4, 2008.

C24. O'Brien, J. E., Stoots, C. M., McKellar, M. G., and Herring, J. S., "Demonstration and System Analysis of High Temperature Steam Electrolysis for Large-Scale Hydrogen Production using SOFCs," 8th European Solid Oxide Fuel Cell Forum, Lucerne, paper# A114, June 30 – July 4, 2008.

C25. Stoots, C. M., O'Brien, J. E., Herring, J. S., and Hartvigsen, J. J., "Design and Initial Operation of a Multi-Kilowatt High Temperature Steam Electrolysis Test Facility at the Idaho National Laboratory," 6th International Fuel Cell Science, Engineering & Technology Conference, paper# 65124, June 16-18, 2008, Denver, CO.

C26. Hawkes, G. L., O'Brien, J. E., Haberman, B., Marquis, A. J., Martinez Baca, C., Tripepi, D., Costamagna, P., "Numerical Prediction of Performance of Integrated Planar Solid Oxide Fuel Cell, With Comparison of Results from Several Codes," 6th International Fuel Cell Science, Engineering & Technology Conference, paper #65179, June 16-18, 2008, Denver, CO.

C27. O'Brien, J. E., McKellar, M. G., and Herring, J. S., "Performance Predictions for Commercial-Scale High-Temperature Electrolysis Plants Coupled to Three Advanced Reactor Types," 2008 International Congress on Advances in Nuclear Power Plants, June 8-12, 2008, Anaheim, CA.

C28. Stoots, C. M., O'Brien, J. E., "Initial Operation of the High-Temperature Electrolysis Integrated Laboratory Scale Experiment at INL," 2008 International Congress on Advances in Nuclear Power Plants, June 8-12, 2008, Anaheim, CA.

C29. Hawkes, G. L., McKellar, M. G., Stoots, C. M., O'Brien, J. E., and Wood, R. A., "Biomass to Liquid Fuels via High Temperature Electrolysis," presentation only, International Biomass 2008 Conference and Trade Show, Minneapolis, Minnesota, April 15-17, 2008.

C30. Sohal, M. S., O'Brien, J. E., Soots, C. M., McKellar, M. G., and Herring, J. S., "Challenges in Generating Hydrogen by High Temperature Electrolysis using Solid Oxide Cells," National Hydrogen Association Annual Hydrogen Conference 2008, March 30- April 3, 2008, Sacramento.

C31. Hartvigsen, J. J., Elangovan, S., Frost, L., Nickens, A., Stoots, C. M., O'Brien, J. E., Herring, J. S., "Carbon Dioxide Recycling by High Temperature Co-Electrolysis and Hydrocarbon Synthesis," Annual Meeting & Exhibition, The Minerals, Metals & Materials Society, March 9 – 13, 2008, New Orleans.

C32. Sohal, M. S., Herring, J. S., O'Brien, J. E., Stoots, C.M., Hawkes, G. L., and McKellar, M. G., "Nuclear Energy Powered Hydrogen Generation using Solid Oxide Electrolyzer," Workshop on New Horizons in Nuclear Reactor Thermal Hydraulics, Bhabha Atomic Research Centre (BARC), Mumbai, India, Jan. 7-8, 2008.

C33. McKellar, M. G., O'Brien, J. E., Stoots, C. M., and Hawkes, G. L., "A Process Model for the Production of Syngas Via High Temperature Co-Electrolysis," paper # IMECE2007-43658, 2007 ASME International Congress and Exposition, Seattle, Nov., 2007.

C34. Stoots, C.M., O'Brien, J.E., and Hartvigsen, J., "Carbon-Neutral Production of Syngas Via High Temperature Electrolytic Reduction of Steam And CO_2," paper # IMECE2007-43667, 2007 ASME International Congress and Exposition, Seattle, Nov., 2007.

C35. Stoots, C. M., O'Brien, J. E., "Results of Recent High-Temperature Co-electrolysis Studies at the Idaho National Laboratory," paper # 412b, 2007 AIChE Annual Meeting, Salt Lake City, November 4 – 9, 2007.

C36. Herring, J. S., Stoots, C. M., O'Brien, J. E., and Hartvigsen, J. J., "Recent Progress in High Temperature Electrolysis," paper # 412a, 2007 AIChE Annual Meeting, Salt Lake City, November 4 – 9, 2007.

C37. Hawkes, G. L., O'Brien, J. E., and Stoots, C. M., "3D CFD Model of a Multi-Cell High Temperature Electrolysis Stack, paper # 412d, 2007 AIChE Annual Meeting, Salt Lake City, November 4 – 9, 2007.

C38. O'Brien, J. E., McKellar, M. G., Stoots, C. M., Herring, J. S., and Hawkes, G. L., "Parametric Study of Large-Scale Production of Syngas via High Temperature Electrolysis," paper # 412c, 2007 AIChE Annual Meeting, Salt Lake City, November 4 – 9, 2007.

C39. Stoots, C.M., O'Brien, J.E., Herring, J. S., Housley, G., Condie, K., Hawkes, G. L., McKellar, M. G., Hartvigsen, J., "Progress in High Temperature Electrolysis at the Idaho National Laboratory," 2007 Fuel Cell Seminar, Paper # 390, San Antonio, Texas, Oct 15-19, 2007.

C40. Hawkes, G. L., Hawkes, B. D., Sohal, M. S., Torgerson, P. T., Armstrong, T. R., and Williams, M. C., "3D CFD Model of a Tubular Porous-Metal Supported Solid Oxide Electrolysis Cell," 2007 Fuel Cell Seminar, Paper # 119, San Antonio, Texas, Oct 15-19, 2007.

C41. Herring, J. S., O'Brien, J. E., Stoots, C. M., and Housley, G. K., "Recent Results in the Development of High Temperature Electrolysis for Hydrogen Production," GLOBAL 2007, paper no. 180109, September 9-13, 2007, Boise, ID.

C42. Hawkes, G. L., O'Brien, J. E., Stoots, C. M., Herring, J. S., and Jones, R. W., "CFD Model of a Planar Solid Oxide Electrolysis Cell: Base Case and Variations," paper # HT2007-32310, 2007 ASME-JSME Thermal Engineering Conference and Summer Heat Transfer Conference, July 8 – 12, 2007, Vancouver, BC, Canada.

C43. O'Brien, J.E., Stoots, C., Herring, J.S., and Hartvigsen, J., "High-Temperature Co-electrolysis of Carbon Dioxide and Steam for the Production of Syngas: Equilibrium Model and Single-Cell Tests," paper no. 173084, ANS Embedded Topical: International Topical Meeting on the Safety and Technology of Nuclear Hydrogen Production, Control, and Management, June 24 - 28, 2007, Boston, Massachusetts, USA.

C44. Stoots, C.M., O'Brien, J.E., and Hartvigsen, J., "Test Results of High Temperature Steam/CO2 Coelectrolysis in a 10-Cell Stack," paper no. 173131, ANS Embedded Topical: International Topical Meeting on the Safety and Technology of Nuclear Hydrogen Production, Control, and Management, June 24 - 28, 2007, Boston, Massachusetts, USA.

C45. Hawkes, G.L., O'Brien, J.E., Stoots, C.M., Herring, S.J., and Hartvigsen, J., "3D CFD Model of High Temperature H2O/CO2 Co-Electrolysis," paper no., 173216, ANS Embedded Topical: International Topical Meeting on the Safety and Technology of Nuclear Hydrogen Production, Control, and Management, June 24 - 28, 2007, Boston, Massachusetts, USA.

C46. Hartvigsen, J.J., Elangovan, S., Stoots, C.M., O'Brien, J.E., and Herring, J.S., "Pre-ILS Demonstration Of Planar Solid Oxide Fuel Cell Technology Readiness For Application In Nuclear Hydrogen Production," paper no. 173733, ANS Embedded Topical: International Topical Meeting on the Safety and Technology of Nuclear Hydrogen Production, Control, and Management, June 24 - 28, 2007, Boston, Massachusetts, USA.

C47. Steffen, C. J. Jr., McKellar, M. G., Harvego, E. A., and O'Brien, J. E., "The Effect of Electrolysis Temperature on Hydrogen Production Efficiency," paper no. 171599, ANS Embedded Topical: International Topical Meeting on the Safety and Technology of Nuclear Hydrogen Production, Control, and Management, June 24 - 28, 2007, Boston, Massachusetts, USA.

C48. Housley, G., Condie, K., O'Brien, J.E., Stoots, C.M., "Design of an Integrated Laboratory Scale Experiment for Hydrogen Production via High Temperature Electrolysis," paper no. 172431, ANS Embedded Topical: International Topical Meeting on the Safety and Technology of Nuclear Hydrogen Production, Control, and Management, June 24 - 28, 2007, Boston, Massachusetts, USA

C49. Herring, J.S., O'Brien, J.E., Stoots, C.M., Hartvigsen, J., Petri, M.C., Carter, J.D., and Bischoff, B.L., "Overview of High-Temperature Electrolysis for Hydrogen Production," paper no. 175960, ANS Embedded Topical: International Topical Meeting on the Safety and Technology of Nuclear Hydrogen Production, Control, and Management, June 24 - 28, 2007, Boston, Massachusetts, USA.

C50. Cadwallader, L. C., DeWall, K. G., and Herring, J. S., "Hydrogen and Oxygen Gas Monitoring System Design and Operation," paper no. 172431, ANS Embedded Topical: International Topical Meeting on the Safety and Technology of Nuclear Hydrogen Production, Control, and Management, June 24 - 28, 2007, Boston, Massachusetts, USA.

C51. Demkowicz, P., Medvedev, P. and DeWall, K., "Materials Degradation Studies for High-Temperature Electrolysis Systems," paper no. 172796, ANS Embedded Topical: International

Topical Meeting on the Safety and Technology of Nuclear Hydrogen Production, Control, and Management, June 24 - 28, 2007, Boston, Massachusetts, USA.

C52. O'Brien, J.E., Stoots, C.M., Hawkes, G.L., Herring, J.S., and Hartvigsen, J., "High-Temperature Coelectrolysis of Steam and Carbon Dioxide for Direct Production of Syngas: Equilibrium Model and Single-Cell Tests," submitted, Fifth International Conference on Fuel Cell Science, Engineering & Technology, June 18-20, 2007, New York, USA.

C53. Stoots, C.M., O'Brien, J.E., and Hartvigsen, J., "Syngas Production Via High-Temperature Coelectrolysis of Steam and Carbon Dioxide In A Solid-Oxide Stack," submitted, Fifth International Conference on Fuel Cell Science, Engineering & Technology, June 18-20, 2007, New York, USA.

C54. O'Brien, J. E., McKellar, M. G., Hawkes, G. L., and Stoots, C. M., "Development of a One-Dimensional Co-Electrolysis Model for Use in Large-Scale Process Modeling Analysis," submitted, Fifth International Conference on Fuel Cell Science, Engineering & Technology, June 18-20, 2007, New York, USA.

C55. Hawkes, G. L., Hawkes, B. D., Sohal, M. S., Torgerson, P. T., Williams, M. C., "Tubular Porous-Metal Supported Solid Oxide Fuel/Electrolysis Cell: Part 1: CFD and Electrochemical Model," Fifth International Conference on Fuel Cell Science, Engineering & Technology, June 18-20, 2007, New York, USA. (presentation only)

C56. Hawkes, B. D., Hawkes, G. L., Sohal, M. S., Torgerson, P. T., Williams, M. C., "Tubular Porous-Metal Supported Solid Oxide Fuel/Electrolysis Cell: Part 2: Thermal-Stress Model," Fifth International Conference on Fuel Cell Science, Engineering & Technology, June 18-20, 2007, New York, USA. (presentation only)

C57. Schultz, K., Sink, Herring, J. S., O'Brien, J. E., Buckingham, R., Summers, W., and Michele Lewis, M., "Status of the US Nuclear Hydrogen Initiative," Proceedings of ICAPP 2007, Paper 7530, Nice, France, May 13-18, 2007.

C58. Hawkes, G. L., Hawkes, B. D., Sohal, M. S., Armstrong, T. R., Torgerson, P. T., and Williams, M. C., "Development of Reversible SOFC's for Hydrogen Production," Electrochemical Society Meeting, Abstract # 333, Chicago, Illinois, May 6-10, 2007. (presentation only)

C59. Harvego, E. A., McKellar, M. G., O'Brien, J. E., Herring, J. S., "Sensitivity Studies of Advanced Reactors Coupled to High Temperature Electrolysis (HTE) Hydrogen Production Processes," 15th International Conference on Nuclear Energy, paper no. ICONE15-10740, April 22-26, 2007, Nagoya, Japan.

C60. Hawkes, G. L., O'Brien, J. E., Stoots, C. M., Jones, R., "Three Dimensional CFD Model of a Planar Solid Oxide Electrolysis Cell for Co-Electrolysis of Steam and Carbon-Dioxide," 2006 Fuel Cell Seminar, paper no. 298, Nov. 13 – 17, 2006, Honolulu.

C61. Stoots, C. M., O'Brien, J. E., Hawkes, G. L., Herring, J. S., and Hartvigsen, J. J., "High Temperature Co-Electrolysis of H2O and CO2 for Syngas Production," 2006 Fuel Cell Seminar, paper no. 418, Nov. 13 – 17, 2006, Honolulu.

C62. O'Brien, J. E., Stoots, C. M., Herring, J. S., Hawkes, G. L., and Hartvigsen, J. J., "Thermal and Electrochemical Performance of a High-Temperature Steam Electrolysis Stack," 2006 Fuel Cell Seminar, paper no. 417, Nov. 13 – 17, 2006, Honolulu.

C63. O'Brien, J. E., Stoots, C. M., Herring, J. S., Hawkes, G. L., "Hydrogen Production from Nuclear Energy via High-Temperature Electrolysis," invited paper, Energy Center Hydrogen Initiative (ECHI) Symposium, Purdue University, April 5-6, 2006.

C64. McKellar, M. G., Harvego, E. A., Richards, M., and Shenoy, A., "A Process Model for the Production of Hydrogen using High Temperature Electrolysis," paper no. 89694, 14th International Conference on Nuclear Energy (ICONE), Miami, July 17 – 20, 2006.

C65. O'Brien, J. E., Stoots, C. M., and Hawkes, G. L., "Comparison of a One-Dimensional Model of a High-Temperature Solid-Oxide Electrolysis Stack with CFD and Experimental Results," Proceedings, 2005 ASME International Mechanical Engineering Congress and Exposition, Nov. 5 – 11, Orlando.

C66. Schultz, K., Henderson, D., Pickard, P., O'Brien, J., Lewis, M., Summers, W. "Fueling the Hydrogen Economy: Status of the US Program for Hydrogen Production using Nuclear Energy," MIT – Tokyo Institute of Technology Symposium on Advance Nuclear Power Systems, Nov. 4, 2005.

C67. Stoots, C. M., O'Brien, J. E., McKellar, M. G., Hawkes, G. L., and Herring, J. S., "Engineering Process Model for High-Temperature Steam Electrolysis System Performance Evaluation," AIChE 2005 Annual Meeting, Cincinnati, Oct. 30 – Nov. 4, 2005.

C68. Herring, J. S., O'Brien, J. E., Stoots, C. M., and Hawkes, G. L., "High Temperature Electrolysis for Hydrogen Production Using Nuclear Energy" Paper #501, GLOBAL 2005, Paper #501, Tsukuba, Japan, Oct. 9 – 13, 2005.

C69. Hawkes, G. L., O'Brien, J. E., Stoots, C. M., Herring, J. S., Shahnam, M., "CFD Model of a Planar Solid Oxide Electrolysis Cell for Hydrogen Production from Nuclear Energy," presented at the 11th International Topical Meeting on Nuclear Reactor Thermal-Hydraulics NURETH-11, Popes Palace Conference Center, Avignon, France, October 2-6, 2005.

C70. O'Brien, J. E., Stoots, C. M., and Herring, J. S., "High-Temperature Electrolysis for Hydrogen Production From Nuclear Energy," presented at the 11th International Topical Meeting on Nuclear Reactor Thermal-Hydraulics NURETH-11, Popes Palace Conference Center, Avignon, France, October 2-6, 2005.

C71. Hawkes, G. L., O'Brien, J. E., Stoots, C. M., Herring, J. S., Shahnam, M., "Thermal and Electrochemical Three Dimensional CFD Model of a Planar Solid Oxide Electrolysis Cell," Proceedings, 2005 ASME Heat Transfer Conference, July 17-22, 2005, San Francisco.

C72. O'Brien, J. E., Stoots, C. M., Herring, J. S., and Hartvigsen, J. J.,"Hydrogen Production Performance of a 10-Cell Planar Solid-Oxide Electrolysis Stack," Proceedings, ASME 3rd International Conference on Fuel Cell Science, Engineering, and Technology, May 23 – 25, 2005, Ypsilanti, MI.

C73. Herring, J. S., O'Brien, J. E., Stoots, C. M., and Hawkes, G. L., "Progress in High-Temperature Electrolysis for Hydrogen Production using Planar SOFC Technology," 2005 AIChE Spring Annual Meeting, April 10 – 14, 2005, Atlanta, GA.

C74. Herring, J. S., Anderson, R., Lessing, P. A., O'Brien, J. E., Stoots, C. M., Hartvigsen, J. J., and Elangovan, S., **"**Hydrogen Production through High-Temperature Electrolysis in a Solid Oxide Cell," presented at the National Hydrogen Association 15th Annual Conference, Los Angeles, April 26-29, 2004.

C75. O'Brien, J. E., Stoots, C. M., Herring, J. S., and Lessing, P. A., "Performance Characterization of Solid-Oxide Electrolysis Cells for Hydrogen Production," Proceedings, 2nd International Conference on Fuel Cell Science, Engineering, and Technology, June 14-16, 2004, Rochester, NY, paper# 2474, pp., 219 – 228.

C76. S. Elangovan, J. Hartvigsen, J. E. O'Brien, C. M. Stoots, J. S. Herring, P. A. Lessing, "Operation and Analysis of SOFCs in Steam Electrolysis Mode," Proceedings, 6th European Solid Oxide

Fuel Cell Forum, 28 June – 2 July 2004, Kultur- und Kongresszentrum Luzern, Lucerne, Switzerland.

C77. Herring, J. S., O'Brien, J. E., Stoots, C. M., Lessing, P. A., Anderson, R. P., Hartvigsen, J. J., and Elangovan, S., "Hydrogen Production from Nuclear Energy via High-Temperature Electrolysis," Proceedings, 2004 International Conference on Advances in Nuclear Power Plants (ICAPP '04), June 13-17, 2004, Pittsburgh, PA, paper no. 4322.

C78. Herring, J. S., O'Brien, J. E., Stoots, C. M., Lessing, P. A., Anderson, R. P., Hartvigsen, J. J., and Elangovan, S., "Hydrogen Production through High-Temperature Electrolysis Using Nuclear Power," presented at the AIChE Spring National Meeting, New Orleans, April 25 – 29, 2004.

C79. O'Brien, J. E., Stoots, C. M., Herring, J. S., Lessing, P. A., Hartvigsen, J. J., and Elangovan, S., "Performance Measurements of Solid-Oxide Electrolysis Cells for Hydrogen Production from Nuclear Energy," Proceedings, 12th ICONE Meeting, April 25-29, 2004, Arlington, VA, paper # ICONE12-49479.

C80. Herring, J. S., Lessing, P. A., O'Brien, J. E., and Stoots, C. M., Hartvigsen, J., and Elangovan, S., "Hydrogen Production through High-Temperature Electrolysis in a Solid Oxide Cell," Second Information Exchange Meeting on Nuclear Production of Hydrogen, Argonne National Laboratory, Oct. 2-3, 2003.

DOE Milestone Reports

R1. O'Brien, J. E., Soots. C. M., Herring, J. S., Housley, G. K., Sohal, M. S., Milobar, D. G., Hartvigsen, J. J., Tao, G., Petigny, N., and Cable. T. L., "Insights Gained from Testing Alternative Cell Designs," INL/EXT-09-16783, September 15, 2009.

R2. Stoots, C. M., O'Brien, J. E., Herring, J. S., Housley, G. K., Milobar, D. G. and Sohal, M. S. (INL); Hartvigsen, J. J., Larsen, D., and Elangovan, S. (Ceramatec, Inc.), Cable, T. (NASA-Glenn), "Long-Term Degradation Testing of High-Temperature Electrolytic Cells," INL/EXT-09-16559, August 15, 2009.

R3. Sohal, S., O'Brien, J. E., Stoots, C. M., Herring, J. S., Hartvigsen, J. J., Larsen, D., Elangovan, S., Cater, J. D., Sharma, V. I., and Yildiz, B., "Critical Causes of Degradation in Integrated Laboratory Scale Cells during High Temperature Electrolysis," INL/EXT-09-16004, May 29, 2009.

R4. Stoots, C. M., Condie, K. G., Moore-McAteer, L., O'Brien, J. E., Housley, G. K., and Herring, J. S., "Integrated Laboratory Scale Test Report," INL/EXT-09-15283, February 27, 2009.

R5. Hawkes, G. L., and O'Brien, J. E., "Alternate Geometry CFD Predictions," INL/EXT-08-14587, August 1, 2008.

R6. Sohal, M. S., and Herring, J. S., "Oxygen Handling and Cooling Options in High Temperature Electrolysis Plants," INL/EXT-08-14483, July 2, 2008.

R7. Herring, J. S., Stoots, C. M., Condie, K. G., and O'Brien, J. E., "Test Plan for Three-Module Operation of the High Temperature Electrolysis Integrated Laboratory Scale Experiment," INL/EXT-08-14303, May 15, 2008.

R8. Condie, K. G., Stoots, C. M., O'Brien, J. E., and Herring, J. S., Characterization of the Transient Response of the ILS with One Module Installed to Heatup Changes in Power Level and Cooldown," INL/EXT-07-13626, December 14, 2007.

R9. McKellar, M. G., O'Brien, J. E., Harvego, E. A., and Herring, J. S., "Optimized flow sheet for a reference commercial-scale nuclear-driven high-temperature electrolysis hydrogen production plant," November 14, 2007.

R10. O'Brien, J. E., Stoots, C. M., Hartvigsen, J. J. and Herring, J. S., "Documentation of Short Stack and Button Cell Experiments Performed at INL and Ceramatec during FY07," September 14, 2007.

R11. McKellar, M. G., O'Brien, J. E., and Herring, J. S. "Commercial Scale Performance Predictions for High-Temperature Electrolysis Plants Coupled to Three Advanced Reactor Types," September 14, 2007.

R12. Cadwallader, L., "Monitoring for Combustible and Toxic Gases," November 28, 2006.

R13. Harvego, E. A., McKellar, M. G., O'Brien, J. E., and Herring, J. S., "Summary of Reactor-Coupled HTE Modeling Sensitivity Studies," October 26, 2006.

R14. O'Brien, J. E., McKellar, M. G., Stoots, C. M., Hawkes, G. L., and Herring, J. S., "Analysis of Commercial-Scale Implementation of HTE to Oil Sands Recovery," September 15, 2006.

R15. Stoots, C. M., Condie, K. G., O'Brien, J. E., Housley, G. K., and Herring, J. S., "Integral Laboratory Scale Stack Specification Mechanical Design Report," August 15, 2006.

R16. O'Brien, J. E., Stoots, C. M., and Herring, J. S., "Documentation of INL High-Temperature Electrolysis Milestone: Operation of HTE Stack at 100 NL/hr Hydrogen Production Rate for 1000 Hours," April 15, 2006.

R17. O'Brien, J. E., Stoots, C. M., McKellar, M. G., Housley, G. L. , Condie, K. G., and Herring, J. S. , "High Temperature Electrolysis Integrated Laboratory Scale Performance, Space and Power Requirements," DOE NHI Milestone Report, February 1, 2006.

R18. Stoots, C. M., O'Brien, J. E., and Herring, J. S., "Conceptual Design Documentation for High-Temperature Electrolysis Pilot-Scale Experiment at 200 kW," August 15, 2005.

R19. O'Brien, J. E., McKellar, M. G., Stoots, C. M., Hawkes, G. L., and Herring, J. S., "Analysis of Commercial-Scale Implementation of HTE to Oil Sands Recovery," August 15, 2005.

R20. O'Brien, J. E., Stoots, C. M., and Herring, J. S., "Documentation of INL High-Temperature Electrolysis Milestone Demonstrating 100 NL/hr Hydrogen Production Rate," August 1, 2005.

R21. Stoots, C. M., O'Brien, J. E., McKellar, M. G., Hawkes, G. L., and Herring, J. S., "Engineering Process Model for High-Temperature Electrolysis System Performance Evaluation," May 17, 2005.

R22. O'Brien, J. E., Hawkes, G. L., and Stoots, C. M., "Progress report on analysis of engineering and commercial scale HTE units," January 15, 2005.

R23. O'Brien, J. E., Stoots, C. M., and Herring, J. S., "Documentation of INEEL High-Temperature Electrolysis Milestone Demonstrating 50 NL/hr Hydrogen Production Rate," October, 2004.

R24. O'Brien, J. E., Stoots, C. M., and Herring, J. S., "Design of a 50 kW Integrated Laboratory-Scale High-Temperature Electrolysis Facility," September 15, 2004.

R25. O'Brien, J. E., Stoots, C. M., and Herring, J. S., "High Temperature Electrolysis Scaling Demonstration Experiments," July 30, 2004.

R26. Stoots, C. M., O'Brien, J. E., and Herring, J. S., "High Temperature Electrolysis System Configuration Study," June 30, 2004.

Internal Project Milestone Reports

IMR1. Sohal, S., "Degradation in Solid Oxide Cells during High Temperature Electrolysis," INL/EXT-09-15617, May 21, 2009.

IMR2. O'Brien, J. E., Stoots, C. M., Herring, J. S., McKellar, M. G., Hawkes, G.L., Harvego, E. A., Sohal, M. S., and Condie, K. G., "High Temperature Electrolysis for Hydrogen Production from Nuclear Energy – Technology Summary, INL/EXT-09-16140, May 18, 2009.

IMR3. Harvego, E. A., "Implementation of Lead-Bismuth Properties into Unisim," May 2006.

IMR4. Harvego, E. A., "Implementation of Molten Salt Properties into Unisim," May 2006.

Invited Presentations

P1. Hawkes, G. L., "Bio-Syntrolysis – Developing Highly Carbon-Efficient BTL Process Combining High Temperature Steam Electrolysis and Biomass Gasification," 4th BTLtec Conference, Graz, Austria, September 24 – 25, 2009.

P2. Hawkes, G. L., McKellar, M. G., Wood, R. and Plum, M.,"Biomass to Liquid Fuel via High Temperature Steam Electrolysis," International Biomass Conference, Portland, OR, April 28 – 30, 2009.

Patents and IDRs

1. IDR# 1461, O'Brien, J. E., Housley, G. K., Hawkes, G. L., and Stoots, C. M., "Internally manifolded compact heat exchanger for heat recuperation from a multiple-stack high-temperature electrolysis module," submitted, April 1, 2008.
2. Patent Application (in progress): Hawkes, G. L., Herring, J. S., Stoots, C. M., O'Brien, J. E., McKellar M. G., and Wood, R. A. "Methods and Systems for Producing Syngas," IDR #BA-254, pending US Patent 12/054,269, filed March 24, 2008. IDR:
3. IDR #BA-244, Lessing, P. A., Demkowicz, P. A., DeWall, K. G., and Medvedev, P. G., "Protective Coating for Bi-polar Plate," submitted 1/31/07.
4. Patent Application (in progress): Stoots, C. M., O'Brien, J. E., Herring, J. S., Lessing, P. A., Hawkes, G. L., and Hartvigsen, J. J., "High temperature H2O/CO2 Co-Electrolysis for Syngas Production," IDR# BA-069, pending US Patent 11/461,337, filed July 31, 2006.
5. IDR #BA-203, "High Temperature $H_20/C0_2$ Co-Electrolysis for Syngas Production with Renewable Energy Power Sources," (this IDR will likely be considered as a CIP to the pending US Patent 11/461,337 filed 7/31/2006).
6. Patent Application (in progress): Hawkes, G. L., Herring, J. S., Stoots, C. M., and O'Brien, J. E., "Electrolytic/Fuel Cell Bundles and Systems Including a Current Collector in Communication with an Electrode Thereof, Methods for Generating Electricity and/or Performing Electrolysis Using the Same," BA-133, elected for Patent Application, March 2006.